Imperial College London

# CREEP AGE FORMING INVESTIGATION ON ALUMINIUM ALLOY 2219 AND RELATED STUDIES

by

**Haoliang Yang**

A Thesis submitted for the Degree of Doctor of Philosophy of Imperial College London and the Diploma of Imperial College London

Department of Mechanical Engineering

Imperial College London

June 2013

# Abstract

By the middle of the 20th Century, traditional mechanical metal forming methods were showing to be inadequate for producing components comprising of large high strength aluminium alloy panels with complex curvatures, such as those used in modern aircraft and aerospace metal structures. To deal with this problem, a new forming method was conceived by Textron, which has proven to be very useful for forming components with these shape characteristics and good mechanical properties. The method is called Creep Age Forming (CAF).

The research described in this thesis is a study of CAF of a 2219 aluminium alloy, which is used for fabricating the isogrid structure for fuel tanks of launch vehicles. The main aim of the research is to develop experimental and modelling tools for CAF of AA2219 sheet structures.

A series of creep-ageing tests and stress-relaxation tests have been conducted on AA2219 at 175 ℃ . The age-hardening, creep deformation and stress relaxation behaviour of AA2219 have been investigated. Based on the experimental investigation, a novel set of physically based, unified creep constitutive equations has been established.

A small scale CAF test rig was designed to validate the springback prediction from FE simulation. The experimental result and simulation are in good agreement. Development of FE procedures for simulating creep-ageing behaviour of the material and springback has been performed to predict and assess the springback behaviour of metal sheet in typical forming tools.

Integrated numerical procedures for predicting stress relaxation and springback and tool shape determination for autoclave creep age forming isogrid panel have been developed. Meanwhile, experimental work has been carried out to investigate mechanical-based creep age forming of stiffened structures.

# Declaration of Originality

I hereby declare that this thesis ‘ CREEP AGE FORMING INVESTIGATION ON ALUMINIUM ALLOY 2219 AND RELATED STUDIES’ and the work reported herein was composed by and originated entirely from me. Information derived from the published and unpublished work of others has been acknowledged in the text and references are given in the list of sources.

07/2013

Haoliang Yang

# Copyright Declaration



07/2013

Haoliang Yang

# Acknowledgements

I would like to thank Professor Dear for his scientific support. His guidance and support were tremendous for me. Without your help, I would not be able to finish my research work. Thanks to Professor Dear for giving me a valuable chance to study and research at Imperial College London. Thank you for your efforts in providing such a good working environment. You did not only teach me lessons in science and research, but also in many different aspects in personal and professional life.

The most important person who deserves more thanks than I could ever do in words is Dr. Catrin Davies, my lovely and daily supervisor. During my PhD study, I received tremendous encouragement and academic guidance from Dr. Davies. Without your help, I would not be able to conquer the difficulties and finish the work. Without your help, I could not to be able to be more confident in the research work. Dr. Davies, thank you very much and I wish you all the best in your future life and career.

I would like to express my appreciation to Professor Lin and Professor Dean. Thank you so much for providing me such a good chance to work with you and learn from you. Your rich experiences have provided me strong support in the modelling and experimental work. Moreover, you have taught me valuable lessons in science and engineering and you have setup very good examples for my future personal and professional life.

I would like to express my sincere appreciation to my project partner Dr. Li Wan. We worked on the project together for over one year and this is a valuable experience for me. With your help, my research progressed very smoothly. During this period, I learned from

you on many different aspects, such us how to conduct research, how to solve practical problems.

I would like to appreciate my girlfriend, Zhou Long. I spent most of my time on my work and could not find enough time to stay with you, which makes me feel sorry, but you have shown great understandings and you are always supportive. When I was over-stressed, you can always find methods to help me to release. When I felt frustrated in my PhD work, you kindly encouraged and supported me so that I can pass the difficult time quickly. I learned computer programming and photography skills from you which are extremely helpful in my PhD work.

During my PhD study, many friends and colleagues have helped me a lot and I would like to take this opportunity to express my sincere appreciation. Dr. Paul Hooper, Dr. Hari Arora, Mr. Aditya Narayanan, Dr. Qian Bai, Dr. Liliang Wang, you have helped me when I met difficulties in FE simulations and experiments.

Thanks to technical support staff of the department. Dr. Leonard Wanigasooriya, Mr. Suresh Viswanathan Chettiar, Dr. Ruth Brooker, and Mr. Amit Choda, your efficient and effective helps have provided strong supports to my experiments.

At last but not least, I would also like to express my sincerest appreciation to my parents. You always support me and help me. Thank you!

# List of Nomenclature

| | |
|---|---|
| $x, y, z$ | coordinate axis |
| $t$ | thickness of the workpiece |
| $U1, U2, U3$ | displacement constraint in $x, y, z$ direction respectively in ABAQUS |
| $UR1, UR2, UR3$ | rotation constraint about $x, y, z$ axis respectively in ABAQUS |
| $T$ | ageing time |
| $T_A$ | effective ageing time |
| $E$ | Young's modulus |
| $\varepsilon$ | strain |
| $\varepsilon_T$ | total strain |
| $\varepsilon_e$ | elastic strain |
| $\varepsilon_c, \dot{\varepsilon}_c$ | creep strain and rate |
| $\varepsilon_{in}$ | inelastic strain |
| $\bar{\varepsilon}$ | equivalent plastic strain |
| $\dot{\bar{\varepsilon}}$ | equivalent plastic strain rate |
| $\dot{\bar{\varepsilon}}_c$ | equivalent creep strain rate |
| $\sigma$ | stress |
| $\sigma_1, \sigma_2, \sigma_3$ | stress at time, $t_1, t_2, t_3$ respectively |
| $\sigma_c$ | critical load/stress |

| | |
|---|---|
| $\sigma_y$ | yield stress (MPa) |
| $\sigma_{ij}$ | Cauchy stress |
| $\hat{\sigma}_{ij}$ | Jaumann rate of Cauchy stress |
| $\sigma_e$, $\sigma^e$ | equivalent stress |
| $\sigma^e_{\max}$ | maximum equivalent stress |
| $\psi$ | energy dissipation rate potential |
| $\sigma_A, \dot{\sigma}_A$ | ageing (precipitation) hardening and rate ($h^{-1}$) |
| $\sigma_{SS}, \dot{\sigma}_{SS}$ | solute hardening rate ($h^{-1}$) |
| $\sigma_{dis}, \dot{\sigma}_{dis}$ | dislocation hardening rate ($h^{-1}$) |
| $r$ | the radius of the disc plane in disc shaped precipitates |
| $l$ | the half-length of the peripheral plane in disc shaped precipitates |
| $A$ | the ratio of half length to radius for the disc-shape precipitates |
| $N_p, \dot{N}_p$ | precipitates density and rate |
| $R_g$ | gas constant |
| $V_0$ | the average volume of the precipitates |
| $V_m$ | molar volume of precipitates |
| $\Delta G$ | critical activation energy for precipitation |
| $\beta$ | the parameter for precipitates growth |
| $k_b$ | Boltzmann constant |
| $Z$ | Zeldovich's factor |

| | |
|---|---|
| $L$ | Avogadro number |
| $p_A$ | the parameter related to $\beta$ |
| $\beta^*$ | the parameter related to the volume fraction ( $f_v$ ) of disc-shape precipitates |
| $r^*$ | the critical radius of the precipitates |
| $a_l$ | the lattice parameter related to $\beta^*$ |
| $D$ | the diffusion coefficient of solute atom in solvent |
| $\Omega$ | the super-saturation parameter related to $\beta$ |
| $\gamma$ | the precipitates-matrix interfacial energy |
| $F_V$ | the driving force per mole of solute atom to precipitate from super saturated solid solution |
| $\upsilon_{at}$ | the molar volume of precipitate |
| $C_0, C_e, C_p$ | the mean solute concentrations by atom percentage in matrix, equilibrium precipitate-matrix interface and precipitates, respectively |
| $f_v^*$ | the maximum volume fraction of precipitates |
| $\overline{f}_v, \dot{\overline{f}}_v$ | normalized volume fraction of precipitates and rate |
| $l_n, \dot{l}_n$ | the growth of the characteristic size of precipitate and rate |
| $E_1, w_1, w_2, v_1$ | material constants related to the normalized volume fraction of precipitates |
| $Q_1, E_2, v_2$ | material constants related to the growth of the characteristic size of precipitate |

| | |
|---|---|
| $Q_2$ | the activation energy related to the growth of precipitates |
| $\overline{A}$ , $\dot{\overline{A}}$ | the mean ratio of half length to radius for the disc-shape precipitates and rate |
| $A_C$ | the mean ratio at peak ageing state |
| $\overline{\rho}$ , $\dot{\overline{\rho}}$ | normalized dislocation density and rate |
| $\rho_i$ | dislocation density for the virgin material |
| $\rho_m$ | maximum (saturated) dislocation density |
| $\rho$ | dislocation density |
| $S_{ij}$ | deviatoric stress tensor |
| $D_{ij}^p$ | rate of inelastic deformation |
| $D_{ij}^{\mathrm{e}}$ | rate of elastic deformation |
| $D_{ij}^{\mathrm{T}}$ | rate of total deformation |
| $GP$ | Gruinier-Prestion zones |
| $\theta$", $\theta$' | transitional phases of the inter-metallic $\theta$ |
| $\theta$ | $CuAl_2$ precipitates |
| α | single phase solution of Al and Cu |
| $G$ , $\lambda$ | Lamé elasticity constants |
| $\partial\Delta p / \partial p$ | gradients of inelastic strain in ABAQUS |
| $\partial\Delta p / \partial\sigma_e$ | gradients of effective stress in ABAQUS |
| $SP$ | springback index in four point bend test |
| $\delta_A$ | distance between the bottom surface of undeformed |

| | |
|---|---|
| | workpiece and bottom frame surface |
| $\delta_B$ | distance between the bottom surface of fully loaded workpiece and bottom frame surface |
| $\delta_C$ | distance between the bottom surface of workpiece after springback and bottom frame surface |
| $SP_n$ | numerical springback index |
| $S$ | engineering springback factor |
| $\delta_f$ | the final maximum vertical distance on the workpiece after springback |
| $\delta_0$ | the maximum vertical distance on the workpiece when fully loaded |
| $R_i$ | local radius of curvature of a workpiece |
| $(O_{iX}, O_{iY})$ | coordinates for the centre of curvature |
| $(X_{i-10}, Y_{i-10}), (X_i, Y_i), (X_{i+10}, Y_{i+10})$ | the coordinates of the three selected nodes |
| $CI$ | localized curvature index |
| $R_i$ | instantaneous local radius of curvature |
| $R_{tool}$ | die's radius |
| $SI$ | localized springback index |
| $R_e$ | effective radius of target isogrid panel |
| $R_{es}$ | effective radius of springback isogrid panel |
| $\delta$ | ratio of effective radius between the springback and target isogrid panel |

| | |
|---|---|
| $A_1$, $B_1$, $k_0$, | material constants related to creep strain |
| $C_A$, $m_1$, | material constants related to ageing hardening |
| $C_{SS}$, $m_2$ | material constants related to solute hardening |
| $A_2$, $n$, | material constants related to dislocation hardening |
| $C_r$, $Q$, $m_3$, $\gamma_0$ , $m_4$, | material constants related to normalized mean ratio of disc-shape precipitates |
| $C_p$, $m_5$ | material constants related to dislocation density |
| $\bar{r}$ , $\dot{\bar{r}}$ | normalized precipitate size for sphere precipitate and rate |

# Contents

# List of Figures

# List of Tables

# Chapter 1

# Introduction

## 1.1 Launch Vehicles

In the aerospace industry, a launch vehicle is a rocket used to carry payload from the Earth's surface into outer space. Usually the payload is an artificial satellite placed into orbit [1-3]. There are two types of launch vehicles: one is expendable launch vehicles, which are designed for one-time use. They always separate from their launched payload at the objective orbit and break up during atmospheric re-entry. Another one is reusable launch vehicles, which are designed to be recovered intact and used again for subsequent launches [4-8]. Currently, many nations and space agency have developed their expendable launch vehicle families [9]. For example, the European Space Agency developed the Arianne Family [6], Untied Launch Alliance manufactures and launches the Delta and Atlas Family and China Aerospace Corporation develops their Chang Zheng (CZ) Family [8, 10-12].

Launch vehicles are often characterized by the amount of mass they can carry into orbit [4, 5]. For example, Arianne 5 (Figure 1.1 (a)), as a part of Arianne rocket family, is manufactured under the authority of the European Space Agency and was used to deliver payloads into geostationary transfer orbit. On 22$^{nd}$ April 2011，the Arianne 5 ECA flight VA-201 broke a commercial record, lifting Yahsat 1A and Intelast New Dawn with a total payload weight of 10,064 kg to transfer orbit. This record was later broken again during the launch of Arianne 5 ECA flight VA-208, lifting a total of 10,182 kg into the planned geosynchronous transfer orbit [13].

The Chang Zheng 2F, also known as the CZ-2F, is a Chinese manned orbital carrier rocket, designed to launch manned Shenzhou spacecraft [14, 15]. On 15th October 2003, the CZ-2F launched Shenzhou 5, China's first manned spaceflight. The CZ-2F has successfully launched the Shenzhou 6, 7, 9 missions into orbit between 2004 and 2010. On 16th June 2012, it was used to deliver Tiangong-1 (China's first space station) to demonstrate orbital rendezvous and docking capabilities (Figure 1.1 (b)).

(a) Arianne-5 (b) LM-2F

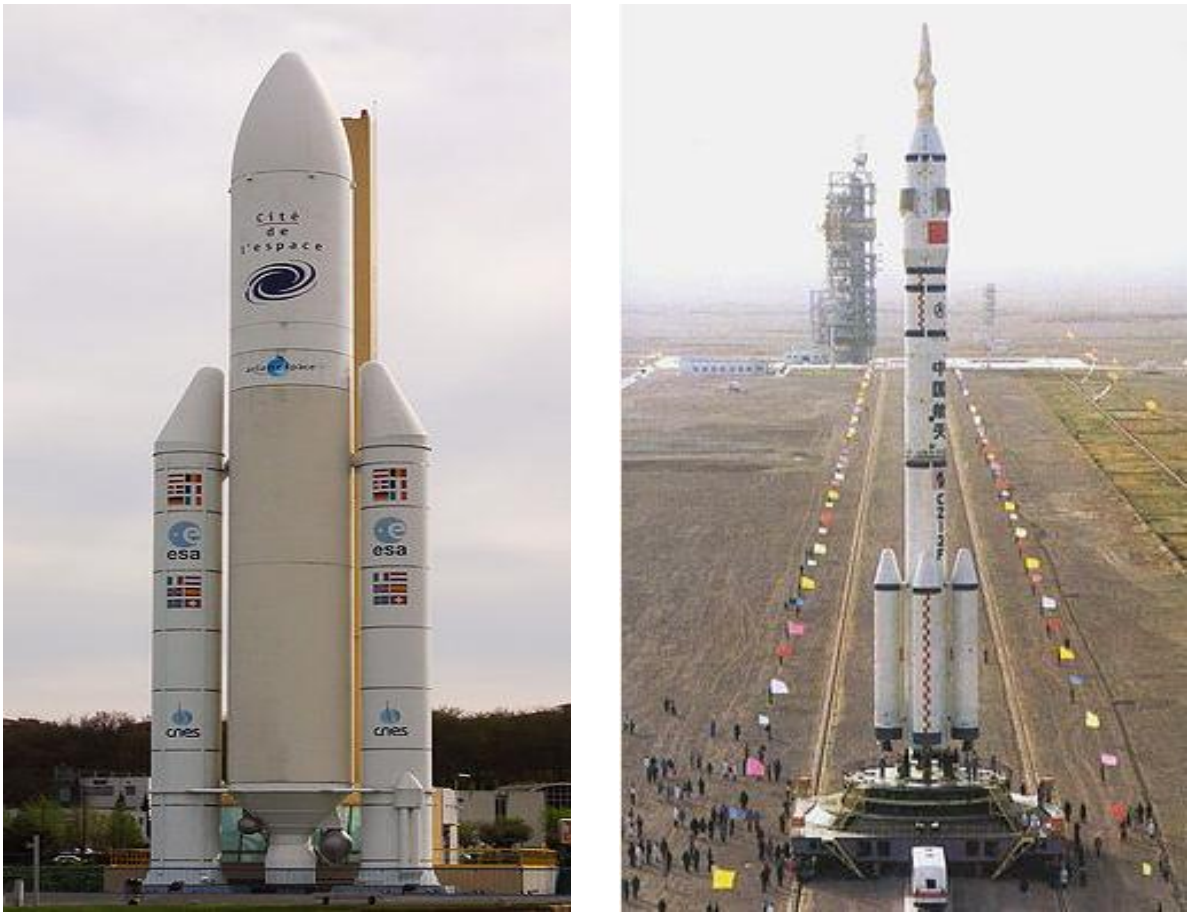


Figure 1.1: (a) Arianne 5 used to deliver payloads into geostationary transfer orbit or low earth orbit [13] and (b) LM-2F used to deliver Tiangong-1 to demonstrate orbital rendezvous and docking capabilities [16].

## 1.2 Isogrid Structures in Launch Vehicles

Weight saving is of great importance in designing and fabricating aerospace structures because of the high cost of each kilogram of payload [17, 18]. The launch vehicles' body are generally fabricated by lightweight structures. Isogrid structures meet the needs of lightweight with high strength to weight ratios in launch vehicle structures. Aircraft fuselage, interstates, shrouds, orbital workshop interiors and launch vehicle fuel tanks are the main applications of these structures in airspace and aerospace industry [9, 19, 20]. These structures are characterized by a shell structure supported by a lattice pattern of stiffeners on either the inner or outer sides of the shell. It employs an array of equilateral triangle cut-outs to increase the stiffness per weight of a structure [21]. The concept of implementation of isogrid structures began in the early 1960s using aluminium structures and development continues today with focusing on optimizing stiffening patterns to further decreasing the weights [22]. The material used for manufacturing isogrid structures of fuel tanks is aluminium alloy 2219, which has a unique combination of properties such as its good ability to weld, high strength to weight ratio and superior cryogenic properties [23-25].

The isogrid structure has been successfully employed for the manufacture of fuel tanks of launch vehicle of CZ-LM Family developed by China Aerospace Corporation [11]. Figure 1.2 illustrates the assembly of the AA2219 isogrid structure for the fuel tanks of CZ-2F launch vehicles.

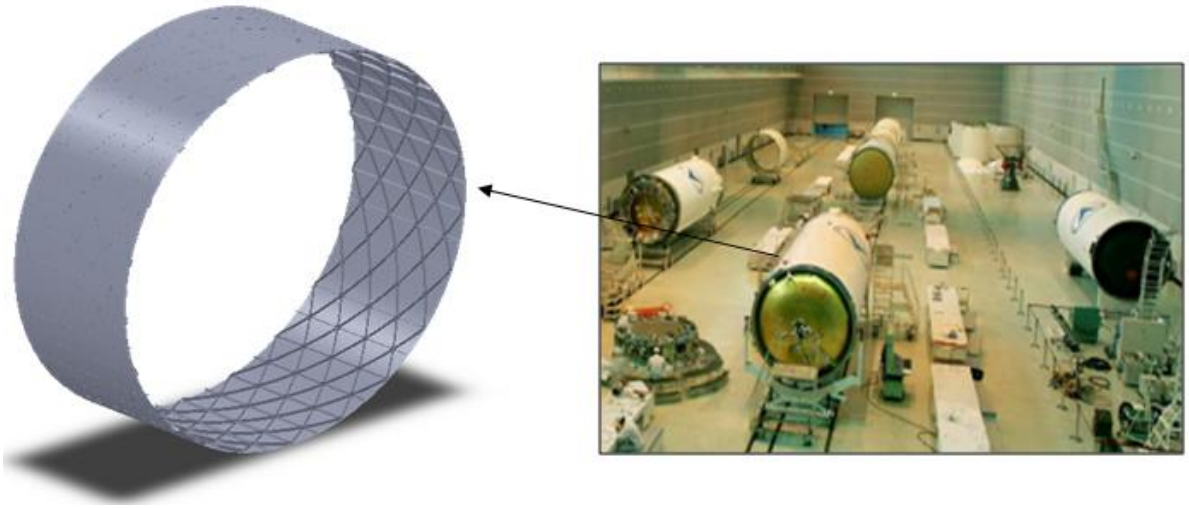

Figure 1.2: AA2219 isogrid stiffened structures for fuel tanks of launch vehicles.

## 1.3 Fabrication of Isogrid Structures

Figure 1.3 reviews the current manufacturing sequences involved in producing the cylindrical fuel tanks of launch vehicles [26, 27]. Firstly, the isogrid structures are typically fabricated by numerically controlled CNC machining operation on an AA2219-T87 flat panel (Figure 1.3(a)). Next, the machined isogrid panels are rolled after the machined-out pockets are filled with a low melting wax (Figure 1.3(b) and (c)). This filler material stabilizes the isogrid ribs, evenly distributing the forming/bending force throughout the whole structure during rolling. A rolling process without a filler material may result in an irregular skin and buckling of the ribs. After rolling process, the wax is melted out at 60 ℃ and the isogrid panel is cleaned in the water tank with the trimming of longitudinal edges thereafter (Figure 1.3(d), (e) and (f)). Finally, a cylindrical isogrid panel can be obtained by joining four pieces of individual formed isogrid panels via friction stir welding (FSW) (Figure 1.3(g). Excess materials at the lateral edges are machined off (Figure 1.3(h).

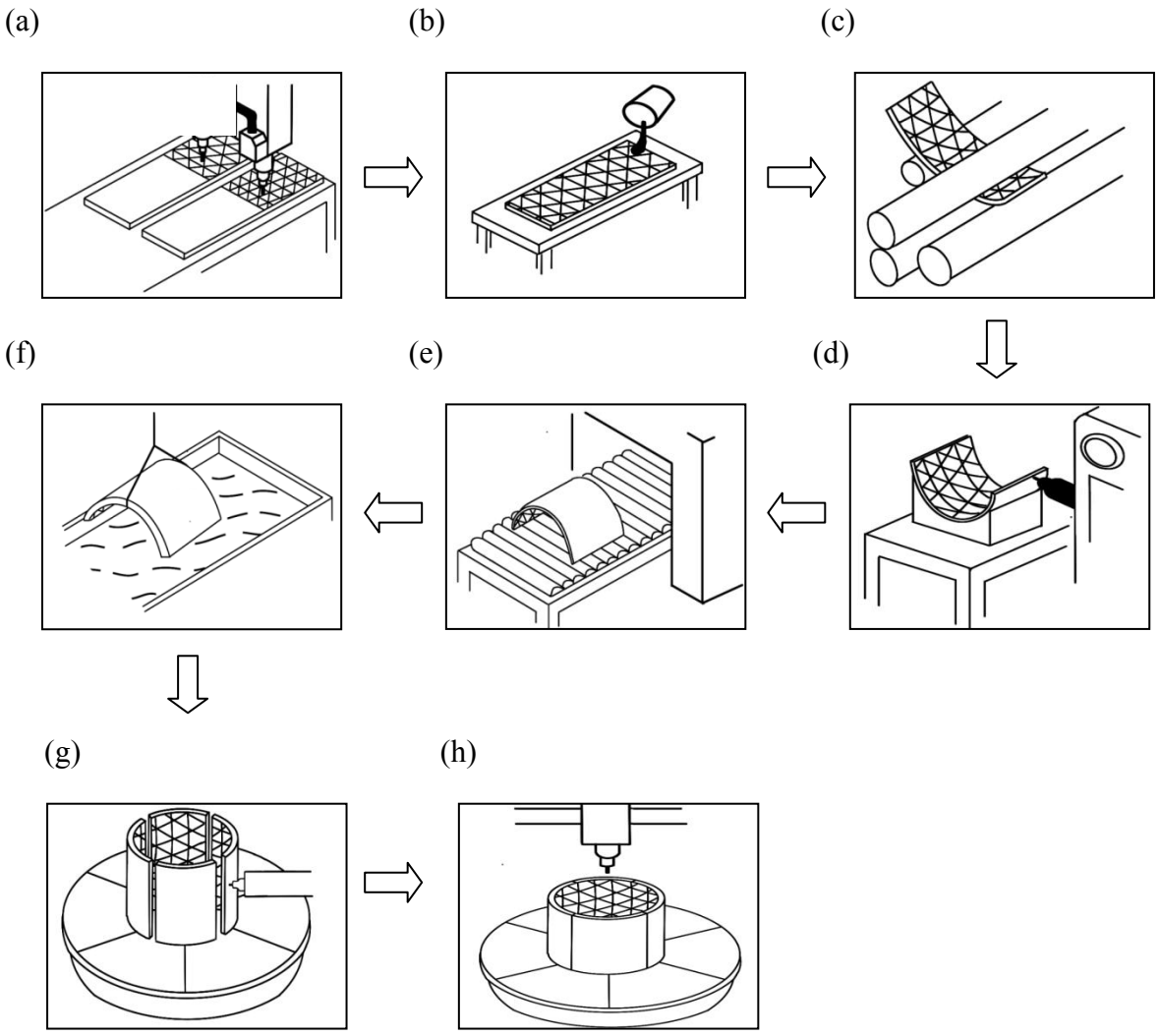


Figure 1.3: Roll forming sequence for isogrid stiffened structures.

## 1.4 Advanced Cylindrical Isogrid Structures

Many previous studies have shown that integral structures have a number of advantages in the application of structural components in the aerospace industry [28, 29]. Therefore, integral cylindrical isogrid structures are expected to be fabricated as integral as possible to reduce the number of parts, and thereby the manufacturing costs by reducing part assembly, handling, inventory and transport costs [30]. In the present research, a new concept is developed: The concept of this integral airframe structure (IAS) is illustrated in Figure 1.4.

IAS is the 'built-up' structures are fabricated by fewer components of the current 'built-up' structures. The objective of the IAS is to build structure that is less expensive and improve the structural performance than current 'built-up' structure. As shown in the figure, it is expected to reduce the number of isogrid panels for assembling the entire cylindrical isogrid structure. The strength values at the joint area are reduced by 30% at the HAZ areas and so that the thickness of the components have to be increased at the joint area to keep the structure safety [31-33]. Currently, a cylindrical fuel tank of launch vehicle is fabricated by four individual formed isogrid panels. It is then expected to use three parts or a single part to fabricate the entire cylindrical fuel tank structure to achieve the following advantages [29]:

- Weight savings. Lighter than the current built-up structure
- Cost savings. Cost less than the current built-up structure
- Improved structure integrity

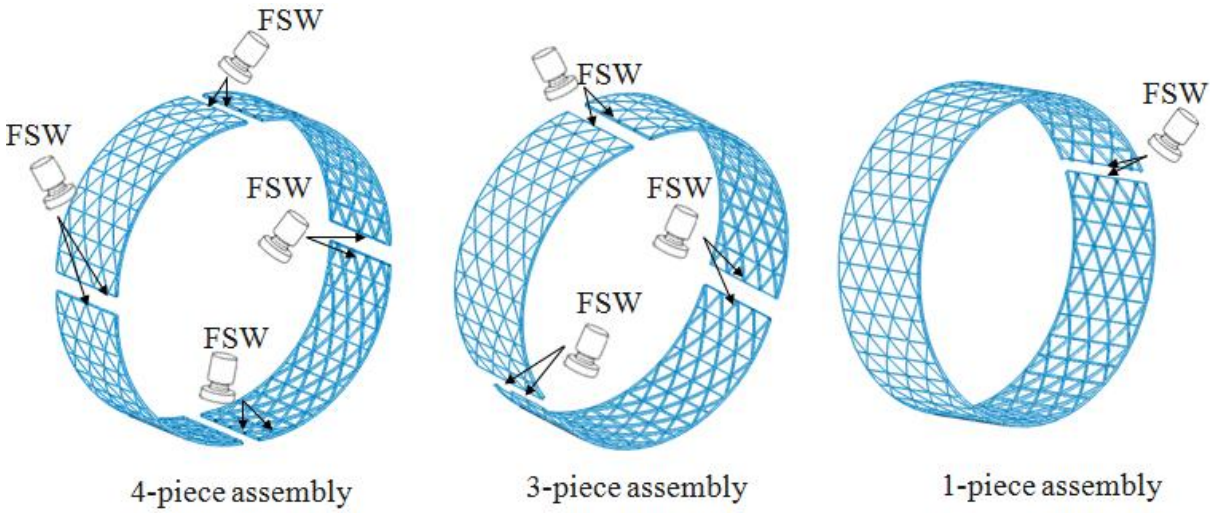


Figure 1.4: Concept of integral airframe structures for isogrid structures.

To meet this goal, the IAS program aims to develop a new and effective design approach for integral structures with reduced parts for assembling, along with manufacturing

technologies for implementing that approach. The design manufacturing technologies pursued would be selected from various possible concepts based on cost and performance criteria.

## 1.5 Advanced Forming Technologies

With the increasing demand for higher formability, durability and cost efficiency, there has been tremendous development in metal forming technologies and tool design in the past decades for forming large contoured sheet structures (isogrid panels can be also classified as sheet metal) [34-36]. One of the major concerns in forming these large contoured sheet structures is the amount of imparted residual stress left in the panel. If a high residual stress remaining in the panel's outer layer and the panel is subject to cyclic loading, as it would be in aerospace applications, the possibility of fatigue cracking is greatly increased [34, 37]. Conventional forming methods like roll forming, stretch forming and peen forming are based on plastic deformation and generate a high residual stress that causes problems when the material is loaded dynamically [36-42]. To deal with this problem, a new forming method was developed by Textron Aero-structures, which has been proven to be an advanced technology for forming components with complex curvature and achieve good mechanical properties [43]. This advanced forming technology is called creep age forming (CAF). Compared with the other forming techniques, CAF offers a potential solution that imparts significantly less residual stress. CAF utilizes the metallurgical stress relaxation behaviour during the artificial ageing of stressed aluminium alloy. It is notable that the CAF process can be performed on different types of heat-treatable aluminium alloys，such as 2XXX, 6XXX and 7XXX series [43-45]. Currently, most components made by CAF are aircraft wings and stringers [46], but this research aims to introduce the CAF technique into forming aerospace components.

## 1.6 Aim of the Work and Research Approach

The aim of this project is to develop experimental and numerical tools to predict creep-ageing behaviour and springback in creep age forming of AA2219 sheet structures. In order to achieve the aim, the research work was divided into the following distinct subjects:

First, the creep-ageing behaviour of AA2219 during CAF and its springback response are studied through experimental investigations and modelling work.

Second, based on an understanding of the creep-ageing behaviour of the material and establishment of the unified creep-ageing constitutive equations that are capable of modelling age-hardening, creep and prediction of stress relaxation during CAF, FE simulations have been performed to investigate the issues that could affect creep age forming process. Also, small scale CAF experimental work was carried out to validate the springback predictions.

Thirdly, FE simulations have been carried out on autoclave creep age forming isogrid structures to demonstrate the tool compensation process in CAF. In addition, experimental work has been performed on AA2219 stiffened structures with mechanical-based creep age forming method. Based on two cases, CAF processes have been proposed for forming isogrid cylindrical assembly for industrial applications.

## 1.7 Structure of Thesis

This thesis has been divided into nine chapters. This chapter provides a short introduction to the AA2219 isogrid structures for launch vehicles and the motivation of this research. Chapter 2 contains a review of recent research and scientific developments on the creep age forming process. Chapter 3 is dedicated to reporting the experimental

investigations. Creep ageing and stress relaxation ageing experiments have been designed to characterize the creep-ageing and stress relaxation behaviours of Aluminium Alloy 2219 under thermal exposure conditions. Based on experimental investigations, a unified constitutive equation for AA2219 has been adopted for the CAF process in Chapter 4. The determined equation set has been integrated into the commercial FE software ABAQUS via the user defined subroutine, CREEP, to describe the creep-ageing behaviour. In Chapter 5, a four point bend rig was designed and a series of creep age forming tests were carried out to investigate the springback of AA2219 sheet, In addition, simulations have been carried out to compare with the experimental observations. Numerical models have been established in Chapter 6 to analyse the difference in springback predictions between the two loading cases: end clamp and uniform pressure. The former is often used in small scale laboratory testing and the latter in real industrial forming processes. In Chapter 7, an iterative tool compensation method was introduced and demonstrated to compensate for forming AA2219 isogrid panels by autoclave forming process. Also, a proposed CAF process for forming 1/3 pieces isogrid cylindrical assembly by autoclave forming has been given. Besides autoclave forming method for CAF, a mechanical forming method for CAF has been proposed in Chapter 8, Corresponding experiments have been performed on creep age forming stiffened panels with an end clamp. Finally, the conclusions and suggestions for future work are presented in the last chapter, Chapter 9.

# CHAPTER 2

# Review of Creep Age Forming Technologies

## 2.1 Background and Current Development

Creep age forming (CAF) is the process by which a sheet (typically of aluminium) is formed into the required shape by creep deformation, whilst precipitation aging processes are performed simultaneously. The stresses generated in the workpiece, due to the restraining forces applied, gradually relax as creep strain accumulates [43].

Creep age forming is now widely applied in aircraft industry. For example, both the upper and lower wing skins of B-1B' Long Range Combat Aircraft or the USA are produced using CAF [37]. 'Bennetts Associates' has worked with Airbus on the development of CAF for producing the wing skin for the latest A380 airplane, using AA7055 alloy (Figure 2.1(a)). The length of the wing skin is 33 m, its widest section is 2.8 m, and it has a double curvature aerodynamic surface. Its thickness varies from 3 to 28 mm [47, 48]. STADCO, USA also developed one of the largest creep age-forming tools to manufacture Gulfstream G-5 upper and lower wing skin [43, 49], as shown in Figure 2.1(b).

Apart from aircraft wing panel manufacturing industry, creep age forming technique is also applied in other industries. For example, Rolls-Royce used CAF tool to produce wide chord fan blades and GKN AEROSPACE also employed the CAF technique to manufacture and fabricate aerospace engine inner fixed structure (Figure 2.1(c)) [50, 51].

(a) (b)

(c)

Figure 2.1: Creep age forming workpieces. (a) The world's largest commercial aircraft A380 wing panel [43], (b) Gulfstream G-5 wing skin [43], (c) GKN aerospace engine inner fixed structure [51].

## 2.2 Mechanisms of Creep Age Forming

### 2.2.1 Typical creep age forming process

Creep age-forming is typically divided into three stages. The typical process is shown schematically in Figure 2.2. Firstly, a fully machined flat workpiece is positioned onto a contoured forming tool. Next, a high temperature vacuum bag is fitted to seal the component against the continuous surface of the forming tool, the air is then removed from under the bag creating an atmospheric pressure differential, forcing the workpiece towards the tool surface.

Thereafter, the pressurised workpiece with the tool are loaded into an autoclave while the workpiece undergoes heat treatment at a heat-treatment temperature (120 $^{o}$C – 180 $^{o}$C) for a certain period of time. During the thermal exposure, stress relaxation due to creep occurs, inelastic strain is generated. At the end of the heat treatment cycle, the workpiece is removed from the autoclave and unwrapped. Some permanent deformation remains in the workpiece while there is some deformation recovery takes place, which is termed as springback [40, 43, 52]. Figure 2.3(a) shows a wrapped A380 wing panel prior to CAF while Figure 2.3(b) shows the wing panel taken out from autoclave after CAF.

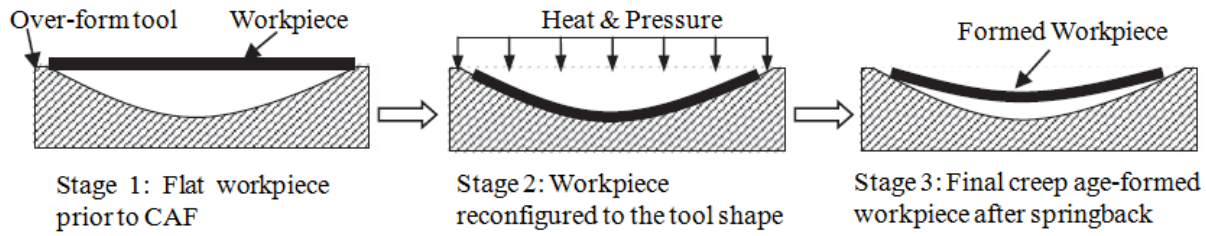


Figure 2.2: Creep age forming process [43].

(a) (b)

Figure 2.3: (a) Wrapped A380 wing panel, (b) panel taken out from autoclave after creep age forming [47].

### 2.2.2 Stress relaxation in creep age forming

The concept of CAF is based on stress relaxation phenomenon due to high temperature creep. During the CAF process, stresses present within the metal after initial loading/prior to ageing will seek to relieve themselves upon exposure to artificial ageing temperature. For a conventional forming operation, assuming that the initial stress within the workpiece is below the yield stress, when the workpiece is unloaded, it will physically relieve the stress by returning to its original shape. However, for CAF, the induced level stress is significantly relieved for a significant amount of time [52, 53], the workpiece, upon unloading, will not fully recover to its original state [45, 54-57]. A detailed stress-strain-time relationship during CAF process is shown in Figure 2.4. In Figure 2.4(a), stress redistribution between initial loading (material is below its yield stress) and after ageing for a simple single plane bending condition can be seen. Figure 2.4(b)-(d) present the corresponding stress-relaxation, creep curve and stress-strain relationship during CAF. The stress relaxation behaviour is mainly due to creep and thermal recovery. As shown in Figure 2.4(d), the stress level in the workpiece reduces from $\sigma_1$ to $\sigma_2$ . Even though the total strain, $\varepsilon_T$ , remains constant throughout the period of artificial ageing. The amount of the inelastic strain, $\varepsilon_{in}$ , is responsible for shaping the part.

(a)

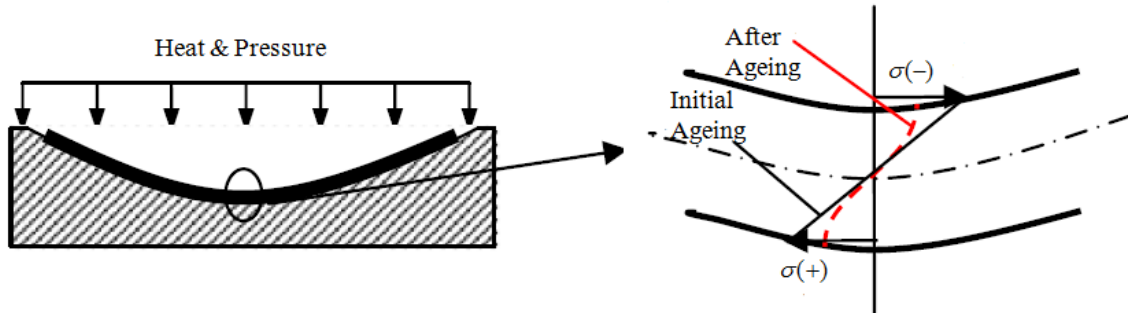


(b)

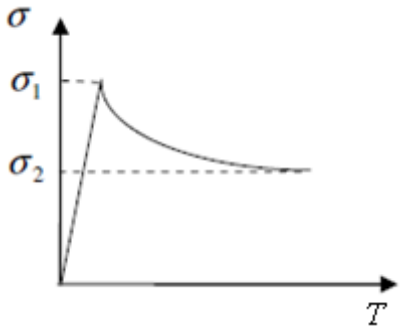


(c)

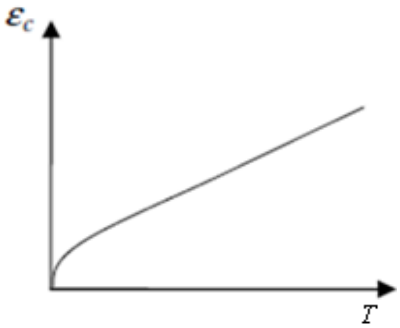


(d)

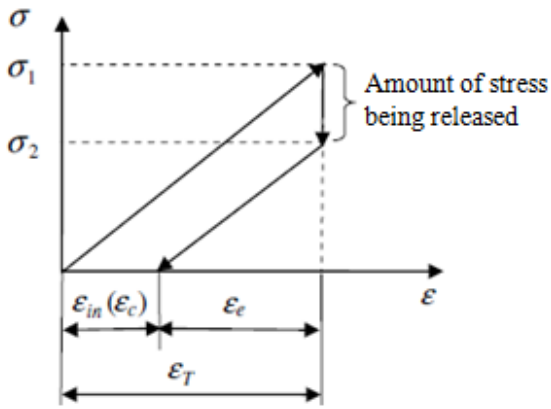


Figure 2.4: Forming mechanism of CAF under simple bending. (a) CAF under simple bending and stress distribution through thickness, (b) stress relaxation, (c) creep deformation, (d) stress relaxation that occurs during CAF [43].

### 2.2.3 Age hardening in creep age forming

CAF is not only a stress-induced deformation process, but also a process of artificial ageing the aluminium alloy. During the artificial ageing period in CAF, the constituents of the metal precipitates alter the microstructure of the material, which improves its mechanical strength [43, 45]. Due to the simultaneous increase of strength with relaxation of the metal during CAF, the creep deformation is different from that of conventional creep [58]. For conventional creep, the candidate material has been artificially aged to its highest strength already for creep resistance working at high temperature. However, in CAF, the material is relatively soft initially. Thus the primary creep rate is higher [57, 59]. Figure 2.5 shows the comparison of creep strain for conventional creep deformation (AA2219-T87) and creep in CAF (AA2219-T4) for a period of 18 hours. The creep rate in CAF is higher than that in the conventional creep deformation ( $\theta_{ca} > \theta_a$ ). It can also be seen that, more creep strain is accumulated in CAF process compared to conventional creep.

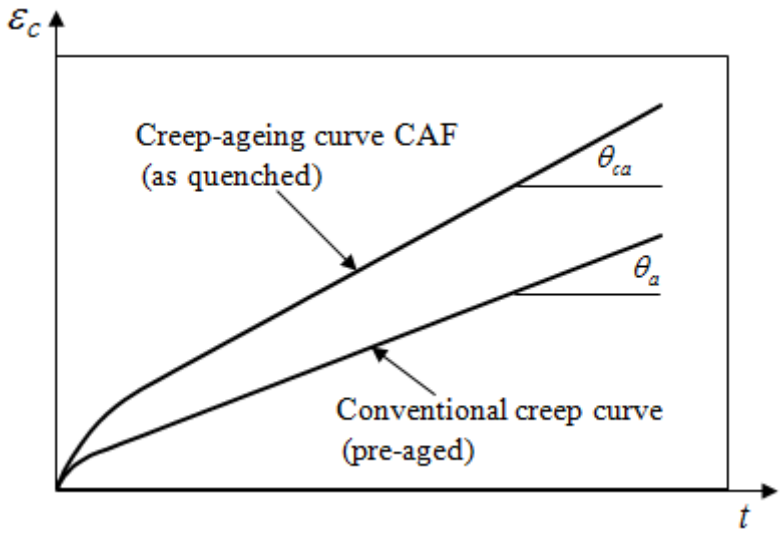


Figure 2.5: Comparison of primary stages of conventional creep deformation (pre-aged, T87) and creep deformation in CAF (as quenched, T4) on AA2219 with a same applied stress.

## 2.3 Development of CAF Experimental and Modelling Tools

The studies on material behaviour associated with the CAF process in practical materials, such as aluminium alloys used for panels structure manufacturing, will be of fundamental significance in the evolution and optimization of CAF process. Over the past decades, considerable research has been carried out to investigate and model the CAF operation, including creep/stress relaxation, age-hardening characteristics and formability of aerospace aluminium alloys, in order to fully exploit the CAF technology [60-63].

### 2.3.1 Experimental Investigations

Gangloff et al. [64] studied and assessed an aluminium alloy (AA8090), which is used to form the lower wing skin. The authors conducted various tests and measured the stress relaxation behaviour of the material during CAF. Their experimental results showed that CAF of AA8090 reduced the toughness but improved fatigue crack growth resistance. Creep age forming of non-age hardenable alloys like 5XXX series alloy, used for the fabrication of fuselage shells, was studied by Jambu et al. [65, 66]. Creep tests and stress relaxation tests were carried out at different temperatures to study the thermal stability and mechanical property evolution. Their experimental results showed that CAF of 5XXX series alloy can be reduced to less than half of the original CAF duration without deteriorating alloy properties.

A number of experiments and microscopy examinations were performed for age-hardenable heat treatable aluminium alloys series 2XXX and 7XXX to investigate the material aspects, especially age-hardening response and microstructure evolution of the precipitates during ageing heat treatment [44, 64-69]. For example, Zhan et al. [62] investigated the creep ageing behaviour of AA7050. Through testing, they determined suitable CAF conditions by optimizing the balance between material mechanical properties

and creep-induced deformation behaviour. Jeshvaghani et al. [70, 71] carried out multi-step treatment in creep age forming of AA7075 to decrease springback and exfoliation corrosion susceptibility without reduction in tensile properties. The results showed that the multi-step heat treatment resulted in low springback and the best combination of exfoliation corrosion resistance and tensile strength. Starink et al. [69] reviewed the metallurgical principles applied to high formability of AA2024 and studied a series of experiment and calculations for various aluminium alloys after simple bending and stretching. Creep age forming of a 2024 aluminium alloy was carried out by Lin et al. [72], their results showed that the precipitation process is more sensitive to the creep ageing temperature than to the external stress. Also, the creep ageing process induced discontinuous distribution of precipitation phases on the grain boundary, which is useful to improve the corrosion resistance of AA2024. Similarly, Lin et al. [73] investigated the effects of the external stress and creep aging temperature on the precipitation hardening in 2124-T851 aluminium alloy, and worked out that the external stress and temperature can alert the competitive precipitation equilibrium of different strengthening phases.

### 2.3.2 Materials and process modelling investigations

CAF is often used to manufacture extra-large panel structure. In order to minimise the cost and experimental time consumption, efforts have been made to develop mathematical models and finite element simulation methods for the CAF operation to predict formability and age-hardening characteristics of aerospace aluminium alloys [40].

For instance, Peddieson and Buchanan [74] carried out a preliminary simulation of creep age-forming of a beam using a model based on linear visco-elasticity and ignoring thermal stresses. Their simulations successfully captured many features of CAF but could not

accurately predict springback. Based on Peddieson's and Buchanan's research, Sallah et al. [75] developed a mathematical beam model, with simply inelastic response, to simulate springback in CAF of circular arc shapes. Jackson et al. [76] studied the application of a unified elastic/inelastic constitutive model to simulate CAF. Narimetla et al. [77, 78] proposed a simulation procedure for CAF of aircraft panels by using an FE plate model. Guines et al. [79] used a traditional power-law creep model to predict the creep deformation, stress relaxation phenomena, which took place during the thermal exposure (creep-ageing stage) in CAF. Ho et al. [43, 54] used a set of creep damage constitutive equations, developed by Kowalewski et al. [80] to describe CAF. They studied the stress relaxation and creep deformation of aluminium sheet under various forming conditions and using a range of sheet thickness. All the above discussed CAF numerical analyses mainly dealt with simple CAF tool shape and conventional elastic-inelastic/visco-plastic material response. Their models ignored thermal stress for simplicity and had not considered for the essential age-hardening characteristics of the material.

Besides the basic creep strain behaviour, the interaction between creep deformation and age hardening has been widely studied in recent years. There have been attempts to mathematically relate process variables (alloy composition, heat treatment temperature and time) with resulting alloy strength or hardness, based on physical principles. For instance, Shercliff and Ashby [81] developed a process model to describe age hardening of aluminium alloys based on thermodynamics, kinetic theory and dislocation mechanics. With a few assumptions and simplifications, while still retaining the essential features of ageing, their proposed process models provided a description of the evolution of the precipitation reaction and the relationship between the microstructure and the strength for aluminium alloy 2XXX and 6XXX series. Poole et al. [82] developed a model for the age-hardening response in

AA7030 that describes the effect of two step ageing treatment and the effect of deformation on the kinetics of ageing. Their model also described the essence of the experimental observations the alloy subjected to deformation before artificial ageing. Based on strain energy, Kashyap et al. [83] developed two step ageing model for aluminium alloy 7010 by taking into account the coherency of strain between precipitates cluster and matrix. Ho et al. [54] developed a set of constitute equations, which models the precipitate nucleation, growth and primary and secondary creep deformation for AA7010 aged at 150 °C. Ho's material models have been successfully introduced into FE solver to predict the creep deformation, stress relaxation, springback and the increase in yield strength of formed part. However, Ho's equations are only suitable for aluminium alloy with spherical precipitates mechanism, because there is only one parameter (the radius of precipitates) to consider the effects of precipitate hardening on creep deformation. Further efforts have been made by Zhan et al. [62] to develop new mechanism-based creep ageing constitutive equations for aluminium alloys with different forms of precipitates under different CAF conditions. These equations entirely model the CAF mechanism combining the interaction between mechanical property evolution and creep deformation under CAF. These constitutive equations are also used in this research and will be fully discussed in Chapter 4.

## 2.4 Experimental Investigation of Springback

During CAF, the key challenge is to accurately predict the amount of springback that will arise after CAF, so that the tool and CAF process can be designed to compensate for springback effects [84, 85]. To deal with this issue, integrated numerical models have been developed by several researches to evaluate springback in creep age formed components from

thick aluminium sheet using physically-based creep constitutive equations. These models are often combined with experimental investigations to examine springback in forming processes [52, 86].

Simple experimental devices have been developed to examine stress relaxation and springback during CAF. However, these are generally based on single curvature bending conditions. The range of typical cylindrical testers which can be used for CAF features investigations are shown in Figure 2.7. A number of CAF tool designs have been studied in the literature as illustrated in Figure 2.7(a)-(e) where the initial undeformed and fully loaded configurations are shown. These CAF tool designs are next reviewed.

Huang [87] carried out forming tests on an aluminium alloy, AA2324, using a single tool with a cylindrical surface, as shown in Figure 2.7(a). The rectangular workpiece was pressed onto the tool's surface and clamped at both ends, generating an initial bending stress in the workpiece. Creep forming and stress relaxation took place and the springback phenomenon was investigated. This tool configuration is further investigated in this work.

Ho et al. [43] employed a testing device that was similar to a four point bend rig, as shown in Figure 2.7(b). This design provided an effective method to study the effect of the initial stress level on creep deformation, stress relaxation and springback. Springback features were investigated after CAF forming AA7010 at 150 ℃ , for different ageing periods and loading conditions.

Jeshvaghani et al. [70, 71] examined the effects of CAF time and temperature on the mechanical properties of AA7075. Samples were prepared, as shown in Figure 2.7(c), by pressing the workpiece between two dies, achieving full contact. The upper and lower die

were then bolted together and isothermally heated in a furnace for a specified ageing time and temperature.

Miller et al. [88, 89] developed a bend-stretch forming device to achieve a cylindrical profile, a schematic of which is shown in Figure 2.7(d). The workpiece was gripped in a collet and the die advanced towards the workpiece, causing the collet to rotate and remain tangential to the ends of the workpiece. Finally, the die was retracted and workpiece removed. Though this was a cold forming process, it provides a reference method for CAF investigations.

Zhang [90] designed a cantilever bending test device, as shown in Figure 2.7(e), and studied the influence of a number of parameters including temperature, time and curvature radius on the aluminium alloy 2A12CZ. However, this testing device resulted in various complex creep deformation/stress relaxation due to the non-uniform distribution of bending moments along the length of the workpiece.

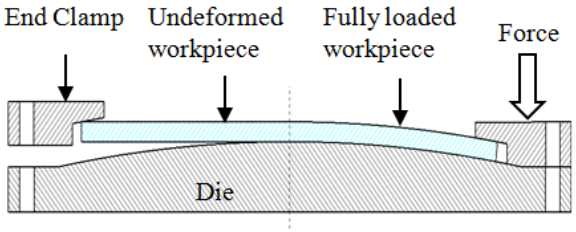


(a) End clamp bending device [87]

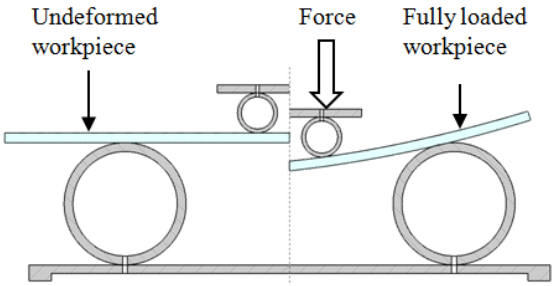


(b) Four point bending device [43]

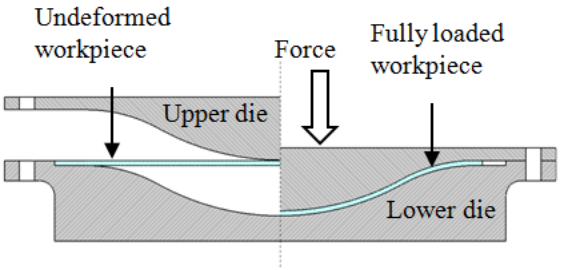


(c) Upper and lower die bending device [70, 71]

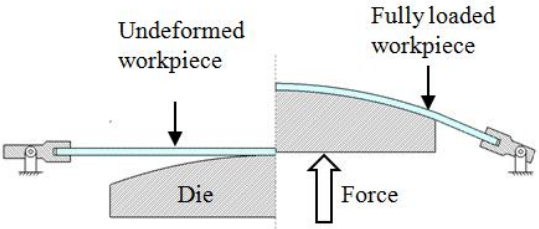


(d) Bend-stretch device [88, 89]

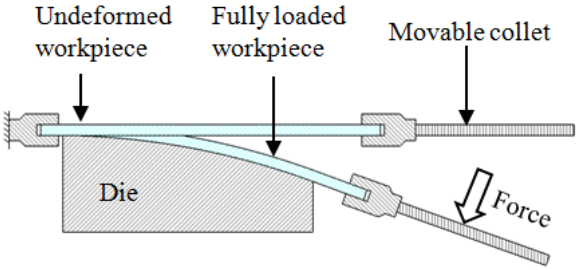


(e) Cantilever bending device [90]

Figure 2.7: Schematic of curvilinear devices developed for CAF springback.

## 2.5 Summary

Numerous efforts have been made to investigate, model and hence improve the industrial CAF. Due to specific requirements of the process, both experimental and modelling techniques need to be addressed. Also, current state of the art shows that:

- CAF is suitable for the production of extra large shell structure components, which are made of heat treatable materials and for which, stress relaxation takes place at their artificial ageing temperatures.
- CAF combines the material heat treatment and forming in one operation, and thus reduces energy in production.
- Springback will occur in CAF. Thus, the process and modelling work should be concentrated on springback evaluation, with the aim of designing an appropriate tool shape to compensate it.
- Significant experimental investigations need to be carried out to characterise both the stress relaxation behaviour and age hardening mechanism. A set of unified creep-ageing constitutive equations should be used and calibrated from experimental data, to enable the physical and mechanical property evolution to be modelled during CAF processes. Thereafter, a set of constitutive equations can be implemented into commercial FE process simulation packages, for process optimisation and appropriate tool design, in order to compensate springback.

The current research is concentrated on constitutive modelling of the creep-ageing behaviour of candidate aluminium alloy 2219 during artificial ageing and developing a practical process to validate and predict stress relaxation behaviour, age-hardening, springback and related work in CAF.

# CHAPTER 3

# Experimental Investigations on the Creep Age Hardening and Stress Relaxation Behaviour of Aluminium Alloy 2219

## 3.1 Introduction

This chapter contains a description of an experimental investigation of creep ageing behaviour of an aluminium alloy AA2219 at a high temperature of 175 °C. Two experimental programmes have been designed to characterise the creep-ageing and stress relaxation behaviours of Aluminium Alloy 2219 under thermal exposure conditions. Both creep-ageing tests and stress relaxation tests have been performed for a range of stress level at 175 °C.

## 3.2 Experimental programme

### 3.2.1 Test material

The creep ageing test specimens, of composition shown in Table 3.1, were machined from AA2219-T87 base plates in the rolling direction. Each test specimen was 90 mm long and had a gauge length of 37.5 mm for creep strain measurement. The dimensions of the specimen are shown in Figure 3.1. Prior to creep ageing and stress relaxation tests, the specimen was solution heat-treated at 535 °C for 1 hour and water quenched immediately to get the material in T4 condition. Subsequently, the samples were kept in a low temperature control zone (15 ℃ ) to reduce natural ageing.

Table 3.1: Material compositional elements of aluminium alloy 2219, wt %

| *Cu* | *Mn* | *Si* | *Fe* | *Ti* | *Cr* | *Al* |
|---|---|---|---|---|---|---|
| 6.3 | 0.3 | 0.2 | 0.3 | 0.06 | 0.18 | Remainder |

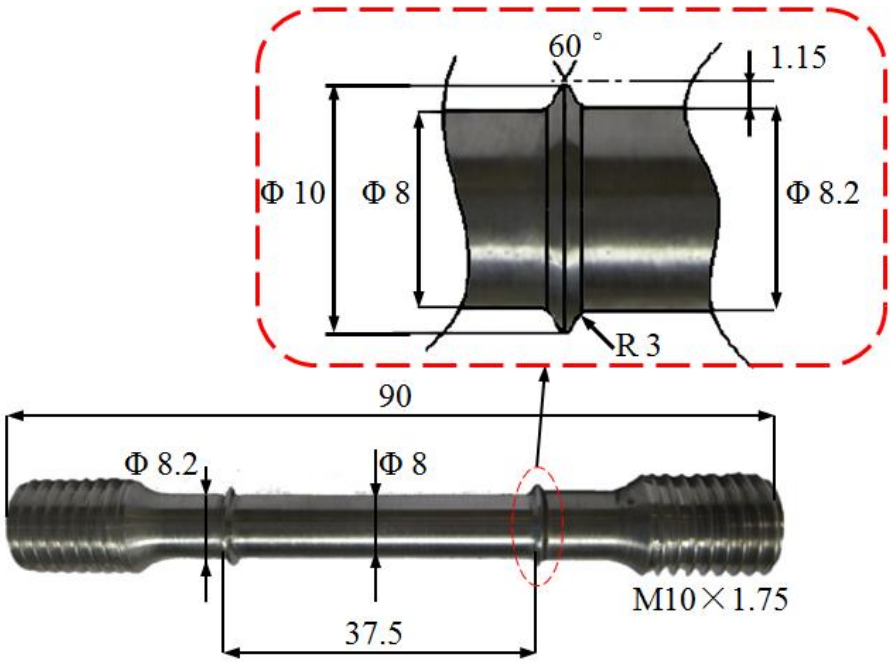


Figure 3.1: Test-piece design with extensometer ridges. (all dimensions are in mm)

### 3.2.2 The overall test programme

In order to capture the CAF mechanism for AA2219, two types of experiments were performed: one was a uniaxial creep-ageing test, and the other one was a uniaxial stress relaxation test. The overall test program is shown in Figure 3.2. Detailed experimental procedures and results for creep-ageing and stress relaxation are given in the following sections of this chapter.

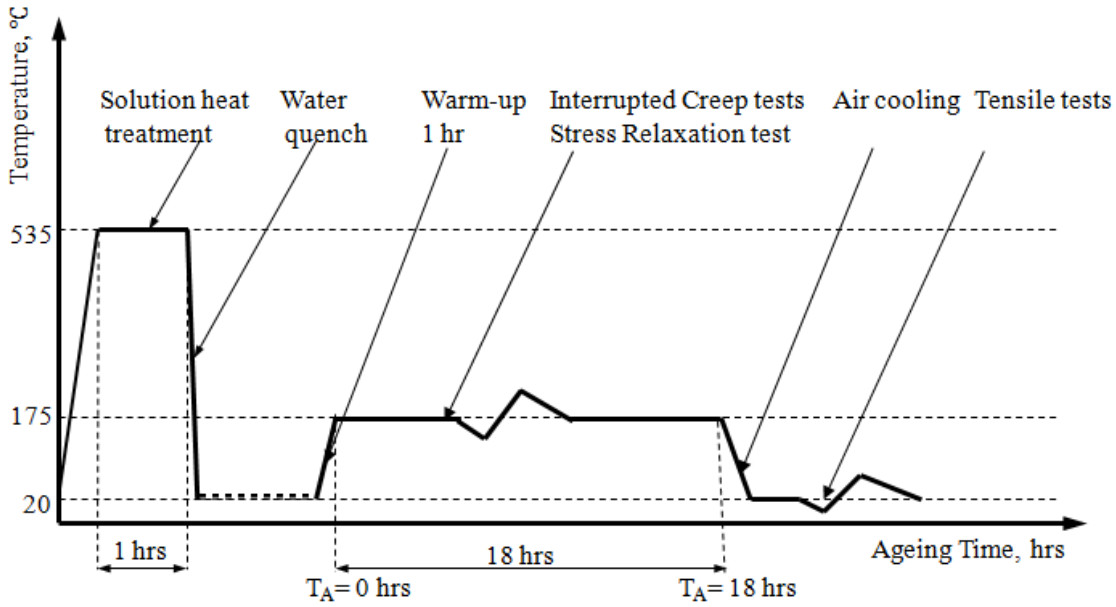


Figure 3.2: Material preparation and test program.

## 3.3 Creep-Ageing Tests

### 3.3.1 Aims

The aim of performing this test was to investigate both the creep and ageing behaviour of AA2219 under constant stress for a controlled amount of time (e.g. 18 hours) at 175 ℃ . This test is very similar to the conventional creep test, apart from the fact that the material used was solution heat-treated and quenched. Therefore, the material was expected to be initially less strong but to exhibit a lot of hardening during the test. The hardening can be attributed to ageing due to thermal exposure and to creep deformation. At the end of the test, the material's yield strength was expected to increase due to the age hardening mechanism.

### 3.3.2 Experimental equipment

The creep tests were conducted on a PHONEIX constant load creep machine (Figure 3.3) in the High Temperature Testing laboratory at Imperial College London. The creep machine consists of a closed furnace with three built-in thermocouples. To measure the

specimen temperature more accurately, two additional thermocouples, which were tied to the surface of the material in the gauge length area, were used to measure the temperature directly from the material. The creep machine was fitted with an auto balanced lever system that can sustain a constant load on uniformly deforming specimens.

The extension was measured using two linear capacitor gauges, which are fitted on the samples' ridges to measure specimen extension through a FREQ 1MP-AB modular system equipped with two dual transducer amplifier modules. The transducers can measure the testpiece elongation up to 2.2 mm (a totally strain of approximately 2.0 %).

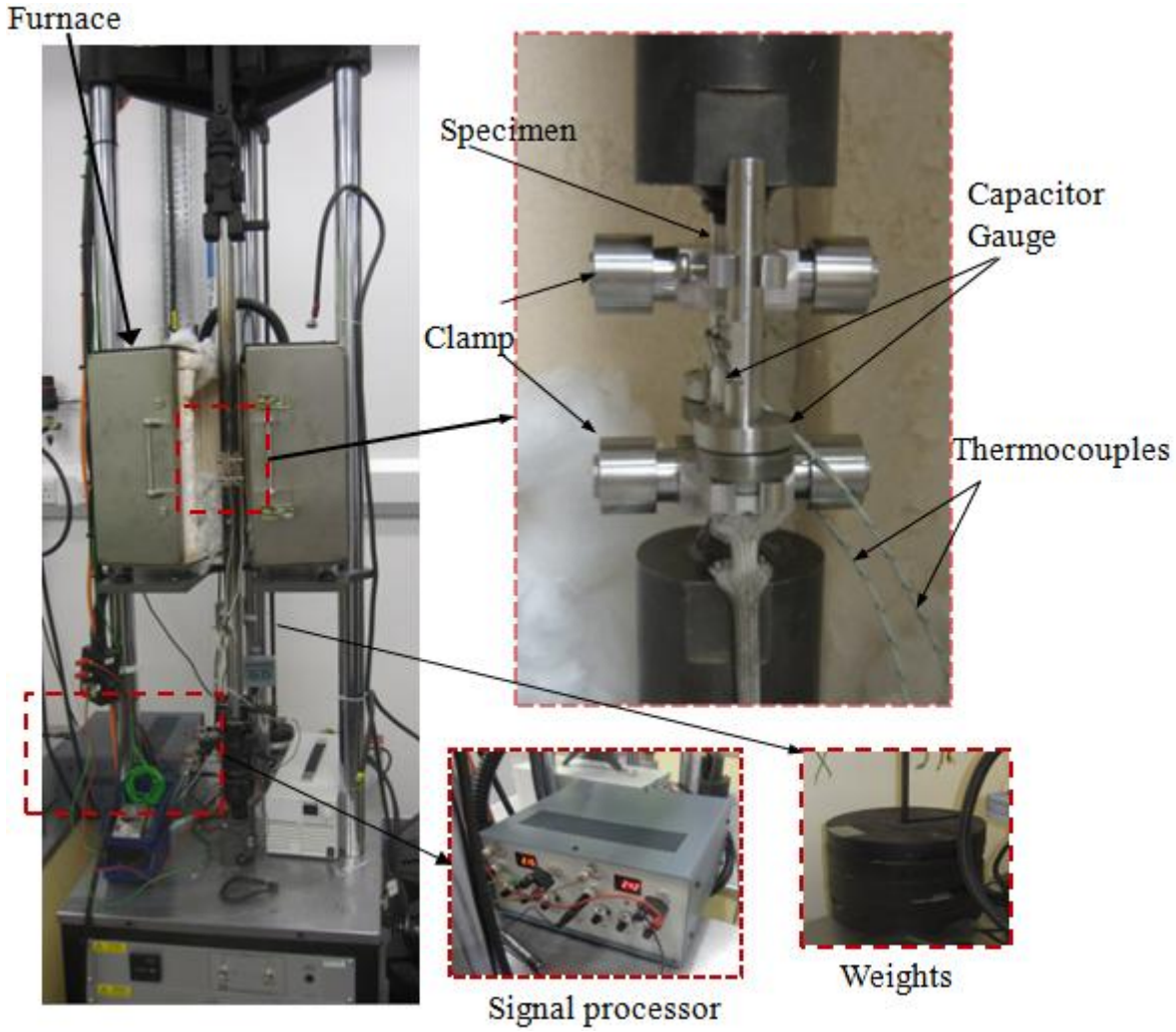


Figure 3.3: Creep-ageing experiment set-up.

### 3.3.3 Experimental procedures

Constant stress creep tests were carried out at 175 ℃ for stress levels of 125.0, 137.5, 150.0, 162.5, 175.0, 200.0, 225.0, 237.5 and 250.0 MPa for the specimens prepared in AA2219-T4 condition. The total test duration was 18 hours, which is approximately similar to the duration for a complete industrial creep-age forming process. Meanwhile, interrupted creep-ageing tests (e.g. 6 hours, 12 hours) were performed to determine the creep-ageing behaviour. The experimental procedures for 18 hours creep-ageing test are briefly described as follows:

- First, the specimen was fitted and aligned in the middle of the furnace. Two additional thermocouples were tied to the specimen gauge area surface and a pair of extensometers was fitted to measure the extension.
- The furnace was closed and the heating was switched on. Super wool was used to cover the top and bottom of the furnace to reduce heat loss.
- When the temperature stabilized at 175 ℃ , the load was applied and the elongation of the specimen was measured by the capacitor gauges.
- The extension was measured by two capacitor transducers every 10 second initially for the first hour. The time interval was then increased to 30 seconds for the rest of experimental period.
- The data logger was stopped when the time reached 18 hours. The heating was switched off and the furnace was opened and the load was removed.
- When the specimen was cooled down to room temperature, the specimen was moved on an Instron machine to measure the uniaxial tensile properties (Figure 3.4). The longitudinal strain was measured by an extensometer with a resolution of 0.01 mm over a gauge length of 25 mm.

The interrupt creep-ageing tests (6 hours and 12 hours) were repeated for the test specimens prepared in the T4 condition using selected stress levels, e.g. 150.0, 175.0, 200.0 MPa. Also, to compare the ageing effect in details, stress-free ageing of AA2219 was performed every 2 hours with the measurement of mechanical properties thereafter.

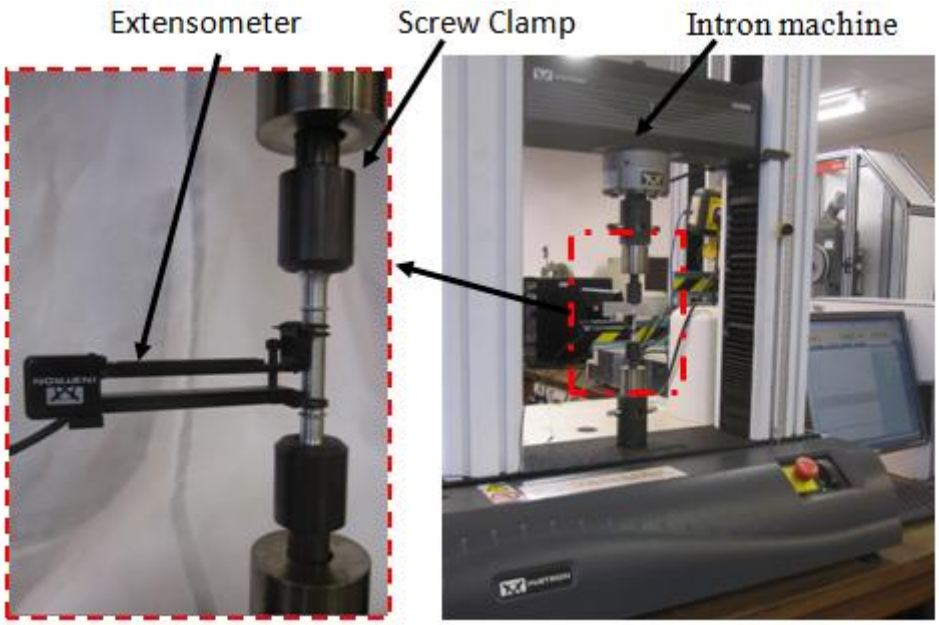


Figure 3.4: Tensile experiment set-up after interrupted creep tests.

### 3.3.4 Results and Discussion

Figure 3.5 (i) showed the evolution of creep strain curve for AA2219 at 175 °C for a total duration of 18 hours, while Figure 3.5(ii) illustrated the creep evolution at the initial period (up to 1.2 hours). For stress level lower than 200 MPa, all creep strain curves show a similar trend. Similar to typical creep curves, these curves were characterized by a primary stage of decreasing creep rate followed by a secondary stage of constant creep rate. As shown in the figure, higher stress level results in higher creep strain rate. When the stress level is relatively low, e.g. stress level equals 100 MPa, the minimum creep strain rate is almost zero and the creep strain is very low.

(a) Stress levels from 75 MPa to 137.5 MPa

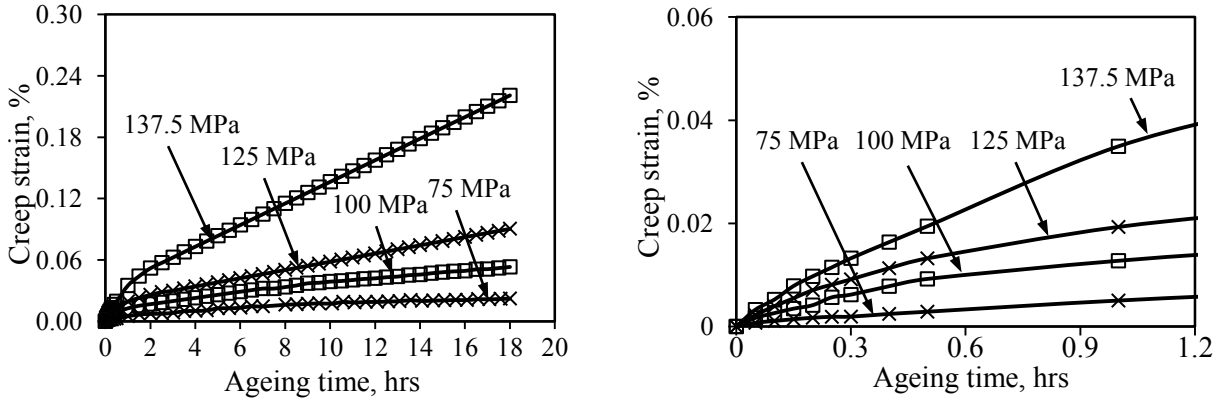


(b) Stress levels from 137.5 MPa to 200 MPa

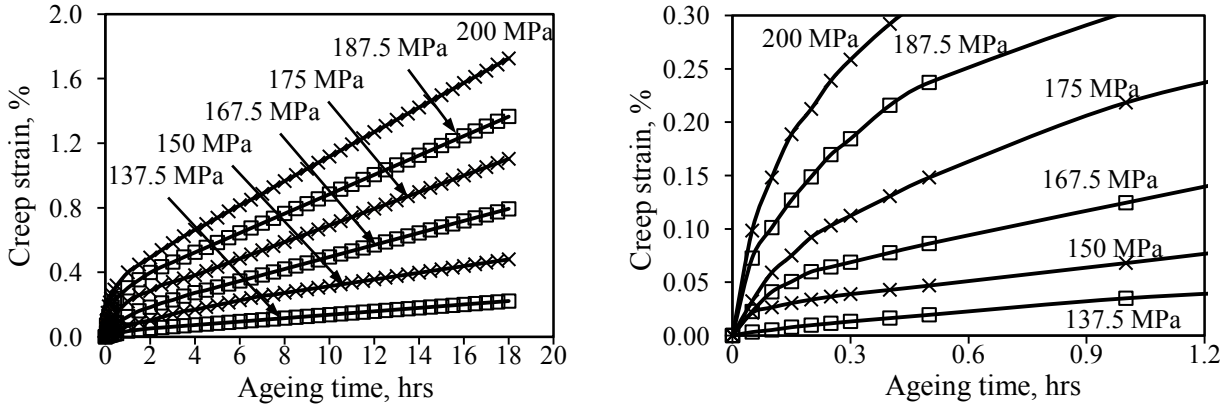


(c) Stress levels from 200 MPa to 250 MPa

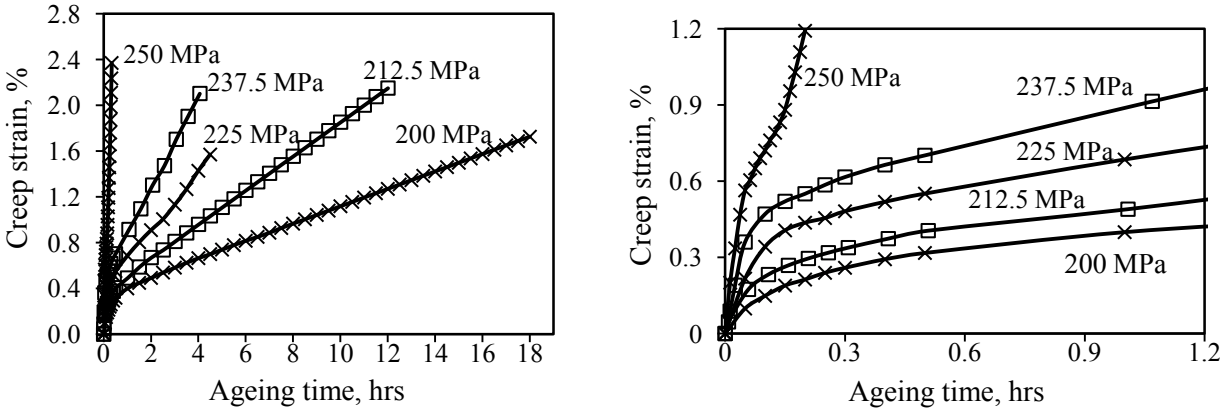


(i) The Complete creep strain curve (ii) Creep strain curve up to 1.2 hrs

Figure 3.5: Experimental creep strain curves obtained at (a) Stress levels from 75 MPa to 137.5 MPa, (b) Stress levels from 137.5 MPa to 200 MPa and (c) Stress levels from 200 MPa to 250 MPa, for the ageing time up to 18 hours.

Comparing the results in stress level between 137.5 MPa and 200 MPa, more creep strains are observed. For example, at the end of the test, for a stress level of 150 MPa, the creep strain is approximately 0.46% while it is 1.32% for a stress level of 187.6 MPa.

High initial stress levels induce a faster tertiary stage and accelerate the creep strain rate. For example, for a stress level of 212.5 MPa, tertiary creep occurred at $T_A = 9.5$ hours and the sample failed at $T_A = 16$ hours, while for a stress level of 250 MPa, there is no obvious secondary creep taking place; tertiary creep took place at approximately $T_A = 0.2$ hours and the specimen broke after 1.2 hours.

It can be summarized from the tests that the higher the stress level, the shorter the primary stage lasts and higher the initial creep rate reaches. While in the secondary creep stage, the minimum strain rate remained almost constant, and the effect of higher stress levels became weaker than that on the primary stage. In addition, with the further increase in stress level, tertiary stage creep may take place and it shortens the secondary creep.

Figure 3.6 shows a plot of creep strain rate, $\dot{\varepsilon}$, against stress, $\sigma$, for the tested material at initial and minimum creep stage for the stresses level between 75 MPa and 225 MPa. Four phenomena can be summarized from the figure. Firstly, the creep strain rate at the initial stage is higher than that at the minimum stage. Secondly, the creep rates at lower stress levels are smaller than that at higher stress levels. Thirdly, both initial and minimum creep strain rate increased with increase of stress level. Lastly, the relationship between stress and initial or minimum creep strain rate in log scale are linear for both cases. Thus, if a primary and secondary CAF test is performed for a stress level in between 75 MPa and 225 MPa, the creep strain rate is expected to lie between these two curves.

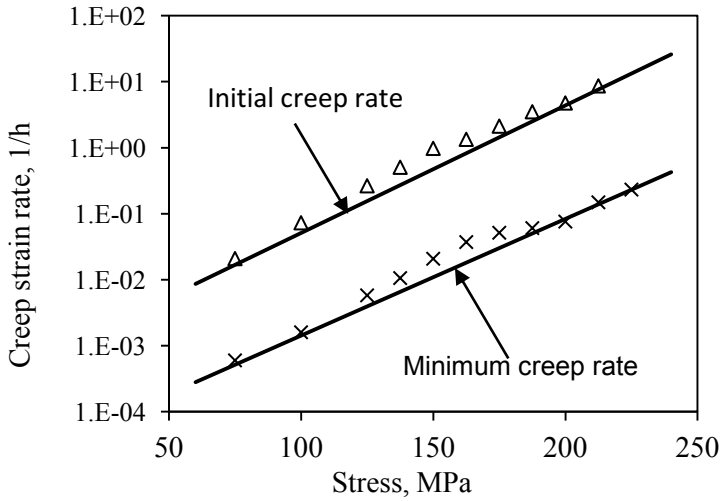


Figure 3.6: Experimental creep strain rates at the initial and steady state.

Figure 3.7 shows the engineering stress-strain curves of crept samples aged at 175 °C for 18 hours, compared to the same samples aged in stress-free condition with different ageing time. It is noted that the effective ageing time, $T_A$ , initiates when the testing environment stabilized at 175 °C after 1 hour. Thus, an AA2219-T4 material (as quenched) is tested to compare with the other condition samples. From free-stress ageing curves, the strength increased with ageing time. The strength increased significantly during the first 6 hours and slowed down thereafter. After 12 hours of ageing, there is no significant increase in the strength properties, compared to the stress-free samples aged for 18 hours. While for stress-ageing samples with 18 hours ageing, further increase in strength can be observed. Higher stress level crept specimen result in higher strength properties. In addition, higher strength properties corresponded to lower ductility.

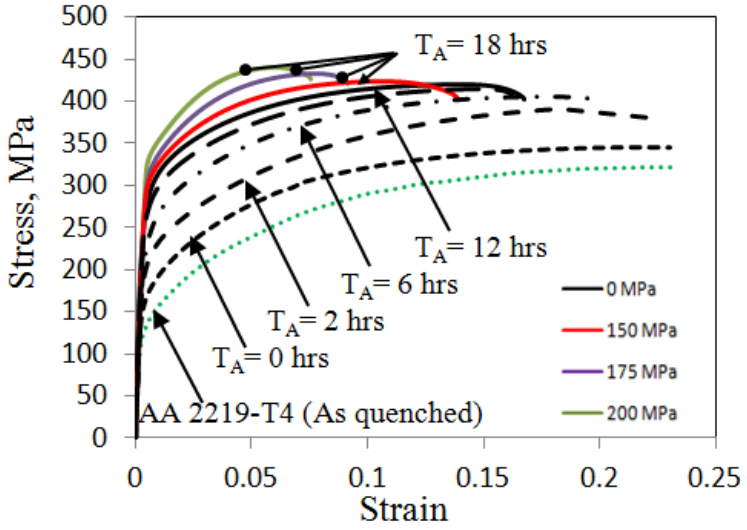


Figure 3.7: Comparison of stress-strain relationships of AA2219 treated at different creep-ageing conditions.

Plots of yield stress, ultimate tensile strength and elongation (up to ultimate tensile strength) as a function of ageing time at 175 °C for both stress-ageing and free-ageing condition are illustrated in Figure 3.8. Referring to Figure 3.8(a), the yield stress (0.2% proof stress) increases more quickly under stress-ageing conditions compared with stress-free condition at the initial ageing state e.g. 6 hours. The yield stress changes from 262 MPa to 309 MPa when the applied stress level varies from 150 MPa to 200 MPa after 6 hour stress-ageing, while the yield stress is only 243 MPa for stress-free-ageing at the same ageing time. In addition, the ageing time to each peak value decreases obviously with increasing applied stress level. The peak ageing time is approximately 20 hours for stress-free conditions, around 18 hours for stress-ageing at 150 and 175 MPa. In terms of ultimate tensile strength (Figure 3.8(b)), the initial increase in strength giving rise to a fast increasing rate after a relatively short period, and then the increase of yield stress begins to decrease rapidly. For example, the UTS of free-stress condition increased from 345 MPa to 405 MPA after 6 hours ageing and it increased only 9 MPa after another 6 hours. The increase in UTS is not as significant as the increase in yield stress. The peak UTS values achieved at an ageing time of

18 hours were 417, 426, 432, 440 MPa for stress free conditions at initial stress 150, 175, 200 MPa conditions. After 18 hours, the UTS decreased with the ageing time. From Figure 8(c), the elongation at UTS deceased with increasing of ageing time for both stress-free and stress-ageing condition. Moreover, elongation decreased with the increasing of experiment applied initial stress at the same ageing time. When ageing time equals 18 hours, the elongation were 12.41%, 10.43%, 7.67%, 6.1% for stress-free condition, 150 MPa, 175 MPa, and 200 MPa respectively.

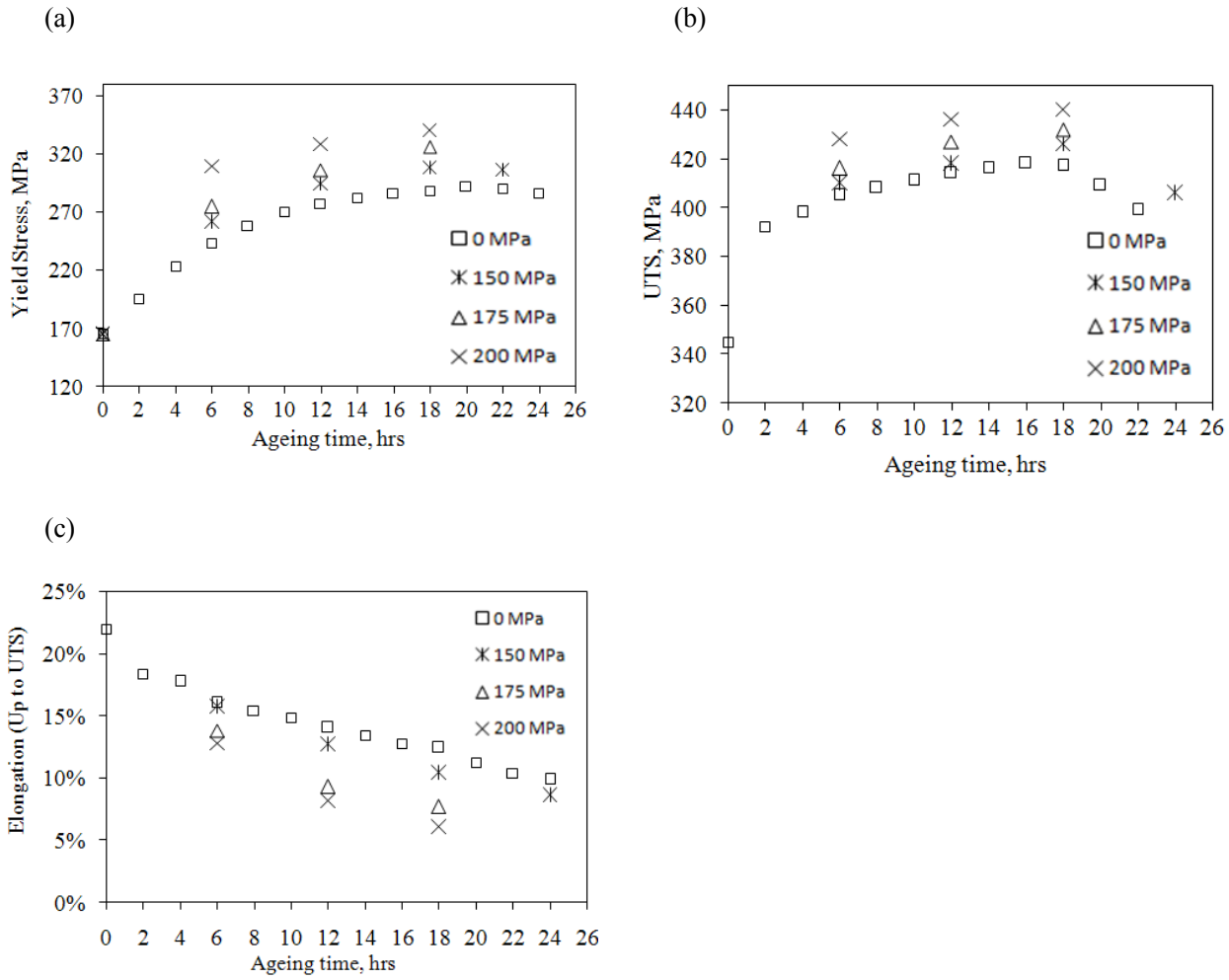


Figure 3.8: Comparison of (a) yield stress, (b) ultimate tensile stress (UTS) and (c) Elongation for AA2219 at different creep-ageing conditions at UTS.

## 3.4 Stress-Relaxation test

Stress induced in forming of large curvature components is sometimes very high and the stress level at or close to the sheet surface may significantly exceed the material yield strength. In a CAF process, stresses will be relieved by thermal exposure. The higher the initial stress level, the higher the stress relaxation rate that can be achieved. As time goes on, the stress relaxation rate will decrease according to a pattern of power law or sinh law. Stress relaxation behaviour dominates during the early period of CAF. Similarly, tests were performed to investigate the stress relaxation behaviour of AA2219 at a temperature of 175 ℃ .

### 3.4.2 Experimental equipment

Uniaxial stress relaxation was carried out on an Instron 5588 machine available in the PACT lab at Imperial College London. The machine has a maximum load capacity of 150 kN. An Instron environmental chamber (Model No.EC1613A, 550×215×460 mm internal dimension), was used to provide the constant heating for the specimen. During the test, a thermocouple was tied on the centre of the specimen surface to monitor the temperature. The load, displacement and force data were logged to the computer and recorded through the experiment. Figure 3.9 shows the experimental setup for stress relaxation test.

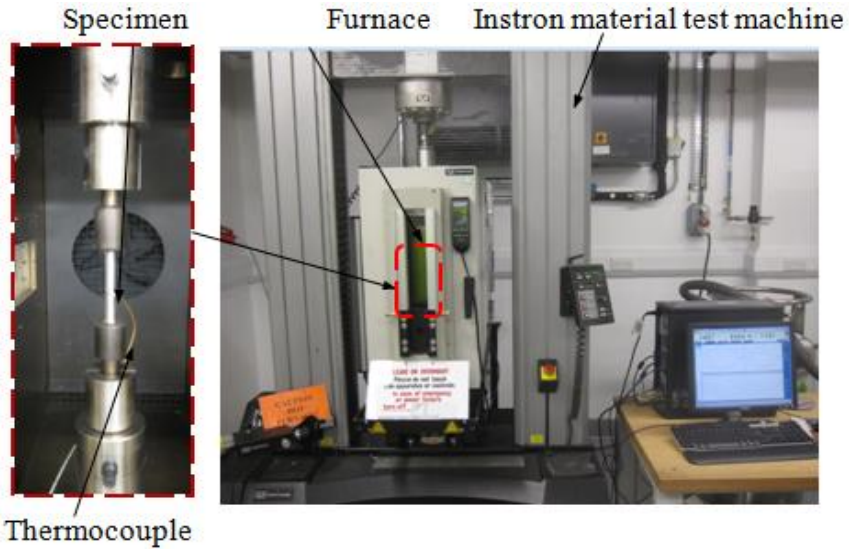


Figure 3.9: Stress relaxation ageing experiment set-up.

### 3.4.2 Experimental procedures

The specimens used were prepared in the same condition to the specimen used in the creep-ageing test. Prior to the experiment, the T4 condition specimens were stored in a steady 15 ℃ place to avoid nature ageing.

Stress relaxation tests were carried out for five target stokes, where the initial engineering stress reached 125, 150, 175, 200, 225 MPa. The total duration for each test was 18 hours. The experimental procedures are described below:

- The specimen was fitted into the screw grips. The cross head connected to the screw grips was adjusted slowly and carefully in stretching direction, so that specimen was just tight in place and any slack was removed.
- The furnace was closed and the heating was switched on. Super wool was used to cover the top and bottom of the furnace to reduce heat loss. The heating took up to 1 hour for the specimen and connected grips stabilized at 175 ℃ . This action avoided the thermal expansion effects on the specimen clamping tools, which would release the clamping force between the specimen and tools in tension direction and result in errors in the

measurement.

- Thereafter, a preload of 25 N was applied to make sure that no slipping would occur during the test, which would have affected tension loading results later.
- Once the preload was achieved, the specimen continued to be loaded at a constant cross head stroke rate 2 mm/min, until the target initial stress was achieved.
- When the target initial stress was achieved, the cross head was kept at the same position, while the stress relaxed. Throughout the experiment, the force/stress history was recorded every 10 second initially for the first hour and then increased to 30 seconds for the rest of the experimental period.
- After 18 hours, the recording was stopped and the results were processed.

### 3.4.3 Results and discussions

Figure 3.10(a) shows the complete stress relaxation experimental curves for AA2219 at 175 ℃ . For a better illustration, stress relaxation at the initial period (up to 1.2 hour) is shown in Figure 3.10(b). The initial stress levels are 125, 150, 175, 200, 225 MPa. Each curve represents the average stress relaxation result of two specimens. The differences in the measured stress relaxation curves between the two specimens for each stress level are no more than ± 8.2 MPa.

Assuming the change of cross-sectional area is negligible, the stress was obtained by dividing the force with the initial cross-sectional area. As illustrated in Figure 3.10(b), the stresses increased at a constant rate initially. Once the target stresses are achieved, the stress curves dropped dramatically in the first hour followed by a gentle decrease. At this stage, the relaxation rate is mainly dependent on the initial stress level, the higher the initial stress is, the higher the stress relaxation rate achieved. For example, for initial stress of 225 MPa, the

stress relaxation rate was 148 MPa/h. While for initial stress of 150 MPa, the stress relaxation rate was only 24 MPa/h. Referring to Figure 3.10 (a), it represents a relatively long period of 18 hours: all the stress relaxation rates decreased to a relatively constant value. It can be also observed that the relaxed stresses are 112 MPa (Initial stress, 225 MPa), 108 MPa (Initial stress, 200 MPa), 106 MPa (Initial stress, 175 MPa), 105 MPa (Initial stress, 150 MPa), 103 MPa (Initial stress, 125 MPa) after 18 hours ageing. From these stress relaxation behaviours, it is believed that all the curves would eventually meet each other for a longer ageing period.

(a)

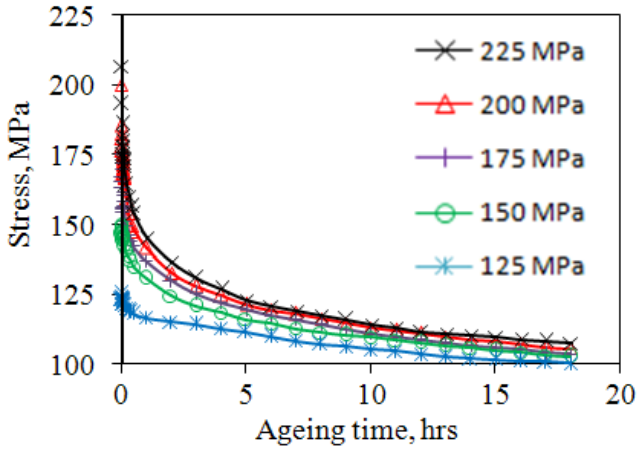


(b)

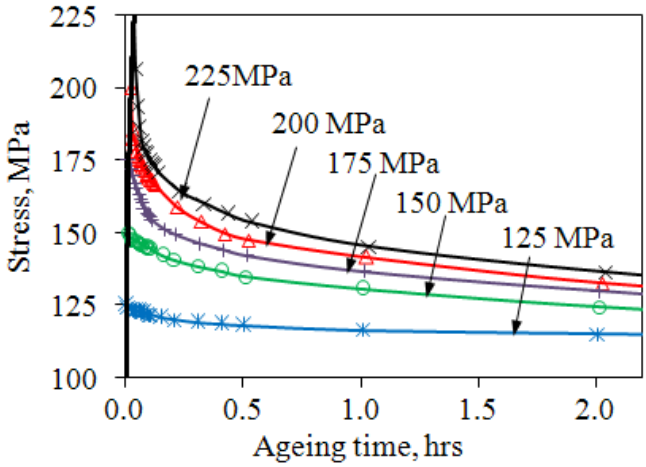


Figure 3.10: The stress relaxation behaviour of AA2219 at 175 ℃ for (a) the whole test period, and, (b) at the initial stage of the tests.

The schematic diagram in Figure 3.11 shows the stress-strain and the corresponding stress-time during a CAF process. The stress relaxation may be due to the thermally activated diffusion, dislocation recovery and creep. When stress relaxation takes place resulting from thermal exposure, the stress level of the material drops sharply from the maximum stress in the initial period of the test. The relaxation rate decreases as the stress level decreases. If the stress relaxation takes for a longer time, all the stress levels are expected to relax to a critical value $\sigma_c$. As shown in Figure 3.11, when stress relaxation occurs largely in the elastic-region, stress level reduces from $\sigma_2$ (below 0.2% proof stress) to $\sigma_c$. The total strain, $\varepsilon_{T1}$, remains constant through the period of time. The amount of the inelastic strain, $\varepsilon_{C1}$, retained by the material after CAF indicates the permanent deformation. In terms of stress relaxation takes place at plastic region, stress level drops significantly from $\sigma_1$ (above 0.2% proof stress) to $\sigma_c$. The total strain, $\varepsilon_{T2}$, is the constant value throughout the period of ageing. The residual elastic strain, $\varepsilon_{e2}$, springs back after unloading. The permanent deformed shaped is characterized by the amount of inelastic strain, $\varepsilon_{P2}$, and $\varepsilon_{C2}$. Also, the residual stress levels during CAF are expected to achieve the same level, which improves component shape stability after unloading.

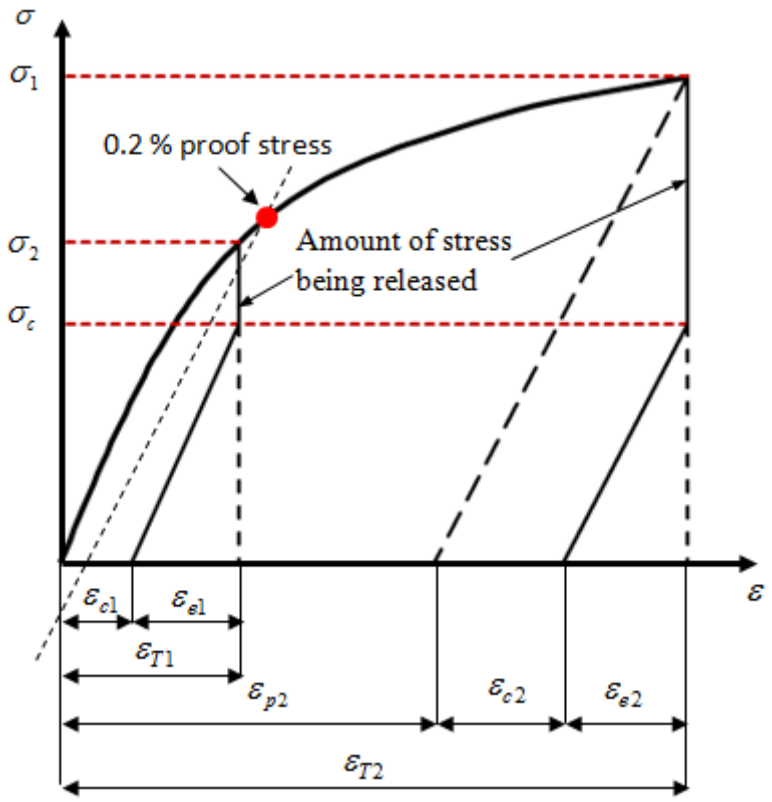


Figure 3.11: Stress relaxation ageing behaviour of the material.

## 3.5 Summary

Creep age forming consists of a combination of age-hardening, creep, and stress relaxation. Creep-ageing and stress relaxation experiments have been carried out in this research to investigate and study the material behaviour of AA2219 in T4 condition subject to CAF.

In the creep-ageing experiments, the creep ageing deformation of the material is very similar to the primary creep behaviour in conventional creep deformation. The material shows a lot of hardening during the test, because the material initially is not artificially aged, the material is soft or 'less strong'. The constituents of the material precipitate upon thermal exposure and creep deformation induced hardening increases the strength but deceases the ductility of the material by the end of the test.

In stress relaxation experiments, the stress level of the material drops sharply from the maximum stress at the initial period of the test. The relaxation rate decreases as the stress level decreases. This kind of relaxation pattern can be modelled using a power law or sinh law. It is also noted that for a long period time, all the stresses are expected to relax to a similar level at a critical load.

# Chapter 4

# Constitutive Modelling of Creep Ageing Behaviour of Aluminium Alloy 2219

## 4.1 Introduction

CAF is a hybrid process of forming and age-hardening. During CAF, the evolution of mechanical properties of the material is complicated because age-hardening occurs simultaneously with creep deformation. Thus 'creep-ageing' behaviour in CAF is different from that of conventional creep behaviour. Based on the experimental investigation of the creep-ageing behaviour of AA2219 in Chapter 3, a set of physically-based, unified constitutive equations (developed by Zhan et.al [53]), which enables the modelling of the evolution of both physical and mechanical properties of the material in CAF, has been adopt in this chapter. The material constants within the equations are fully determined from experimental data of AA2219 using an evolutionary algorithm. The material model has been integrated with the commercial FE solver ABAQUS via user defined subroutine, CREEP, for CAF process modelling. In addition to springback and stress relaxation, the evolution of age hardening and evolution of yield stress during CAF were predicted.

## 4.2 Age-Hardening Mechanism

### 4.2.1 Age hardening

Age-hardening or ageing refers to a mechanism that takes place at the artificial ageing stage of a heat treatment process, which is commonly used to improve the mechanical

properties of commercial aluminium alloy. It is only applicable to heat-treatable aluminium alloys, including aluminium alloys 2XXX (Al-Cu), 6XXX (Al-Mg-Si) and 7XXX (Al-Zn), which are commonly used for aerospace and automotive applications [45, 91] .

### 4.2.2 Heat treatment

The purpose of heat treatment is to alter the mechanical strength of an aluminium alloy: either to make the alloys soft and ductile for forming operations, or to make the alloys strong to achieve a specific mechanical strength. It is designed to alter the mode of occurrence of the soluble alloying elements, particularly copper, magnesium, silicon and zinc, which can combine with one another to form inter-metallic compounds in the form of fine distributed precipitates [92-94]. Figure 4.1 (a) shows the Al-Cu phase diagram for heat-treatable 2XXX series aluminium alloy. Typical heat treatment involves the following stages [95, 96]:

- Solution heat treatment (SHT) at high temperature, $T_0$, within the single phase region, to dissolve the alloying elements.
- Rapid cooling or quenching across the solvus line, usually to room temperature. This leads to a meta-stable supersaturated solid solution (SSSS) at $T_1$. Equilibrium structure should be $\alpha + \theta$, but limited diffusion does not allow $\theta$ forming.
- Ageing heat treatment, where SSSS is heated to $T_2$. SSSS decomposes to form a finely dispersed precipitate. This stage is usually achieved by artificial ageing.

Figure 4.1(b) shows a typical temperature profile during a full heat treatment process. Because of complex interactions that take place during the processes of heat-treatment, different alloys have different characteristics that need appropriate selection and control of the heating operations and specific combinations of temperature and time [95, 96].

(a)

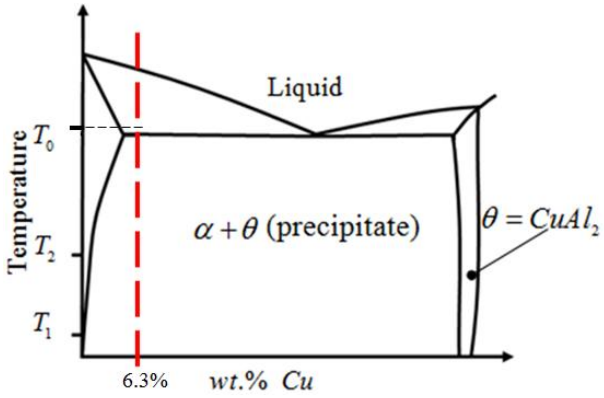


(b)

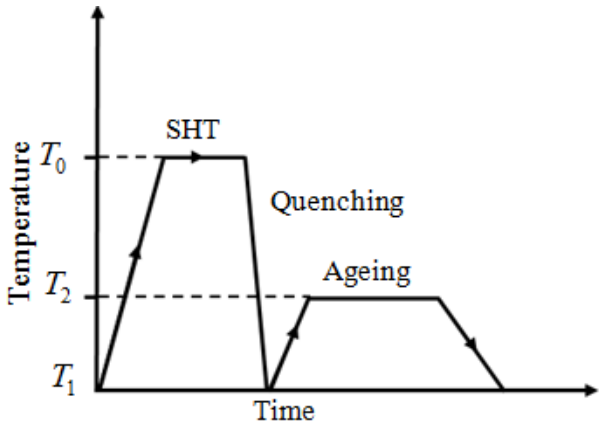


Figure 4.1: (a) The Al-Cu phase diagram for heat-treatable 2XXX series aluminium alloy, (b) A typical temperature profile for the heat treatment based on Al-Cu phase diagram [95].

### 4.2.3 Microstructure evolution of age-hardening mechanism

The ageing behaviour of 2XXX aluminium alloys under isothermal heat treatment has been examined in detail by several researchers [97-99]. The generally accepted ageing sequences is:

$$\alpha_0 \rightarrow \alpha_1 + GP \rightarrow \alpha_2 + \theta'' \rightarrow \alpha_3 + \theta' \rightarrow \alpha_4 + \theta$$

where α is the single phase solution of Al and Cu , GP is the Gruinier-Prestion zones. $\theta$" and $\theta$' are transitional phases of the inter-metallic precipitates $\theta$, $CuAl_2$. The subscripts on $\alpha$ refers to the decreasing Cu composition in the $\alpha$-phase as it precipitates out of solution. The microstructure evolution sequence for Al-Cu system is shown in Figure 4.2.

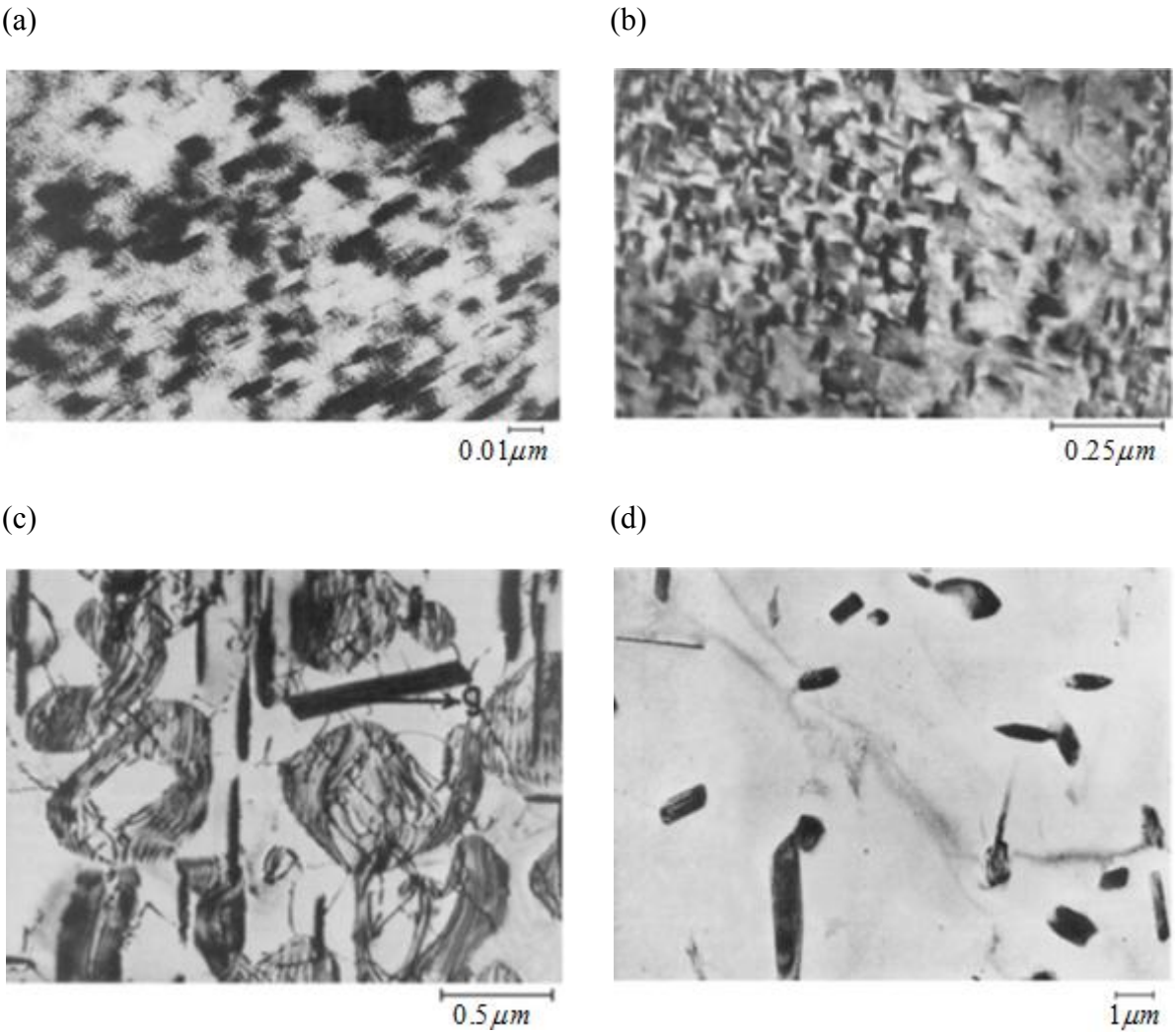


Figure 4.2: Transmission electron micrographs of precipitation sequence in AA2219, (a) GP zones at 720,000×, (b) $\theta$" at 63,000×, (c) $\theta$' at 18,000×, (d) $\theta$ at 8,000× [100].

### 4.2.4 Representation of precipitates formation and growth

Upon ageing, the quenching process retains the supersaturated solid solution within the aluminium matrix. At the early stage of ageing, ordered and solute rich clusters, so called GP zones, forms. GP zones are only 1 or 2 atom planes in thickness and retain a similar crystal structure to that of the Al matrix and are coherent. Because of this, their interfacial energy is low, making their nucleation easy. GP zone formation increases the hardness of the alloy, but because the GP zones are small and coherent, they can be cut by dislocations. During this stage, the initial precipitates $\theta$" increases drastically with time and it is disk-shaped and fully coherent with the matrix. Both the GP zone and $\theta$"are weak and coherent and thus shearable by moving dislocations. Further ageing leads to coarsening of the microstructure, the $\theta$" phase is replaced by the more stable phase $\theta'$ and is semi-coherent with the Al matrix. During this stage, the size of the precipitates increases and the number of constituents in the matrix phase steadily decreases, approaching the equilibrium value. Large incoherent precipitates $\theta$ are formed near the peak hardness and are not shearable by dislocations. A change in the dislocation-strengthening mechanism from the particle shearing to bypassing via Orowan looping takes place as the coarsening process proceeds. In addition, precipitate free zones will form adjacent to the grain boundaries because of the nucleation and growth of coarse precipitates at the grain boundaries. The microstructure thus becomes inhomogeneous and quite complex when the material is age hardened [101-103]. Figure 4.3 shows the schematic ageing precipitates for 2XXX series aluminium alloys at different ageing stages. The dark and more or less disc-shape particles are the $\theta$ precipitates. The morphology of these disc-shaped particles are defined by a parameter $A$, which means the mean ratio of radius to half length for the disc-shaped precipitates in 2XXX series aluminium alloy [101, 104].

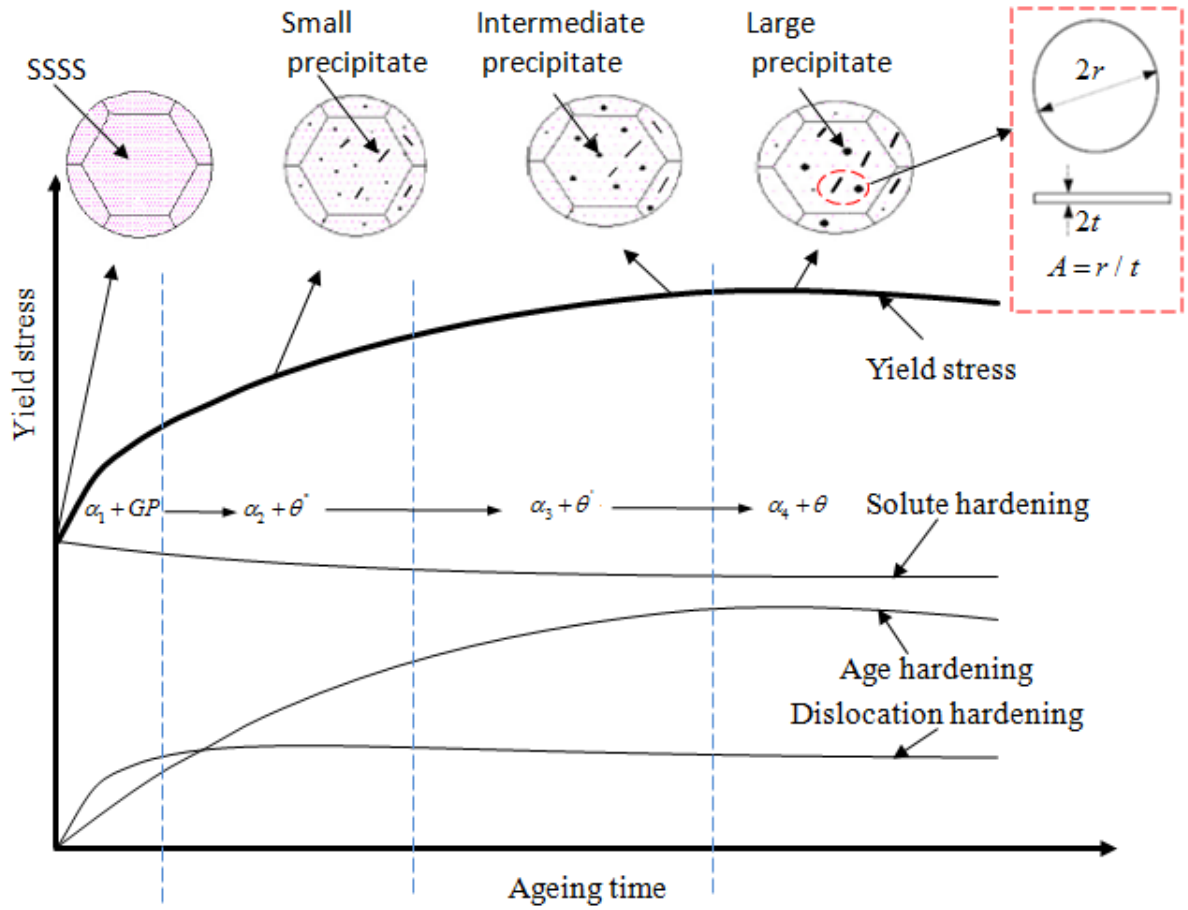


Figure 4.3: Age hardening mechanism for creep age forming of AA2219.

### 4.2.5 Modelling of the evolution of disc-shape precipitates

The evolution of geometric characteristic of precipitates as a function of ageing time and temperature for aluminium alloy with disc shaped precipitates has been modelled by several researches [101, 105-110]. Following the classical nucleation theory, the nuclei form as a result of localized compositional fluctuations that occur statistically within the supersaturated matrix [108, 111]. For homogeneous nucleation, the nucleation rate is expressed as:

$$\dot{N}_p = \frac{R_g Z \beta \exp(-(\Delta G / k_b T))}{V_m} \tag{4.1}$$

where $N_p$ is the precipitates density, $R_g$ is the gas constant, $V_m$ is the molar volume of precipitates, $T$ is the ageing temperature, $\Delta G$ is the critical activation energy for precipitation, $k_b$ is the Boltzmann constant, $Z$ is the Zeldovich's factor, $\beta$ is the parameter for precipitates growth. The volume fraction of precipitates could be calculated as below:

$$f_v = V_0 N_p \tag{4.2}$$

where $V_0$ is the average volume of the precipitates.

Previous models have also characterized the thermodynamics and kinetics (nucleation, growth and coarsening of the precipitates) for precipitation processes. For example, Hou et al. [112] developed a thermodynamically-based precipitation model, employing the classical nucleation and growth theories. This was adapted to deal with the precipitation kinetics of aged Al-Cu-Mg-Ag alloys. The model gives an estimation of the precipitation kinetics (evolution of radius and density of precipitates for both $\alpha$ and $\theta$ phases) of the alloy. Liu et al. [101, 105] made an attempt to describe the precipitates evolution and yield strength as a function of process parameter for aluminium alloy with disc-shaped or rod-shaped precipitates. In his model, the homogeneous growth of disc-shaped precipitates, the radius of the disc plane ($r$) and the half-length of the peripheral plane ($l$) will be varied with the ageing time ($T$).

$$l = \frac{2}{3}\sqrt{A^2 \beta D T} \tag{4.3}$$

$$r = \frac{2}{3}\sqrt{\beta D T} \tag{4.4}$$

The volume fraction ( $f_v$ ) of disc-shape precipitates can be expressed as:

$$f_v = \frac{2\pi}{A} r^3 L N_0 Z \beta^* \exp(\frac{-\Delta G^*}{kT_C})T \tag{4.5}$$

where $A$ is the aspect ratio of disc shaped precipitate ( $r/l$ ), $\beta$ is a dimensionless growth parameter which is in proportion to the super-saturation $\Omega = (C_0 - C_e)/(C_P - C_e)$ and can be calibrated by the formula of $\beta = \Omega / p_A A$ with $p_A$ being a factor. $L$ is the Avogadro number, $N_0$ is the number of mole by unit volume, $Z$ is the Zeldovich's factor, $T$ is the ageing temperature, $\Delta G^*$ is the critical activation energy for precipitation, the parameter of $\beta^*$ can be expressed as $\beta^* = 4\pi (r^*)^2 D C_0 / a_l^4$ with $D$ being the diffusion coefficient of solute atom in solvent, $a_l$ being the lattice parameter and $r^* = 2\gamma / \Delta F_V$ is the critical radius of the precipitates. In the formula of $r^*, \gamma$ is the precipitates-matrix interfacial energy and $F_V$ is the driving force per mole of solute atom to precipitate from super saturated solid solution:

$$F_V = R_g T / \upsilon_{at} [C_p ln(C_0 / C_e) + (1 - C_p) ln(1 - C_0)/(1 - C_e))] \tag{4.6}$$

where $\upsilon_{at}$ is the molar volume of precipitates and $C_0$ , $C_e$ and $C_p$ are the mean solute concentrations by atom percentage in matrix, equilibrium precipitate-matrix interface and precipitates, respectively.

It is assumed here that the growth stage of the precipitates is terminated once the excess solute atoms are exhausted totally. At the moment, defining $T = T_m$ and $r = r_m$ then the maximum volume fraction of precipitates is obtained:

$$f_{mv} = \frac{2\pi}{A} r_m^3 L N_0 Z \beta^* \exp(\frac{-\Delta G^*}{kT_C}) t_m = \frac{C_0 - C_e}{C_P} \tag{4.7}$$

Some relevant researches on simplifying the characterization of ageing disc-based precipitates aluminium alloy have been taken. For example, Zhang et al. [110] modelled the creep age forming of heat-treatable strengthening aluminium alloy containing disc shaped precipitate. In terms of describing the precipitates fraction, a more general parameter, normalized volume fraction is used here:

$$\bar{f}_v = \frac{f_v}{f_v^*} \tag{4.8}$$

where $f_v$ is the current volume fraction of precipitates and $f_v^*$ is the maximum volume fraction. The volume fraction of disc shaped precipitates in ageing process is uniformly expressed as:

$$\dot{\bar{f}}_v = \frac{E_1 l_n^{w_1} \dot{l}_n}{A^{w_2}} (1 - \bar{f}_v)^{v_1} \tag{4.9}$$

where $\dot{\bar{f}}_v$ is the growth rate of the normalized volume fraction, A is the aspect ratio ($r/l$). $E_1$ , $w_1$ , $w_2$ , $v_1$ are material constants, $\dot{l}_n$ is the growth rate of the characteristic size of precipitate and is expressed as:

$$\dot{l}_n = E_2 (Q_1 - l_n)^{v_2} \exp(\frac{-Q_2}{R_g T}) \tag{4.10}$$

where $Q_1, E_2, v_2$ are material constants, $Q_2$ is the activation energy related to the growth of precipitates.

### 4.2.6 Mechanisms of age hardening

The ageing process enhances the yield strength of a heat treatable alloy. Figure 4.3 shows a schematic diagram of relative contribution to the yield strength of an aluminium alloy 2219 and corresponding microstructure evolution. At initial stage, the quenching process retains the solute atoms within the aluminium matrix to obtain supersaturated solid solution (SSSS) within the aluminium matrix as there has been insufficient time for the precipitates to nucleate in the quenched aluminium alloy. The initial yield stress would reflect the contributions of the intrinsic stress and solute hardening. At the early stage of ageing, ordered and solute rich clusters, namely GP zones, form. The yield strength of material starts to increase as the precipitates starts to nucleate and coarsen. As the coarsening process proceeds, the amount of solute atoms in the matrix decreases. This matrix results in a decrease in the solute hardening. However, the decrease in solute hardening is more than offset by the increase owing to dispersion hardening. Therefore, the overall strength of the material continues to increase with time as precipitates continue to grow. Eventually the GP zones are replaced by the $\theta''$ phase, further replaced by the $\theta'$ phase, and finally the stable $\theta$ phase. There is no further decrease in strength owing to the decrease in the amount of solute elements in the matrix, as it has reached its equilibrium value. Precipitation hardening will reach a peak value at this stage as further nucleation and coarsening of precipitates would reduce the pinning effect of the precipitates.

As the precipitates become large, the coherent precipitate will lose their coherency and the dislocation-precipitate will be diminished. In addition, the decreasing number of precipitates and increasing inter particle distance cause a decrease in the precipitates hardening and an overall decrease in the strength of the material. Thus, the strength of the material will reach a maximum value and begin to decrease. As coarsening continues, the

material's strength will continue to decrease [98, 113, 114]. Another mechanism contributing to hardening is dislocation, which is generated due to creep deformation. At the ageing temperature, annealing takes place, which reduces the dislocation density. Thus the dislocation density reaches a saturated condition at the end of primary creep. This indicates that dislocation hardening increases quickly at the initial stage of CAF. Dislocations provide the nucleation sites for precipitates which accelerate the precipitate nucleation and growth. At high stress levels creep is higher, thus dislocation density is higher, which leads to a shorter ageing time. The interaction between age hardening and dislocation motion hardening is significant [62].

## 4.3 Development of unified creep ageing constitutive equations

### 4.3.1 Unified uniaxial creep-ageing constitutive equations

Zhan et al. [62] proposed a set of constitutive equations to model the creep ageing hardening behavior of AA7055. The equations were formulated based on the earlier work by Ho etc. [54, 55], which is based on the assumptions that the precipitates are in the form of spherical shape for 7XXX aluminium alloys. This is the material phenomenon based constitutive equations and has been successfully used to model the creep ageing hardening behaviour of 7XXX aluminium alloys. The creep ageing constitutive equations presented in [62] are adopted here to model the creep ageing behaviour, stress relaxation and dynamic ageing hardening for AA2219, where the precipitates are in the form of disc shape. For the convenience of discussion, the equations are summarised here first.

$$\dot{\varepsilon}_c = A_1 \sinh\{B_1[|\sigma|(1-\bar{\rho}) - k_0\sigma_y]\} sign\{\sigma\} \tag{4.11}$$

$$\dot{\sigma}_A = C_A \dot{\bar{A}}^{m_1}(1-\bar{A}) \tag{4.12}$$

$$\dot{\sigma}_{ss} = C_{ss} \dot{\bar{A}}^{m_2}(\bar{A}-1) \tag{4.13}$$

$$\dot{\sigma}_{dis} = A_2 \cdot n \cdot \bar{\rho}^{n-1}\dot{\bar{\rho}} \tag{4.14}$$

$$\sigma_Y = \sigma_{ss} + \sqrt{\sigma_A{}^2 + \sigma_{dis}{}^2} \tag{4.15}$$

$$\dot{\bar{A}} = C_r(Q-\bar{A})^{m_3}(1+\gamma_0\bar{\rho}^{m_4}) \tag{4.16}$$

$$\dot{\bar{\rho}} = A_3(1-\bar{\rho})\left|\dot{\varepsilon}_c\right| - C_p\bar{\rho}^{m_5} \tag{4.17}$$

where $A_1$, $B_1$, $k_0$, $C_A$, $m_1$, $C_{SS}$, $m_2$, $A_2$, $n$, $C_r$, $Q$, $m_3$, $\gamma_0$, $m_4$, $A_3$, $C_p$, $m_5$ are material constants.

Equation (4.11) describes the evolution of creep strain. Creep rate is not only a function of stress, $\sigma$, and dislocation density, $\bar{\rho}$, but also a function of ageing (precipitation) hardening, $\sigma_A$, the solute hardening, $\sigma_{SS}$, and dislocation hardening, $\sigma_{dis}$, which altogether contribute to the material's yield strength $\sigma_Y$, which varies during a CAF process.

In the present model, the yield strength, $\sigma_Y$, derives from three mechanisms, $\sigma_{dis}$, $\sigma_A$ and $\sigma_{SS}$. In terms of expression the evolution of precipitates size, two problems arise: first, the initial precipitate volume and shape are difficult to determine which vary in different aluminium alloys. Secondly, according to classic ageing mechanisms, in addition to precipitate size, the inter-particle distance is another important factor to influence precipitate hardening behaviour and this should also be considered in the hardening equations. Thus a more general parameter, normalized mean ratio of disc-shape precipitates, is introduced here:

$$\bar{A} = \frac{A}{A_C} \tag{4.18}$$

where $A$ means the mean ratio of radius to half length for the disc-shape precipitates in 2XXX series aluminium alloy [72, 101]. $A_C$ is the mean ratio at peak ageing state, which considers the best match of precipitate size and spacing for the alloy. When $0 \le \bar{A} < 1$, the alloy is in the under-ageing state; $\bar{A} = 1$, represents peak-ageing and $\bar{A} > 1$ denotes over-ageing. This approach simplifies the modelling process significantly. The evolution of the normalized mean ratio of precipitates is given in equation (4.16).

The term $(1-\bar{\rho})$ in Equation (4.11) is used to model the primary creep, which is the contribution of dislocation density to creep rate. This is the same as strain hardening effect on creep. But the dislocation density variation is related to dynamic and static recovery, in addition to creep deformation. A detailed description of the normalised dislocation density will be given later.

Equations (4.12) and (4.13) represent the evolution of age hardening and solute hardening, which are described in terms of normalized mean ratio of disc-shape precipitates, $\bar{A}$ and its evolutional rate $\dot{\bar{A}}$ (equation (4.16)). The strengthening contribution from the precipitates can arise from a variety of mechanisms, such as chemical hardening, coherency strain hardening, etc. However, the overall strengthening contribution from various mechanisms is summarized in Equation (4.12), where $C_{\mathrm{A}}$ describes the interaction between dislocations and shearable precipitates. Equation (4.13) shows the contribution from solid solution strengthening (solute hardening), where resistance is caused by solute atoms to obstruct dislocation motion. Refer to Equation (4.13), $C_{\mathrm{SS}}$ is a constant related to the size, modulus and electronic mismatch of the solute; $m_2$ describes the depletion of solute elements into precipitate. As the concentration of the solute atoms decreases, the solid solution strengthening decreases, acting as a 'softening' mechanism. Equation (4.14) describes the

evolution of dislocation hardening, which is a function of normalized dislocation density $\overline{\rho}$, which is defined by [115]:

$$\overline{\rho} = \frac{\rho - \rho_i}{\rho_m} \tag{4.19}$$

where $\rho_i$ is the dislocation density for the virgin material (the initial state), and $\rho_m$ , the maximum (saturated) dislocation density that the material could have. Thus the actual dislocation density $\rho$ ranges from $\rho_i$ to $\rho_m$. This results in that the variation of normalized dislocation density, $\overline{\rho}$, ranges from 0 (the initial state) to 1 (the saturated state) in the condition that $\rho_i << \rho_m$. The evolution of the normalized dislocation density is given in equation (4.17). The first term in Equation (4.17) represents the development of dislocation due to creep deformation and the dynamic recovery. The second term gives the effect of static recovery in the dislocation density at elevated temperature [115].

Combining Equations (4.12), (4.13) and (4.14), gives Equation (4.15), the individual contribution of each hardening mechanism on the overall yield strength for the material during ageing process. The key feature of Equation (4.15) is that the yield stress, $\sigma_Y$, changes dynamically during the creep ageing period due to age and dislocation hardening. This feature could not be modelled using the conventional visco-plastic constitutive equations [116].

Equation (4.16) describes the evolution of the mean ratio of disc-shape precipitates during the isothermal ageing condition. As precipitates evolve or grow monotonically during isothermal ageing, the coarsening kinetics of the ageing mechanism can be modelled using a normalized mean ratio of disc-shape precipitates growth equation (4.16), in which the

nucleation and growth of precipitates are related to the dislocation density described in Equation (4.17). Since CAF is a combination of creep deformation and age-hardening, Equation (4.16) includes the dislocation density effect to describe the dynamic ageing behaviour. That is as the normalized dislocation density (or creep deformation) increases, the age-hardening effect increases. The effect of the dislocation density (or creep deformation) on precipitate nucleation and growth is controlled by the parameters $\gamma_0$ and $m_4$ in the equation. For stress-free aging conditions, the normalized dislocation density is zero, thus Equation (4.16) models only the static ageing behaviour. The form of Equation (4.16) was chosen due to its several advantages. First, normalized mean ratio $\overline{A}$ is used to substitute conventional mean ratio of radius to half length $A$, which can give a synthetic consideration of the effect of both precipitate size/shape evolution and inter-particle distance if an optimal precipitate size, referring to peak ageing strength of different aluminium alloys can be provided. Second, to avoid numerical difficulties, normalized precipitate mean ratio, is placed as a numerator instead of a denominator. Third, the term, $Q$, a material constant for a given alloy, is used to represent the saturation limit for depletion of copper solute atoms within the aluminium matrix. In a practical ageing mechanism, when the depletion of copper solute atoms eventually reaches its saturation value, precipitation will stop; hence the precipitate will stop growing. Fourth, the power term, $m_3$, gives flexibility to the equation as different alloys behave differently. Most importantly, Equation (4.16) is capable of describing both static and dynamic ageing behaviour while conventional precipitate growth equations can model only static ageing behaviour.

### 4.3.2 Model calibration from experimental data

The material constants in proposed creep aging constitutive equations were determined by fitting experimental data of both creep ageing curves and yield strength variations at different stress levels using evolutionary algorithms (EA) based on optimisation methods [116-119]. To simplify the determination process and speed up convergence, the whole process was divided into three stages below and an evolutionary-algorithm-based fitting software has been developed to help obtain the material constants efficiently (The software is developed by Dr. Pan Zhang from Imperial College London).

Step 1: Determination of material constants related to normalised precipitate size using experiment results of yield strength evolution with time under stress-free condition (0 MPa), as shown in Figure 4.4.

Step 2: Determination of material constants related to yield stress using experimental results of yield strength evolution with time under different stress level, as shown in Figure 4.4.

Step 3: Re-evaluate all pre-determined material parameters according to the experimental creep data and yield strength data, optimise the pre-determined material parameters in Step 1-2 to obtain the best-fit results, as shown in Figures 4.4 and 4.5.

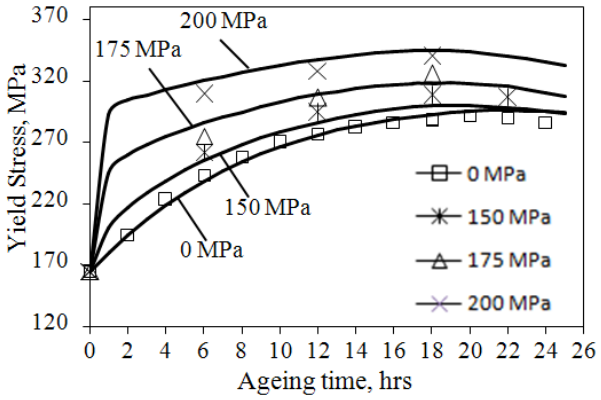


Figure 4.4: Comparison of experimental (symbols) and computed (solid curves) yield strength variation at different stress levels.

(a)

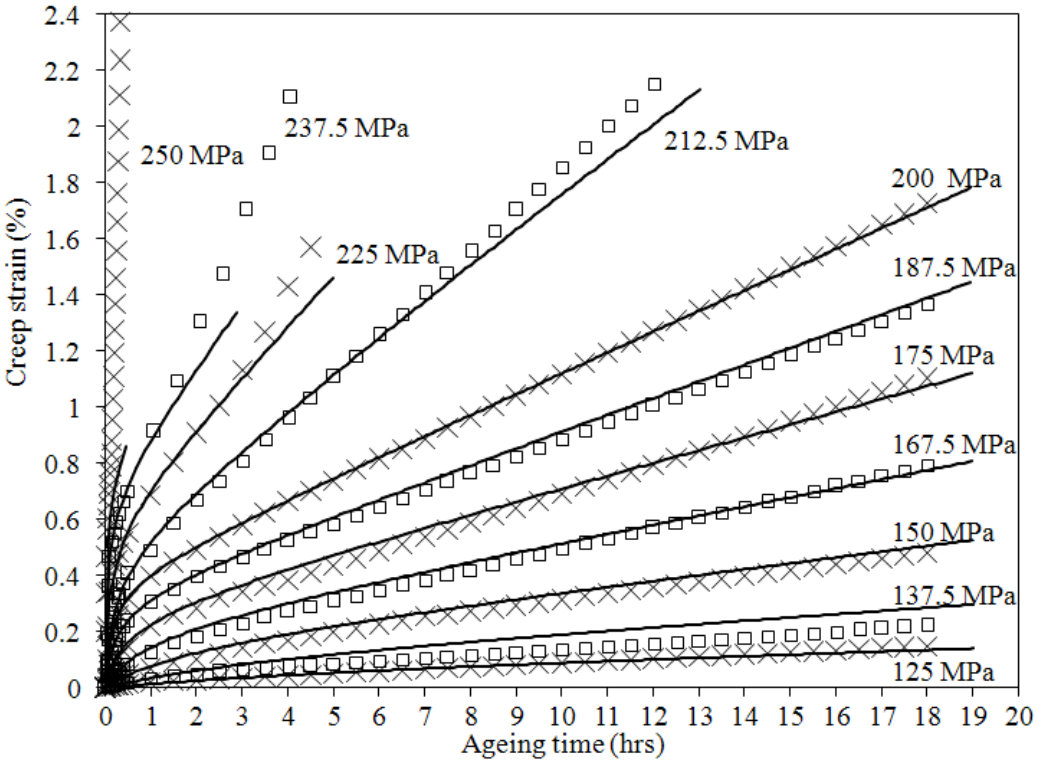


(b)

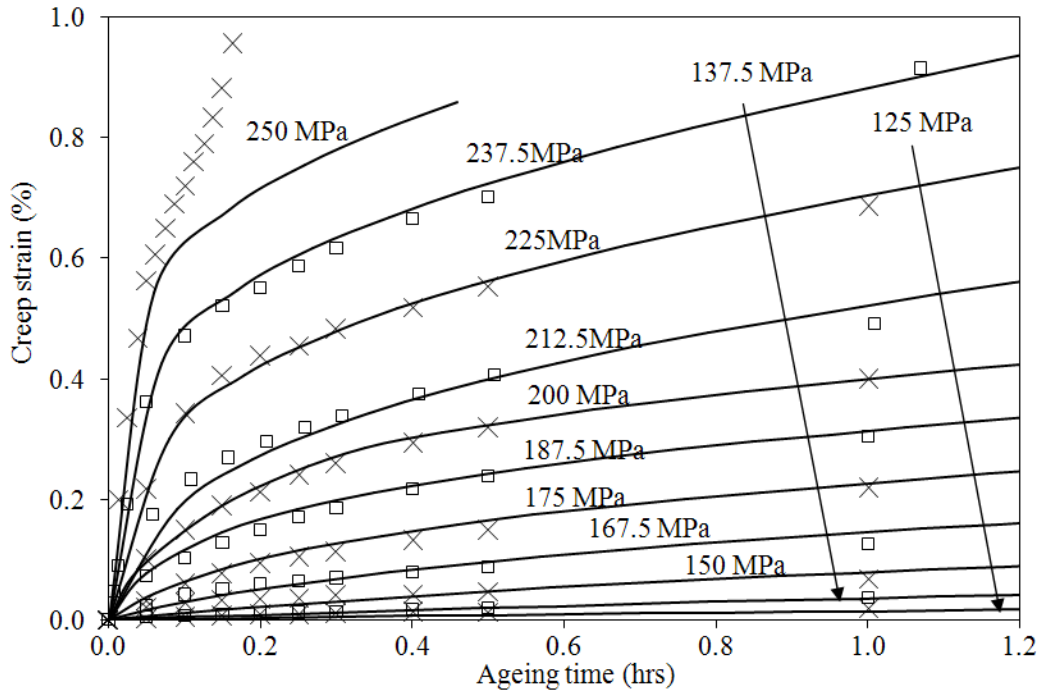


Figure 4.5: Comparison of experimental (symbols) and computed (solid curves) creep ageing curves for a range of stress levels for (a) a full creep ageing test duration (b) up to 1.2 hour duration.

By performing the above-mentioned steps, the material constants in the unified constitutive equations were determined and listed in Table 4.1 when the stress level is below 210 MPa and Table 4.2 when the stress level is above 200 MPa (Stresses level between 200 MPa and 210 MPa can use either Table 4.1 or Table 4.2). It is noted that these equations can only model the primary and secondary creep and it is not suitable to model the tertiary creep. When the stress is 225 MPa, tertiary stage occurred obviously at $T_A = 3.5$ hours, the unified constitutive equations failed to model the tertiary creep strain behaviour after $T_A = 3.5$ hours. The equations are only suitable to model the primary and secondary creep strain behaviour due to the usage of sinh law. In CAF, creep is a favoured process to form the parts, tertiary creep is not expected, because it results in damage and failure of the materials. Also, the determined two sets of material constants are not unique values and both sets are used to be implemented into the constitutive equations with the aim of getting the best fitting between the computed and experimental data. It is too difficult to use one set of parameters to capture all the curves, because when the initial stress is above 212.5 MPa, the primary creep rate increased significantly, tertiary stage creep takes place and it shortens the secondary creep. The creep strain behaviour changed significantly after 212.5 MPa.

Table 4.1: Constants in the CAF constitutive equations for AA2219 under a stress level of 212.5 MPa at 175 °C.

| $A_1$ ($h^{-1}$) | $B_1$ (MPa) | $k_0$ | $C_A$ (MPa) | $m_1$ | $C_{ss}$ (MPa) | $m_2$ | $n$ | $A_2$ |
|---|---|---|---|---|---|---|---|---|
| 3.0E-8 | 0.0825 | 0.078 | 50.1 | 0.42 | 15.0 | 0.85 | 0.9 | 520 |
| $C_r$ ($h^{-1}$) | $Q$ | $\gamma_0$ | $m_3$ | $m_4$ | $A_3$ | $C_p$ | $m_5$ | |
| 0.032 | 1.76 | 2.7 | 1.6 | 2.1 | 65 | 0.182 | 1.01 | |

Table 4.2: Constants in the CAF constitutive equations for AA2219 above a stress level of 200 MPa at 175 °C.

| $A_1$ ($h^{-1}$) | $B_1$ (MPa) | $k_0$ | $C_A$ (MPa) | $m_1$ | $C_{ss}$ (MPa) | $m_2$ | $n$ | $A_2$ |
|---|---|---|---|---|---|---|---|---|
| 1.6E-10 | 0.101 | 0.08 | 50.1 | 0.42 | 15.0 | 0.85 | 0.9 | 520 |
| $C_r$ ($h^{-1}$) | $Q$ | $\gamma_0$ | $m_3$ | $m_4$ | $A_3$ | $C_p$ | $m_5$ | |
| 0.032 | 1.76 | 2.7 | 1.6 | 2.1 | 35 | 0.318 | 1.01 | |

### 4.3.3 Modelling results and discussions

Having determined all material constants, the proposed set of constitutive equations has been tested for its capability to predict the creep-age response for AA2219 at 175 ℃ for a number of different stress levels with ageing duration of 18 hours. Figure 4.5 shows a comparison of the predicted and experimental creep stains for different stress levels. It can be observed that very close agreement is achieved. The accumulated error is less than 1.68%. However, the model is insufficient to model the tertiary stage of creep due to the nature of sinh-law (when applied stress is greater than 212.5 MPa). Good acceptable agreement between experimental and computed data has been obtained at primary and secondary stage of creep and CAF is a process which are the only two stages expected to occur during CAF.

The symbols and solid curves in Figure 4.4 show the measured and modelled yield stress evolution for different stress level conditions after interrupt creep test ($\sigma = 0$, 150, 175, 200 MPa). It should be noted that at $T = 0$ hour, all four curves have the same yield stress value of 165 MPa. Close agreement between experimental and modelled results shows that the developed constitutive equations are capable of modelling the creep-ageing behaviour of AA2219 at 175 °C for the duration of 18 hours.

A more detailed prediction of AA2219 hardening mechanism is presented in Figure 4.6 at stress-ageing ($\sigma = 150$ MPa) and free ageing conditions ($\sigma = 0$ MPa). It can be seen that the dislocation hardening, $\sigma_{dis}$, which is zero at stress free ageing conditions, however, for stress ageing conditions, it increases quickly at the beginning and then reaches its peak value in about 1.5 hrs at 50 MPa, then it decreases slowly due to the combined effects of dislocation generation during creep deformation and annihilation effects of dynamic recovery static recovery at high temperature. $\sigma_{ss}$, decreases quickly from the very beginning to $T = 8$ hours, and then remains a slowly decreasing trend until reaching its saturation point for both conditions. $\sigma_A$, for stress free conditions, increases monotonically with time until it reaches the peak ageing time $T = 22$ hours, while for stress ageing condition, $\sigma_A$ arrives its peak value at around 20 hour and then decrease due to the formation of large incoherent particles and lead to an over-ageing status. For creep ageing under stress free conditions, the material's yield strength, $\sigma_Y$, reaches a value of 292 MPa at its peak ageing time ($T = 22$ hours); for stress level $\sigma = 150$ MPa, $\sigma_Y$ is 308 MPa at $T = 18$ hours near its peak ageing time ($T = 18.5$ hours). For all cases, the yield strength of the material has increased by approximate 80% during ageing.

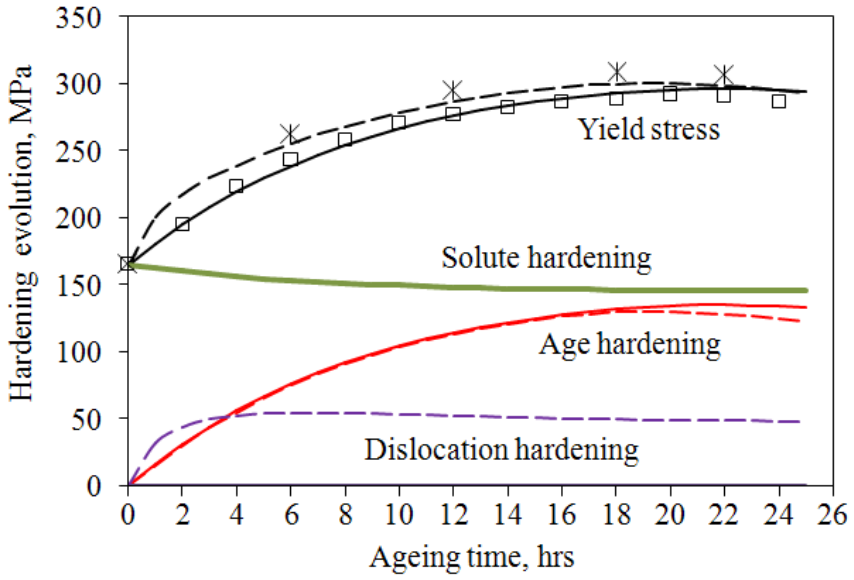


Figure 4.6: Predicted creep age hardening behaviour at σ = 0 MPa (solid curves) and σ = 150 MPa (dashed curves). The experimental data are shown as symbols.

To validate the effectiveness of the developed material model in the FE code, the stress relaxation behaviour has been predicted using the determined constitutive equations by performing creep deformation in a single element using ABAQUS. The predicted curves are compared with the experimental data in Figure 4.7(a) and (b). Overall, it can be observed that close agreement is achieved between predicted and experimental data with a maximum error of 11.76%. Referring to Figure 4.7 (b), for a time more than 1 hour, the predicted stress level is slightly lower than that of experimental data. This might be due to the constitutive model being less sensitive to the stress level lower than 137.5 MPa and therefore the time-dependent creep effect is not significant. From the results, the stresses relaxed significantly for time greater than 1 hour. At this stage, all the stresses are relaxed to a similar level.

(a)

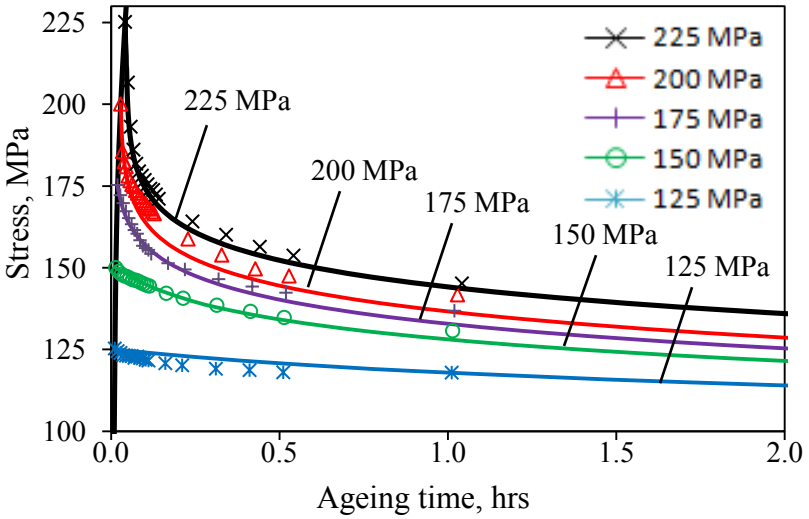


(b)

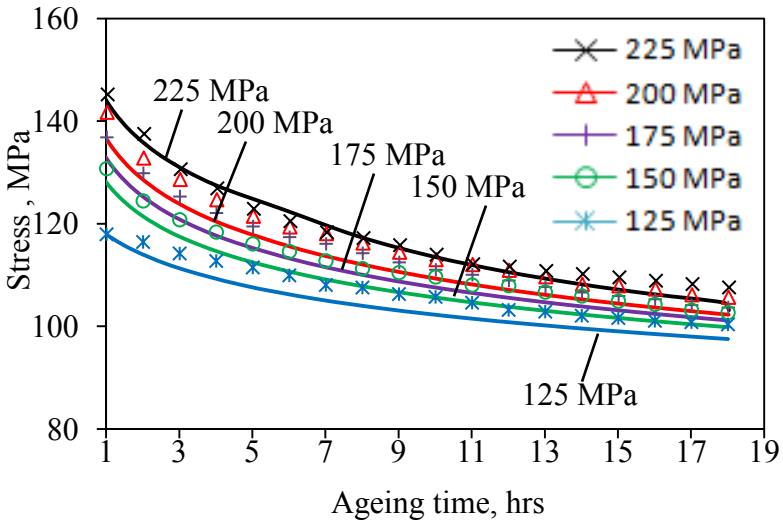


Figure 4.7: Comparison of experimental (symbols) and predicted (solid curves) stress relaxation for (a) up to 2 hours duration; (b) 1 to 18 hours duration for five initial stresses of 225 MPa, 200 MPa, 175 MPa, 150 MPa and 125 MPa.

## 4.4 Multi-Steps Springback Simulation Procedure

### 4.4.1 Details of the FE model

A finite element model has been developed to represent the cylindrical die and work piece under uniform loading condition in ABAQUS, as schematically illustrated in Figure 4.8. The CAF simulation consisted of holding a 6 mm thick, initially flat rectilinear rectangular

shaped workpiece (dimension: 200 × 50 × 6 mm) of aluminium alloy AA2219 against the die surface, and subsequently creep age-forming it at a constant temperature of 175 °C for 18 hours. The die surface has a radius of 150 mm and was modelled as a rigid body. Four node reduced integration shell elements were employed to model the workpiece. A friction coefficient of 0.1, which is related to the contact pair, was assigned at the tool/workpiece interface to simulate the non-lubricated contact between the workpiece and the die. For the convenience of locating the workpiece on the tool surface and avoiding potential problems in convergence in the implicit forming simulation, four ground springs with stiffness of $1\times10^{-6}$ N mm$^{-1}$, which can be compressed to zero volume, were used to support the weight of the workpiece at its corners, as shown in Figure 4.8. The die was meshed by using discrete rigid model. This is the due to the contact pressure can only be predicted on discrete rigid model rather than analytical rigid model in ABAQUS. Mesh convergence studies have been performed for the simulations with different size of mesh e.g. 15 mm, 10 mm, 5 mm and 4 mm. Good agreements have been obtained by using the mesh size of 5 mm and 4 mm. In this simulation, a mesh size of 4 mm is applied. Mesh convergence studies have been performed on all the simulations in this thesis in order to guarantee that enough elements are used to get a convergent solution. A detailed convergence study is shown in the Appendix to investigate the effect of implementation different mesh size.

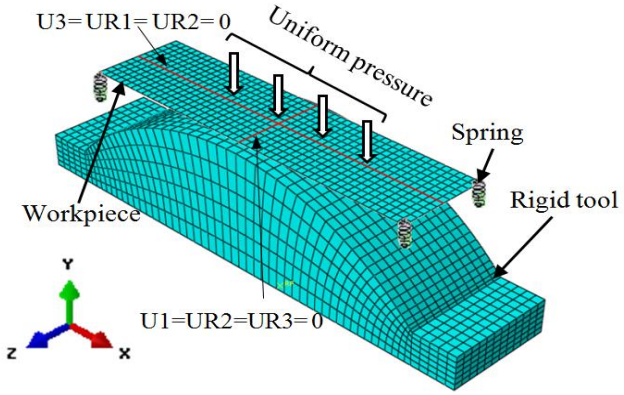


Figure 4.8: FE model with boundary and loading conditions.

### 4.4.2 Multi-axial constitutive equations

In a manner similar to that for creep deformation [120], the uniaxial sinh-law equations can be generalized by the consideration of a dissipation potential function. First consider the creep strain rate equation (4.11) without the hardening and other state variables which then reduces to

$$\dot{\varepsilon}_c = A_1 \sinh(B_1\sigma) \tag{4.20}$$

Equation (4.20) can be generalized for multi-axial conditions by assuming an energy dissipation potential of the form

$$\psi = \frac{A_1}{B_1}\cosh(B_1\sigma_e) \tag{4.21}$$

where $\sigma_e = \left(3S_{ij}\cdot S_{ij}/2\right)^{1/2}$ is effective stress and $S_{ij} = \sigma_{ij} - \delta_{ij}\sigma_{kk}/3$ are stress deviators. Assuming normality and the associated flow rule, the multi-axial relationship is given by

$$\frac{d\varepsilon_{ij}^c}{dt} = \frac{\partial\psi}{\partial S_{ij}} = \frac{3A_1}{2}\left(\frac{S_{ij}}{\sigma_e}\right)\sinh\left(B_1\sigma_e\right) \tag{4.22}$$

On re-introduction of the hardening and grain growth variables the effective inelastic strain rate $\dot{p}$ for the sinh-law material model can be written as:

$$\dot{p} = A_1 \sinh\{B_1[\sigma_e(1-\bar{\rho}) - k_0\sigma_y]\} \tag{4.23}$$

Then the set of multi-axial viscoplastic constitutive equations, integrated within a large strain formulation, can be written as:

$$D_{ij}^c = (3S_{ij}/2\sigma_e)\dot{p} \tag{4.24}$$

$$\dot{\sigma}_A = C_A \dot{\bar{A}}^{m_1} (1 - \bar{A}) \tag{4.25}$$

$$\dot{\sigma}_{ss} = C_{ss} \dot{\bar{A}}^{m_2} (\bar{A} - 1) \tag{4.26}$$

$$\dot{\sigma}_{dis} = A_2 \cdot n \cdot \bar{\rho}^{n-1} \dot{\bar{\rho}} \tag{4.27}$$

$$\sigma_y = \sigma_{ss} + \sqrt{\sigma_A{}^2 + \sigma_{dis}{}^2} \tag{4.28}$$

$$\dot{\bar{A}} = C_r (Q - \bar{A})^{m_3} (1 + \gamma_0 \bar{\rho}^{m_4}) \tag{4.29}$$

$$\dot{\bar{\rho}} = A_3 (1 - \bar{\rho}) \dot{p} - C_p \bar{\rho}^{m_5} \tag{4.30}$$

$$\hat{\sigma}_{ij} = G D_{ij}^e + 2\lambda D_{kk}^e \tag{4.31}$$

where $D_{ij}^c$ is the rate of inelastic deformation; $D_{ij}^{\mathrm{e}} = D_{ij}^{\mathrm{T}} - D_{ij}^c$ is the rate of elastic deformation, $D_{ij}^{\mathrm{T}}$ is the rate of total deformation and $\hat{\sigma}_{ij}$ is the Jaumann rate of Cauchy stress. $G$ and $\lambda$ are the Lamé elasticity constants. The multi-axial constitutive equations have been implemented into the FE solver ABAQUS through a user defined subroutine and used to simulate creep age forming process.

### 4.4.3 CREEP subroutine

The multi-axial creep-ageing constitutive equations were implemented into the large deformation FE solver ABAQUS through the user-defined subroutine CREEP and used to simulate CAF. In addition to the original constitutive equations, the gradients, $\partial \Delta p / \partial p$ and $\partial \Delta p / \partial \sigma_e$ were determined accurately, so that the step time could be controlled efficiently through the implicit integration employed by ABAQUS [121].

### 4.4.4 FE simulation procedures

To simulate the uniform pressure condition, a three-step analysis was performed (Figure 4.9). Initially a 10 MPa load was applied incrementally in a static analysis, followed by a visco step where this load was held over a period of 18 hours, allowing ageing, creep and stress relaxation to take place. Finally, the uniform pressure was removed incrementally, enabling the aluminium workpiece to springback.

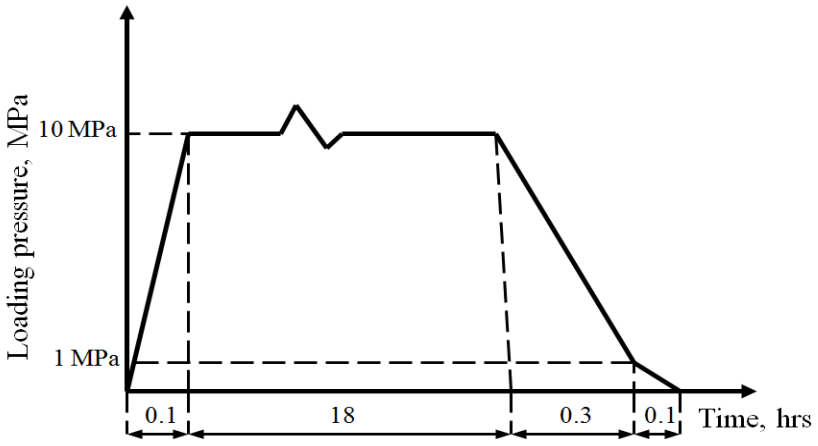


Figure 4.9: Loading process in numerical simulation.

## 4.5 Computational results and discussions

### 4.5.1 Prediction of springback

A contour plot of the equivalent (Mises) stress distribution, which controls the creep strain rate, over the workpiece's surface, is shown in Figure 4.10 for three stages of CAF. The total forming time is 18 hours. Figure 4.10 (a) shows the initial fully loaded condition where the ground springs were compressed to overcome their stiffness by the applied pressure and the whole workpiece deformed to build a full contact with the die surface. At this stage, a relatively uniform stress distribution (190 - 200 MPa) can be observed within the workpiece. The maximum stress (around 204 MPa) was observed at the centre part of workpiece; in this

stage, the stresses were higher than the yield stress of the material which is around 165 MPa. At the end of CAF (Figure 4.10 (b)), significant stress relaxation due to creep took place, generally reduced the equivalent stress by approximately 80% to a maximum of 115 MPa. After the removal of the applied load, springback occurred and a residual stress can be observed in the workpieces. As shown in Figure 4.10 (c), most of the residual stress was released to below 76 MPa. Comparison of stress in the three forming stages shows that the equivalent stresses are lower at the edges of the workpiece, but higher at the centre for all stages, this is due to the amount of uniform pressure which is insufficient to force the workpiece to fully contact with the die surface. The pattern of the stresses in Figure 4.10 (c) is due to the implementation of springback at the corner and mid of the workpiece.

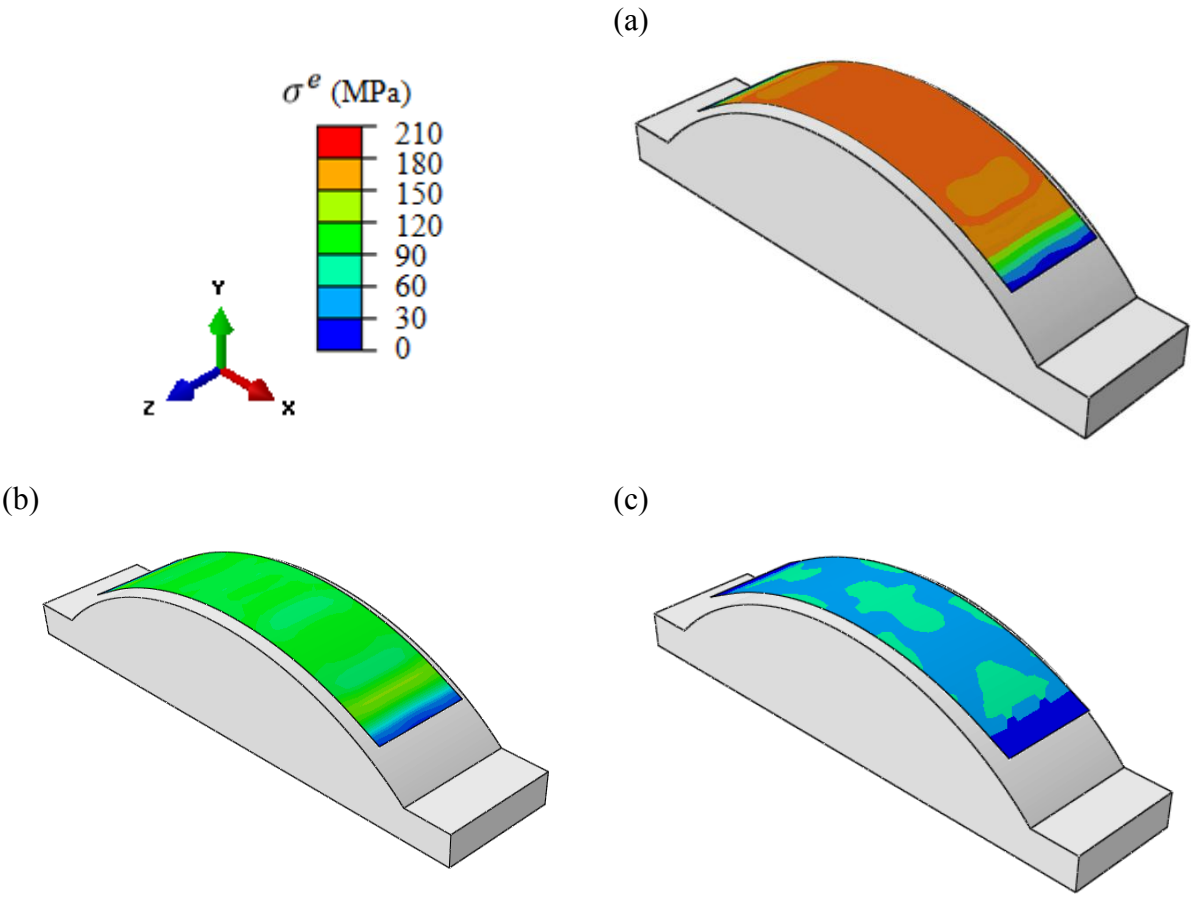


Figure 4.10: Equivalent Stress (MPa) distributions at different stages of CAF process, (a) deformed to target shape, (b) held for 18 hours, (c) after unloading.

### 4.5.2 Modelling of creep strain, evolution of precipitate ratio and yield strength

Figure 4.11 shows the distribution of creep strain on the top surface of AA2219 sheet during the creep ageing stage. After 1 hour of creep ageing, the maximum creep strain of the sheet is approximately 0.158% (Figure 4.11 (a)). The creep strain distribution was uniform except the edge area of the workpiece. After 9 hours of ageing, referring to Figure 4.11 (b), the creep strain increased further and high creep strain area slowly decreased. The majority of the creep strain was around 0.356% - 0.381% at the centre part. At the end of CAF, the major parts of the workpiece had a creep strain value around 0.416% (see Figure 4.11 (c)); the creep strain increment is not significant as the creep deformation has reached its steady state.

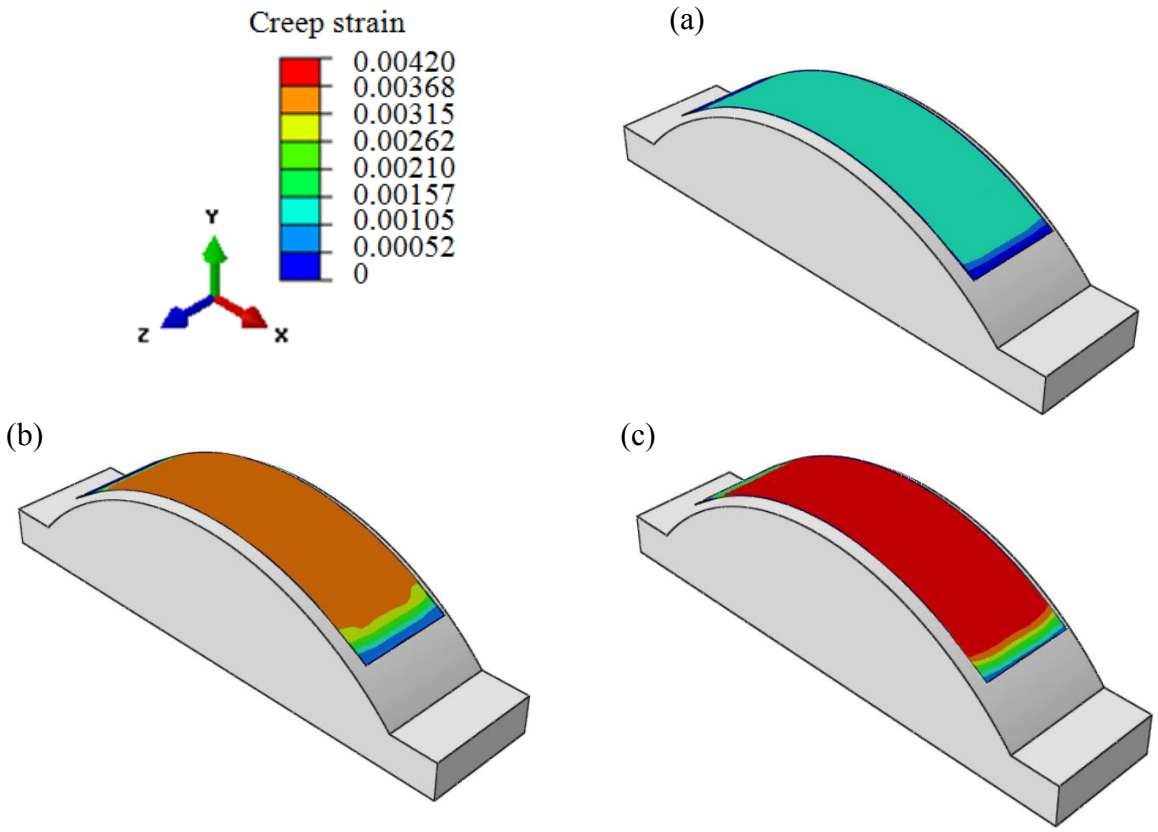


Figure 4.11: Distribution of creep strain during the ageing period at (a) 1, (b) 9 and (c) 18 hours.

Apart from modelling creep deformation, via constitutive equations implemented into ABAQUS, the normalized precipitate ratio and yield strength increment of the material during CAF can be predicted. Referring to Figure 4.12, at $T = 1$ hour, the normalized precipitates vary from 0.137 at low deformation area (edge area) to 0.323 at high deformation area (fully contact area). As ageing time increases from 1 hour to 18 hours, normalized precipitates ratio grow as creep deformation. At the end of ageing period, the maximum normalized precipitates ratio reach a value of 0.877 while the minimum value is about 0.366. It is observed that, at the low deformation area (edge area), the precipitates ratio are lower because in this region, the generation of precipitates only rely on the static ageing effect. In the meanwhile the increments of the precipitates ratio at high deformation are mainly due to the dynamic age effect (i.e. creep deformation on precipitate growth).

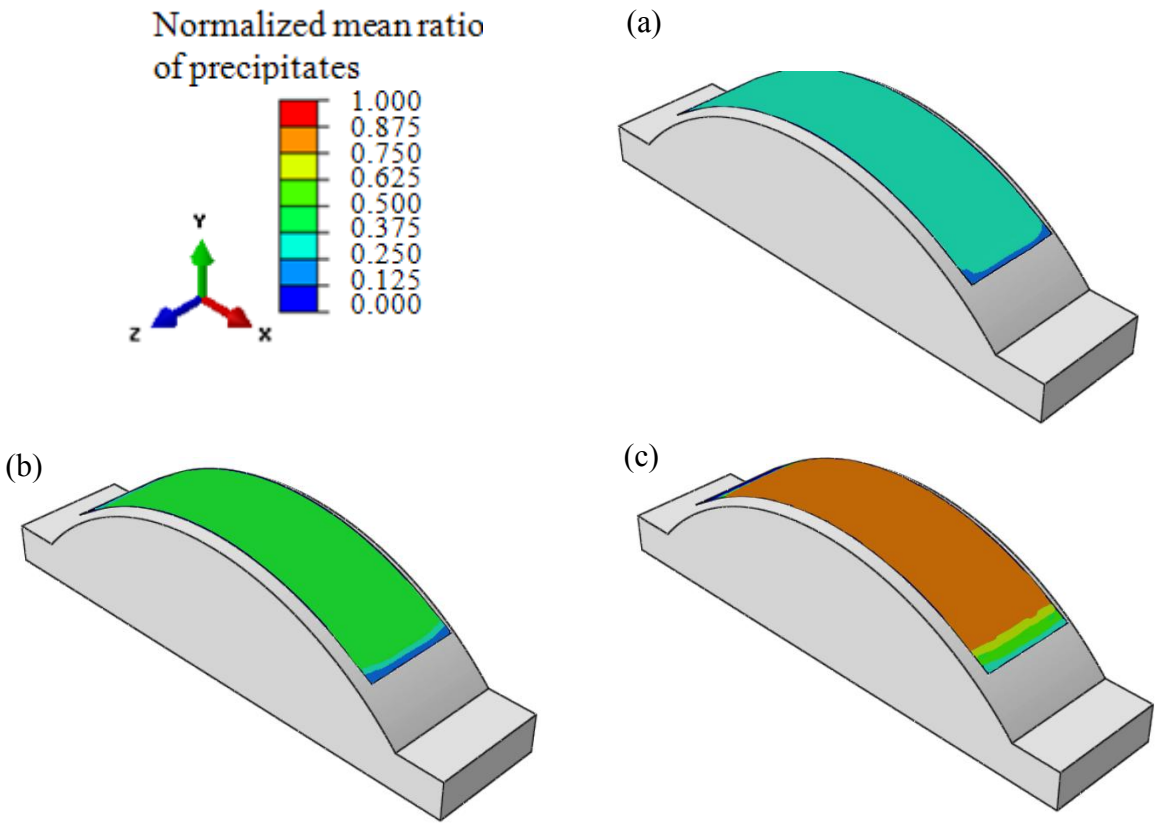


Figure 4.12: Distribution of normalized mean ratio of precipitates during the ageing period at (a) 1, (b) 9 and (c) 18 hours.

The evolution of the yield strength during CAF is shown in Figure 4.13. As the age hardening and solute hardening effects are the function of precipitates ratio, and dislocation hardening increases the yield strength mainly at primary stage, the yield strength distribution during CAF simulation are more or less similar to the normalized precipitates distribution. At the end of CAF ($T = 18$ hours), the yield strength increments are distributed evenly in the region where fully contact has achieved between workpiece and die with a value around 318 MPa.

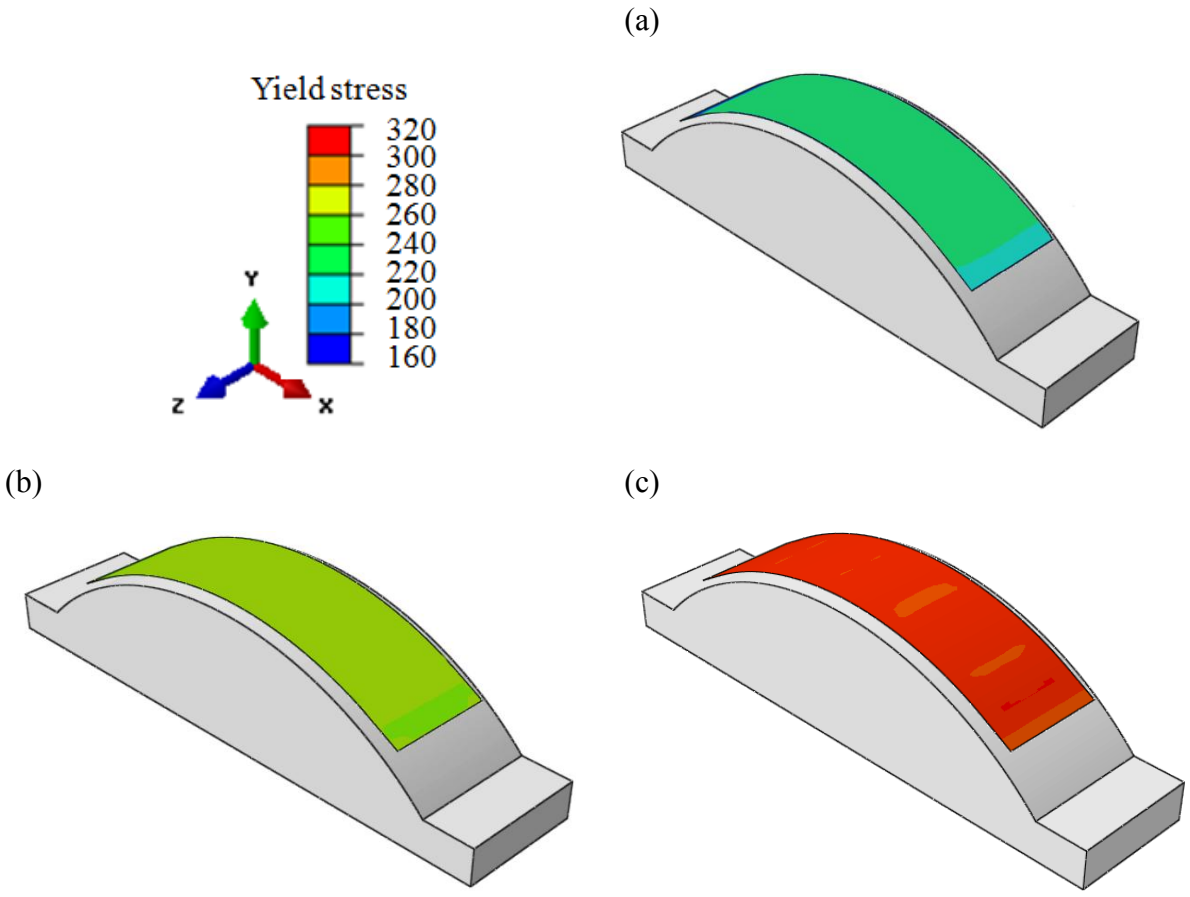


Figure 4.13: Distribution of yield stress variation during the ageing period at (a) 1, (b) 9 and (c) 18 hours.

## 4.6 Summary

Firstly, the age-hardening mechanism that occurs during artificial ageing of 2XXX series aluminium alloy is described. During the artificial ageing of the material, nucleation and growth of the precipitation takes place, which leads to the overall mechanical strength of the material increase. Based on both physical and mechanical properties of the material in CAF, a set of physically-based, unified constitutive equations has been adopted and calibrated from the experimental data, which enables to model the time-dependent creep deformation and the dynamic age-hardening behaviour as well as the prediction of stress relaxation behaviour at different stress levels during CAF.

Based on the establishment of the unified constitutive equations, FE simulation procedures to predict creep deformation, age-hardening and springback for CAF of a single curvature AA2219 sheet have been carried out. The material model is implemented into ABAQUS via the user-defined subroutine CREEP. The FE simulation results demonstrate that, the established FE model and procedure are capable to predict creep deformation, stress relaxation and the age-hardening properties evolution of the material during CAF.

# CHAPTER 5

# Four Point Bending Investigation on Creep Age Forming AA2219 Panel

## 5.1 Introduction

In this chapter, a four point bend rig was designed, manufactured and assembled. Bending tests were conducted on this rig to model the industrial creep age forming process. The aims of the test were twofold: one was to examine the relationship between the initial deflection and the amount of springback after ageing. The second was to validate the springback prediction from numerical simulation.

The experiment includes three stages like the industrial creep age forming routines, which are the loading stage, artificial ageing stage and unloading/springback stage. In the first (loading) stage, a self-made four point bending test rig was used to deflect the specimen into the required shape. In the artificial ageing stage, the deformed workpiece was held in place and the entire test rig was put into an Instron furnace at 175 ℃ for duration up to 18 hours. In the unloading/springback stage, the four point bending rig force is released and the workpiece is allowed to springback. To comprehensively understand the creep ageing effects on springback behaviour, corresponding stress-free forming experiments were conducted. The workpiece was deflected to the same shape similar to each CAF experiment. However, the force was removed after the workpiece deforming to the required position. Next, the deformed workpiece was stress-free heat treated for the same ageing period as the CAF experiment. These two kinds of workpiece formed by two series of experiments are

termed as creep age forming (CAF) workpiece and cold work bending stress free ageing (CWBSFA) workpiece.

For numerical validation, this chapter introduces the same integrated FE procedures in Chapter 4 to model the stress relaxation and springback on CAF workpiece. The numerical results are used to compare with the experimental data thereafter.

## 5.2 Equipments and Test Preparation

### 5.2.1 Bending test rig

Figure 5.1 shows the full configuration of the (i) experimental setup with (ii) an inset detailing the four point bend test rig. The red frame structure with four pillars were ordered from Danly UK, the four point bending dies were manufactured and assembled in the Mechanical Engineering Department workshop at Imperial College London. Detailed drawings are in Appendix A. All the main components are listed in Table 5.1. Figure 5.2 illustrates schematic of the four point bending test rig.

Table 5.1: Bending test rig components details

| Components | Description | Material | Dimension (mm) |
|---|---|---|---|
| A | Bottom frame | mild steel | L 400×W 150×D 40 |
| B | Pin | stainless steel | L 120 × Φ 16 |
| C | Top frame | mild steel | L 400×W 150×D 40 |
| D | Pillar | High strength steel | L 260 × Φ 32 |
| E | Top integral roller | stainless steel | Roller part L 60 × R 10 |
| F | Supporter | mild steel | N/A |
| G | Bottom Roller | stainless steel | L 60 × Φ 50 |
| H | Test workpiece | AA2219 | L 400×W 150×t 3/4.5/6 |
| I | Locking bolts | mild steel | L 220 × M12 |

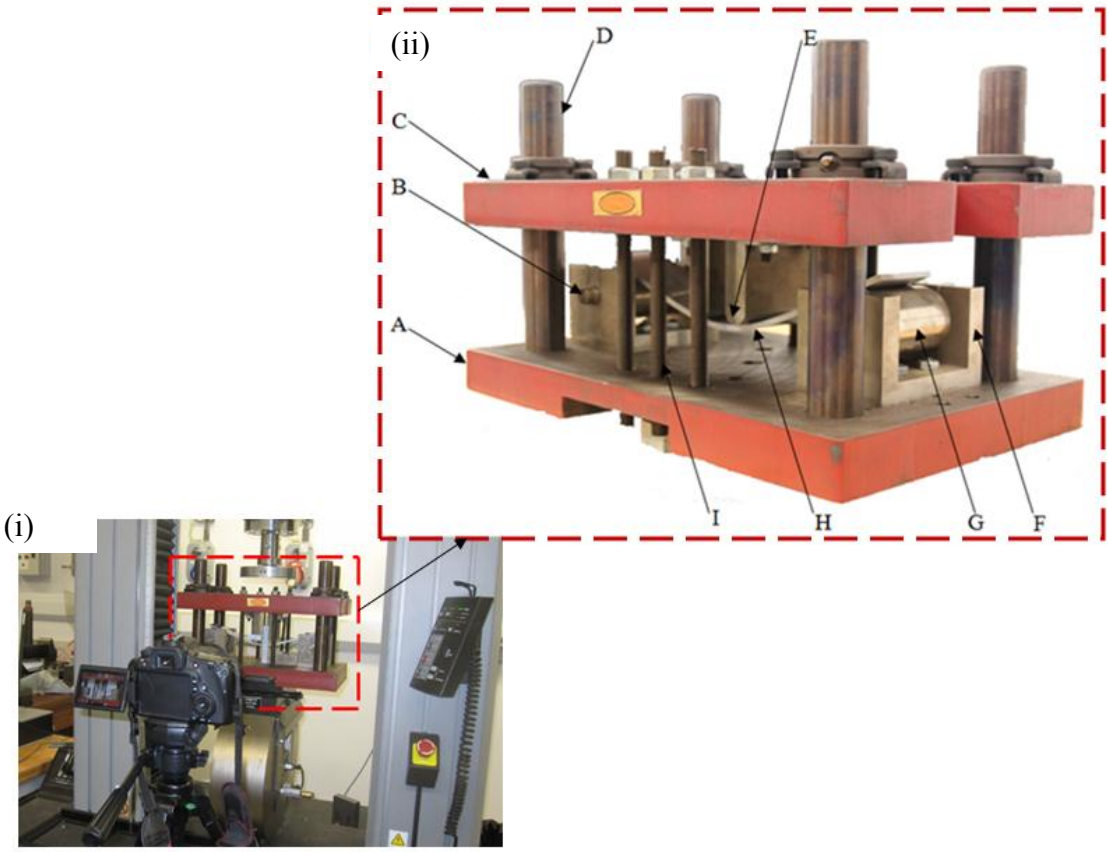


Figure 5.1: (i) Experimental setup with (ii) an inset detailing the four point bend test rig.

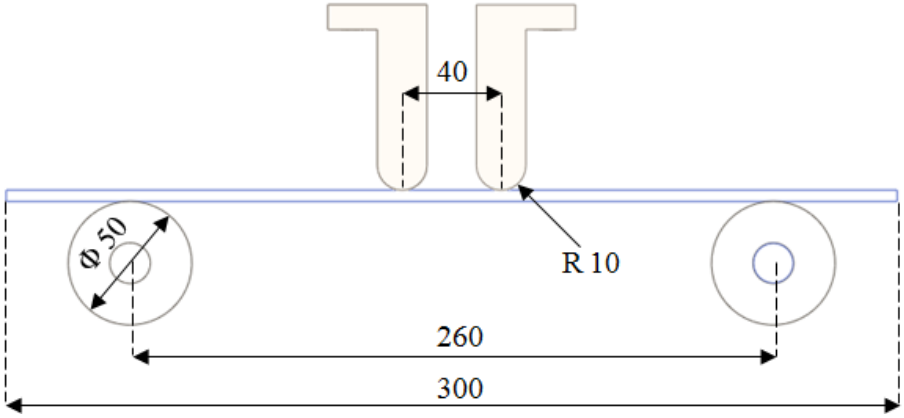


Figure 5.2: Schematic illustration of the four point bend test rig. (all dimensions in mm)

### 5.2.2 Loading device

An Instron 5588 material testing machine was used in the loading stage. A circular steel punch with a diameter of 120 mm was used to load the top frame of the bending rig. The

displacement control module was used in the experiments and the cross head speed and its final position can be controlled. A load cell, attached on the loading rig, was used to record the loading force response.

### 5.2.3 Heating device

To provide constant heating, a 900 KW fan furnace was used. The whole bending test rig which was holding the deformed CAF workpiece and CWBSFA workpiece were placed into the furnace for creep ageing. The temperature was maintained at 175 ℃ throughout the period. A K-type thermocouple was attached to the workpiece to monitor the temperature using a thermometer.

### 5.2.4 Test workpiece preparation

The test workpiece were cut into rectangular shape from the raw plate AA2219-O. The cutting process was performed at room temperature followed by solution heat-treatment and water quenching. Workpieces of three different thicknesses were used in the experiment. The dimension of each rectangular shaped plate was 400 ×150× 3.0 / 4.5/ 6.0 mm.

## 5.3 Experimental procedures

- The four point bending test rig was initially assembled on the Instron instrument load frames. The rig was aligned and centred.
- The initial flat specimen was centred and aligned properly on the top of the bottom roller. Some markings were used for alignment. A wooden block was used to avoid the contact between the top roller and the top surface of the workpiece. (Figure 5.3(a))

- The location of the bottom surface of the test workpiece was measured by a stainless steel ruler stand and the reading was captured by a DSLR cameral. The measurements were taken twice to check repeatability, and an average value was obtained. A bubble level device was used to ensure the plane of camera's sensor was parallel to the plane of the test.
- The wooden block was removed from the four point bending test rig set, the gravity of the top frame part and top integral roller forced the workpiece to deform. The total mass of the top part is 32.8 kg. (Figure 5.3(b))
- The displacement control module was used. Both cross head speed and displacement were preset. Meanwhile, five locking bolts were put through the holes in the top frame without locking.
- The punch was lowered until touching the top frames and preferably, a tiny positive load reading should display on the indicator for confirmation. (Figure 5.3(c))
- Before loading taking place, the load indicator and current movement were zeroed. The cross head was allowed to travel down at the constant speed to press down the top frames and consequently deflect the workpiece to the target displacement, i.e. 30 mm.
- Once the target distance was achieved, the cross head was stopped. The location of the bottom surface of the test workpiece was measured again to record the deformation. The measurement was taken up to five times and an average was calculated. (Figure 5.3(d))
- The stainless steel rule stand was removed out of the four point bend rig. Another locking bolt was put through the hole in the top frame.
- In order to get the CAF workpiece and hold the workpiece in place, six loading bolts were tightened until a zero load reading was displayed on the indicator channel. At this

stage, it is assumed the entire load was transmitted from the punch to the six locking bolts. (Figure 5.3(e-i))

- In order to get the CWBSFA workpiece, the top frame associated with the top integral roller was raised and the workpiece started to springback. The deformed workpiece was taken out from the four point bend test rig. (Figure 5.3(e-ii))
- The CWBSFA workpiece and the entire rig together with the held, deformed CAF workpiece were put into an Instron furnace. The whole rig was placed vertically to avoid any further load-induced creep taking place on the workpiece due to the mass of the top part. (Figure 5.3(f))
- A K-type thermocouple, connect to a thermometer, was attached to the surface of the workpiece to monitor the temperature.
- The furnace took up to 1 hour to increase from room temperature to 175 ℃. The temperature was kept constant at 175 ℃ for the rest of the time to allow age hardening and stress relaxation to take place. The total period was up to 18 hours.
- After 18 hours, the furnace was opened. The entire rig together with the held, deformed CAF workpiece and CWBSFA workpiece was removed from the furnace.
- After cooling to the room temperature (up to 3 hours), the nuts were removed from the locking bolts. The CAF workpiece was allowed to springback.
- Both CAF workpiece and CWBSFA piece were placed, centre and aligned properly on top the bottom roller again. The final deformed location of the bottom surface of the workpiece was measured twice and an average value was obtained. (Figure 5.3(i))
- The tests were conducted with three compression displacements, i.e. 20, 30 and 40 mm. Also, using the same experimental settings, CAF tests were repeated on the workpieces of different thicknesses.

(a)

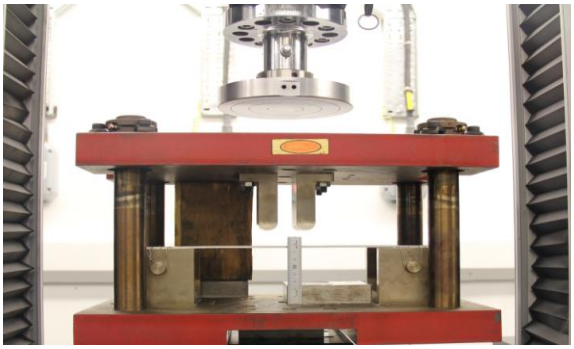

(b)

(c)

(d)

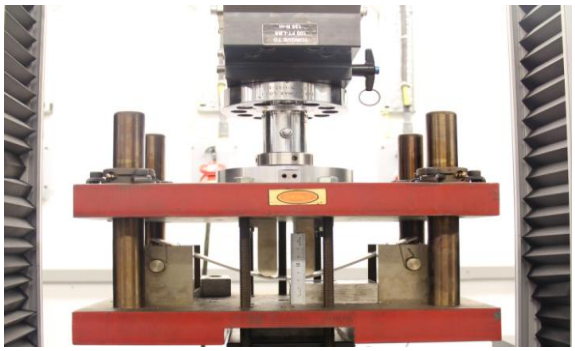

(e - i)

(e - ii)

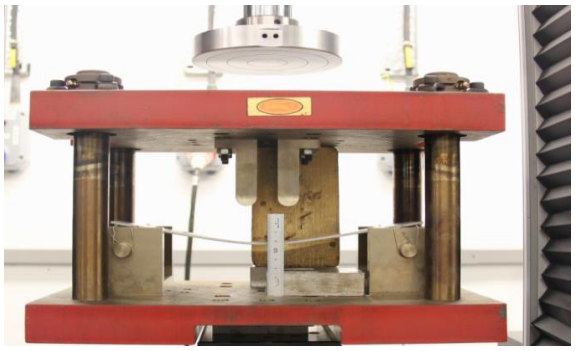

(f)

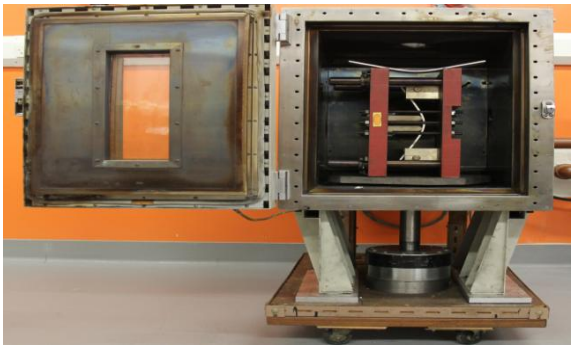

(g)

Figure 5.3: Pictorial illustrations of the experimental test procedures.

## 5.4 Measurement of Deflection and Springback

To measure the deflection and springback of CAF workpiece and CWBSFA workpiece, images were taken by a CANON 60D camera at three instances: (a) before loading, (b) after loading, (c) after unloading (refer to Figure 5.4). $\delta_A$ refers the distance between the bottom surface of undeformed workpiece and bottom frame surface, $\delta_B$ is the distance between the bottom surface of fully loaded workpiece and bottom frame surface, while $\delta_C$ is the distance between the bottom surface of workpiece after springback and bottom frame surface. These measurements were used to evaluate springback. A springback index was introduced as shown in Equation 5.1. $SP = 1$ represents the full springback of the workpiece. If $SP = 0$, no springback occurs.

$$SP = \frac{\delta_C - \delta_B}{\delta_A - \delta_B} \tag{5.1}$$

## 5.5 Experimental Results and Discussion

Several CAF and CWBSFA experiments were performed using the procedures described in Section 5.3. The experimental results for CAF and CWBSFA workpiece were shown in Figure 5.5. In Figure 5.5(i), it shows the comparisons of deformed profiles of CAF (on the top) and CWBSFA (on the bottom) workpiece. The corresponding springback index for each set of experiment was calculated using the method discussed in Section 5.4 and the results are shown in Figure 5.5(ii). For both CAF and CWBSFA workpiece, three phenomena can be summarized from the experiments:

- As the cross head displacement increases, the springback index decreases.

- As the thickness ( $t$ ) of the workpiece increases, the springback index decreases.
- For the same cross head displacement, as the thickness of the workpiece increases, the springback index difference between CAF and CWBSFA workpiece decreases.

(a) (b)

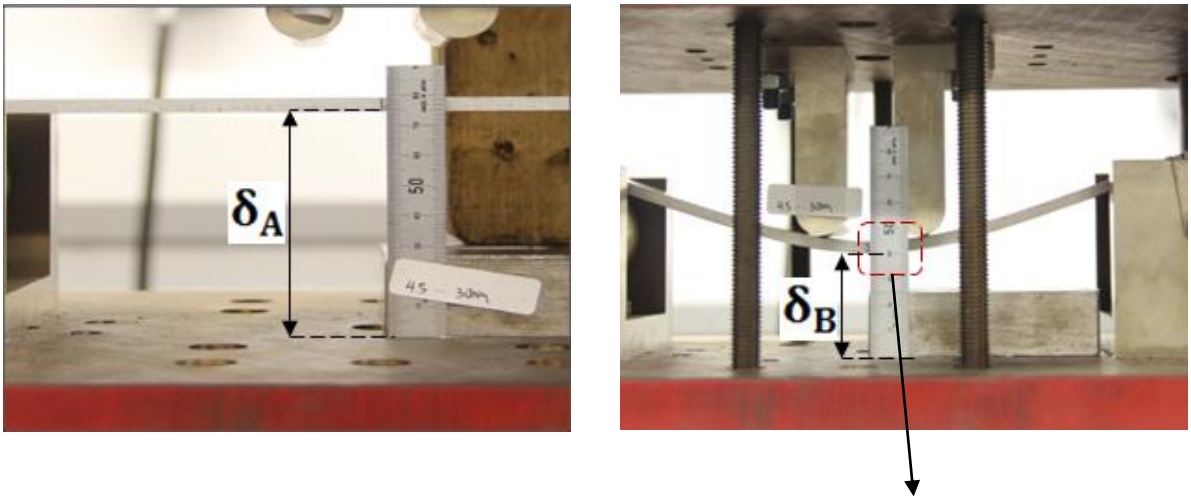


(c)

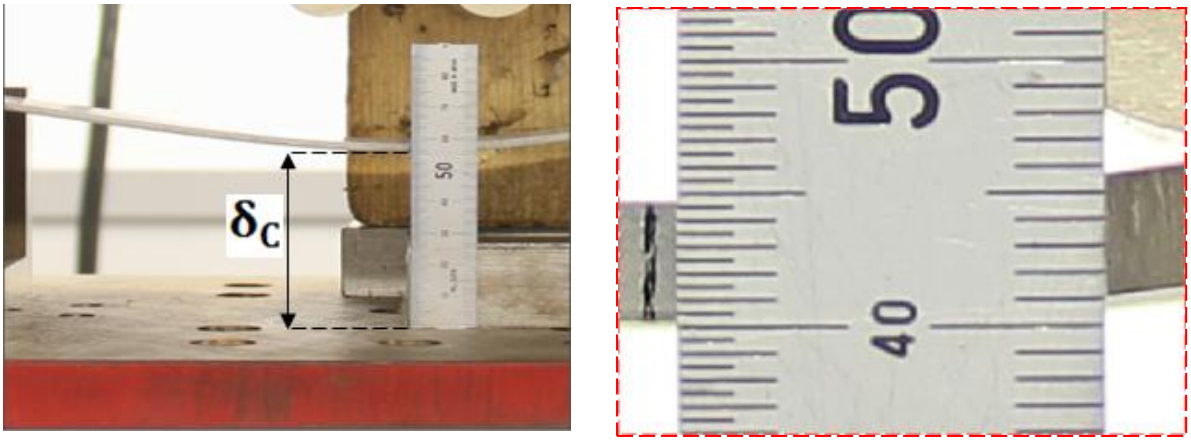


Figure 5.4: Pictorial illustrations of the deflection and springback measurement at (a) the initial (b) fully loaded stage and (c) after springback.

(i) (ii)

(a) t = 3.0 mm

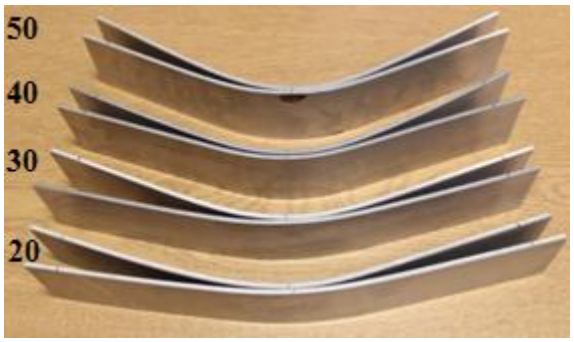


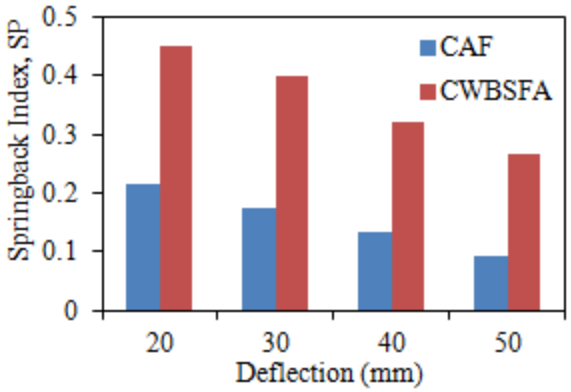


(b) t = 4.5 mm

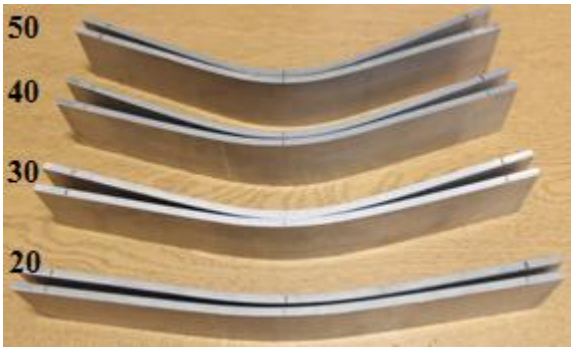


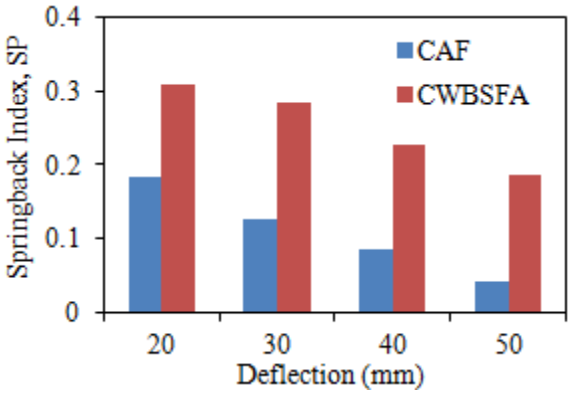


(c) t = 6.0 mm

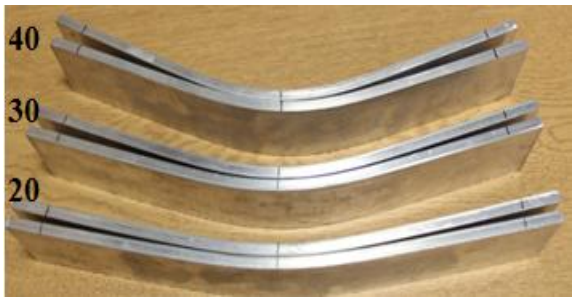


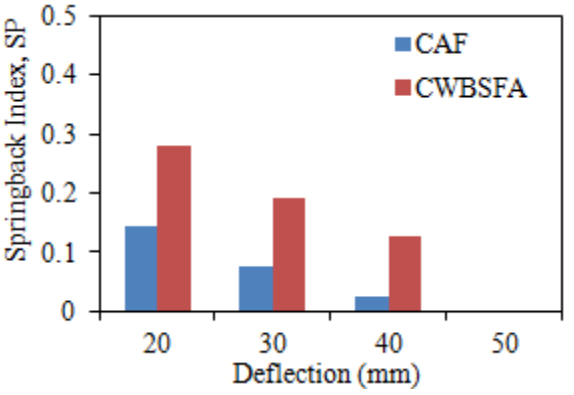


Figure 5.5: Illustration of the (i) profile and (ii) comparison of the springback index between CAF and CWBSFA workpieces with a thickness of (a) 3.0 mm, (b) 4.5 mm and (c) 6.0 mm.

The factors that contribute to these three phenomena are that for all experiments, the maximum induced stresses have already exceeded yield stress. As the cross head displacement and workpiece thickness increases, more plastic strains have been introduced in the workpiece, hence reducing the springback. In other words, less springback occurs in the large deflection case. Springback will be more sensitive in small deflection case. Especially if the maximum induced stress of the material is below yield stress (pure elastic deformation). This will be studied in Chapter 6.

## 5.6 Numerical Validation

### 5.6.1 Details of the FE model

To compare with the experimental investigations, corresponding CAF simulations have been carried out using the FE model as shown in Figure 5.6. The model is basically a four point bending configuration, where there are two large rollers with diameter of 50 mm placed at the bottom as support and two smaller rigid rollers with radius of 10 mm at the top used to bend the workpiece. These rollers are defined as rigid bodies in the simulation. With the convenience of the modelling work, only a quarter models have been established.

Referring to Figure 5.6, the length of each quarter workpiece is 100 mm and the width is 25 mm. The thicknesses are 3.0, 4.5, and 6.0 mm respectively. A total of 246 four-node S4R shell elements were used for the FE simulation. As shown in Figure 5.6, proper boundary conditions were applied to the workpiece to represent those in the tests. Both bottom rollers were fixed at their original location while the top rollers were constrained so that they can move only in –y direction.

Contact pairs were defined between (i) the top rollers and top surfaces of the workpiece; and (ii) the bottom rollers and the bottom surface of the workpiece. The friction coefficients for both contact pairs were taken as 0.1, to simulate the lubricated conditions at the contact area.

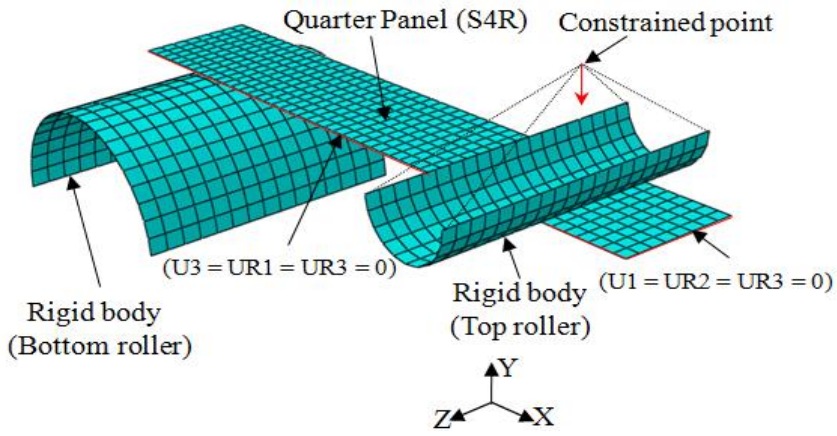


Figure 5.6: FE mesh identifying the boundary conditions for four point bending.

## 5.6.2 FE simulation procedures

Similar to the AA2219 material model settings discussed in Chapter 4. Multi-step numerical procedures have been used to simulate the CAF process and to evaluate the springback using ABAQUS. CAF simulation consists of cylindrically bending the workpiece to different target shape and subsequently holding it at the temperature of 175 ℃ . The target shapes of interest are 20, 30, 40 and/or 50 mm for three thickness workpiece. The total CAF simulation period is 18 hours. The procedures are described as follows:

- The mass of the top frame and roller (8.2 kg) is added on the top roller in the –y direction which elastically displaces and bends the workpiece at 20 ℃ .
- Displace the top roller until the target depth is achieved at 20 ℃ .

- Fix the movement of the top roller so that the AA2219 workpiece is held at the same location. Increase the temperature from 20 ℃ to 175 ℃ and hold the workpiece at 175 ℃ for 18 hours. This allows age hardening, creep and stress relaxation to take place, thus introduces inelastic deformation in the workpiece.
- Remove the constraints of the top roller incrementally after 18 hours and allow the workpiece to springback.

These procedures were repeated for different target displacements and applied to all the workpiece with different thicknesses. Springback index was calculated at the end of each simulation.

### 5.6.3 Springback measurement

The movement of the mid node in y direction (shown in Figure 5.6) at the centre of the workpiece was analyzed throughout the simulation (x and z directions have been constrained). The y coordinates of the mid-node was recorded at three instances similar to the experimental investigation: (a) $y_1$, before loading, (b) $y_2$, after loading and (c) $y_3$, after unloading. The numerical springback index is quantified by

$$SP_n = \frac{|y_2 - y_3|}{|y_1 - y_3|} \qquad (7.2)$$

where $SP_n$ equals 1, the workpiece completely springbacks to its original shape; while $SP_n$ equals 0, there is no springback.

### 5.6.4 FE simulation results

Figure 5.7 shows the simulated maximum (surface) effective stress arising in the AA2219 workpiece during the CAF process. The total time for the deformation is 18 hours.

Figure 5.7 (a) shows the workpiece thickness equals to 6.0 mm. After the workpiece is deformed due to the mass of the top frame and roller, the workpiece is further deformed to its target depth (upper tool displacement) of 30 mm. The equivalent stress at the top surface of the workpiece at the initial stage is shown in Figure 5.7 (a)-(i). The maximum stress level was about 202.5 MPa at the middle of the workpiece, where the workpiece is encountering the highest deformation. The minimum stress level (less than 0.5 MPa) is observed at both ends, where little deformation is taking place. With the workpiece held in place for 18 hours, exposing at the temperature of 175 ℃ , stress relaxation occurs, as shown in Figure 5.7 (a)-(ii). The maximum stress reduces from 202.5 MPa to 109.6 MPa. Figure 5.7 (a)-(iii) represents the residual stress distribution after completely unloading and this is due to the stresses are not fully relaxed by creep. Parallel simulations have been taken with the same target depth of 30 mm on workpiece with a thickness of 3.0 mm and 4.5 mm respectively, as shown in Figure 5.7 (b) and Figure 5.8 (c). Similar residual stress level has been observed for all the three thicknesses. Theoretically, an infinite time period can fully relax the stresses in the panel during CAF, which is not possible in practice. Therefore, springback is unavoidable in CAF.

(a) $t = 6.0$ mm

(i) $T = 0$ hr (Fully loaded)

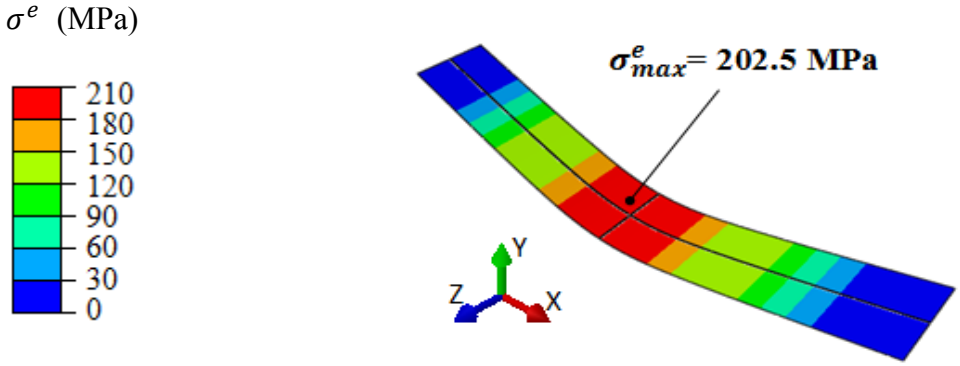

(ii) $T = 18$ hrs (Fully aged)

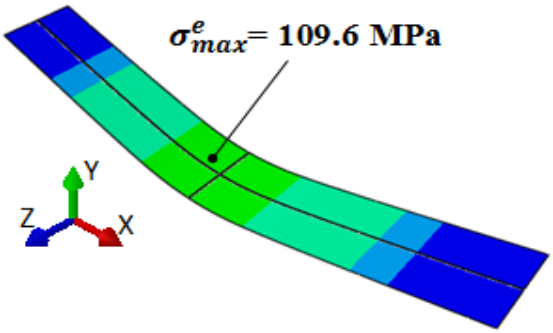


(iii) (After springback)

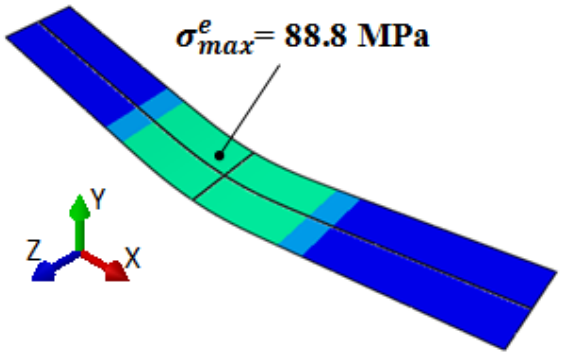


(b) $t = 4.5$ mm

(i) $T = 0$ hr (Fully loaded)

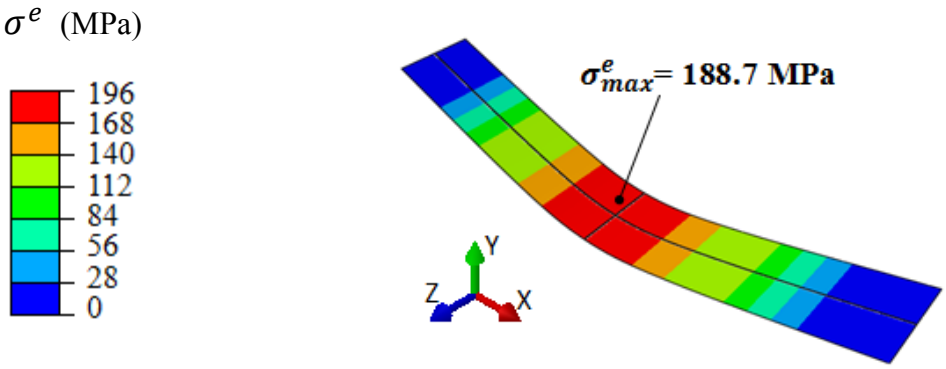


(ii) $T = 18$ hrs (Fully aged)

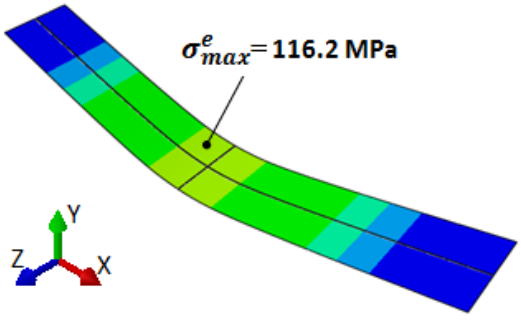


(iii) (After springback)

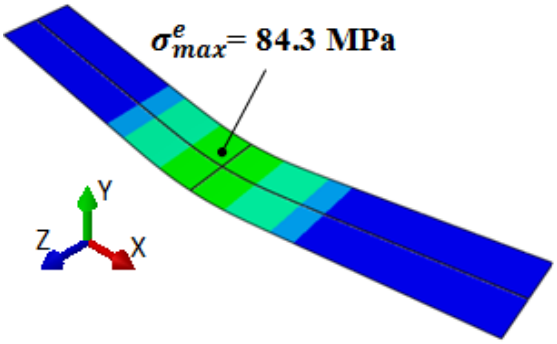

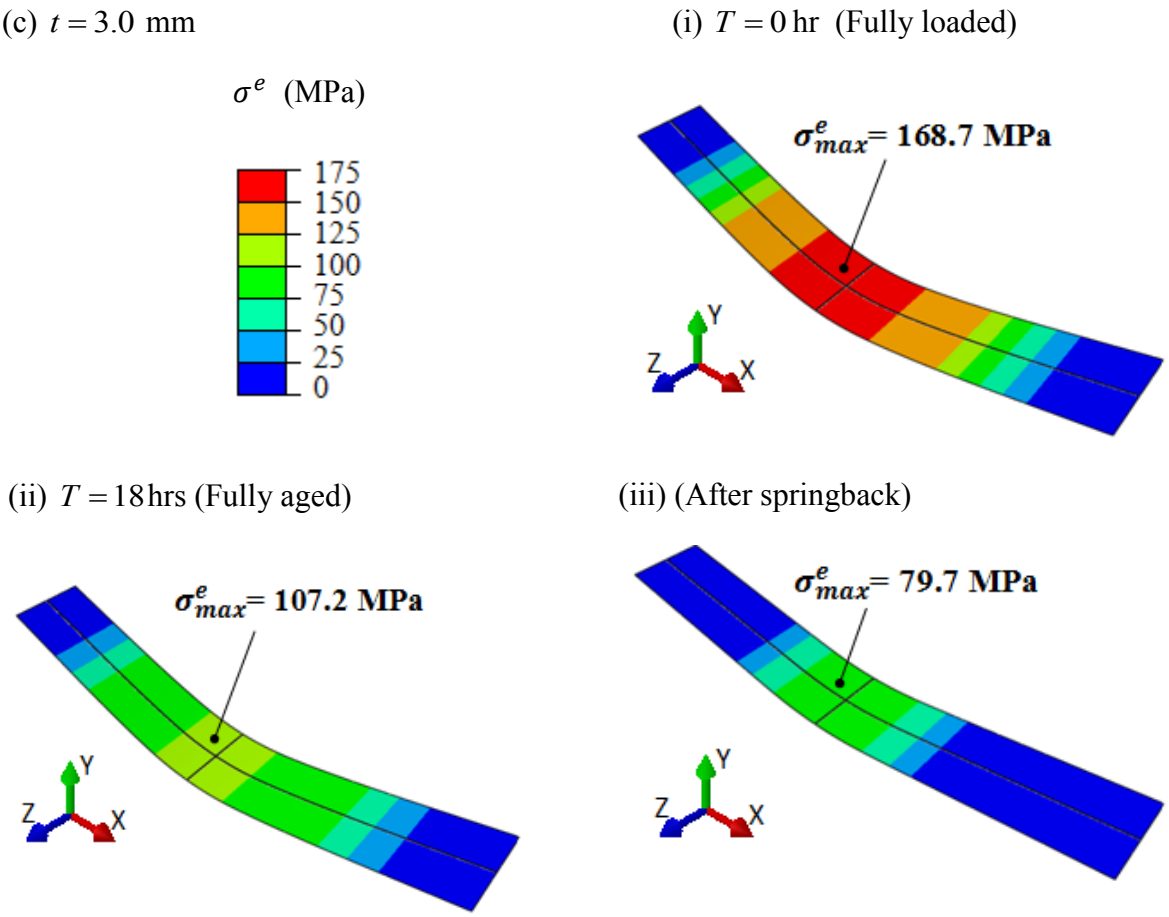


Figure 5.7: Comparison of equivalent stress at the top surface of the workpiece during CAF where initial deflection is 30 mm for workpiece thickness equals (a) 6.0 mm, (b) 4.5 mm and (c) 3.0 mm at (i) the initial, (ii) fully aged stages and (iii) after springback.

### 5.6.5 Springback prediction in CAF

To predict springback, FE simulations and analyses have been carried out in accordance with all experimental CAF results (Figure 5.8). Figure 5.9 shows the comparison of experimental and numerical springback index for different workpiece with different target depth. The predicted springback indices are plotted in Figure 5.9 with solid lines. It is observed that, for the selected range of depths, springback indices for the $t$ = 6.0 mm workpiece vary from 0.039 to 0.165. Meanwhile, for the $t$ = 3.0 mm workpiece, the

springback indices are higher, which vary from 0.112 to 0.233. It can be found that, as the target depth increases, the springback index decreases. Also, when the thickness of the workpiece decreases, the springback index increases.

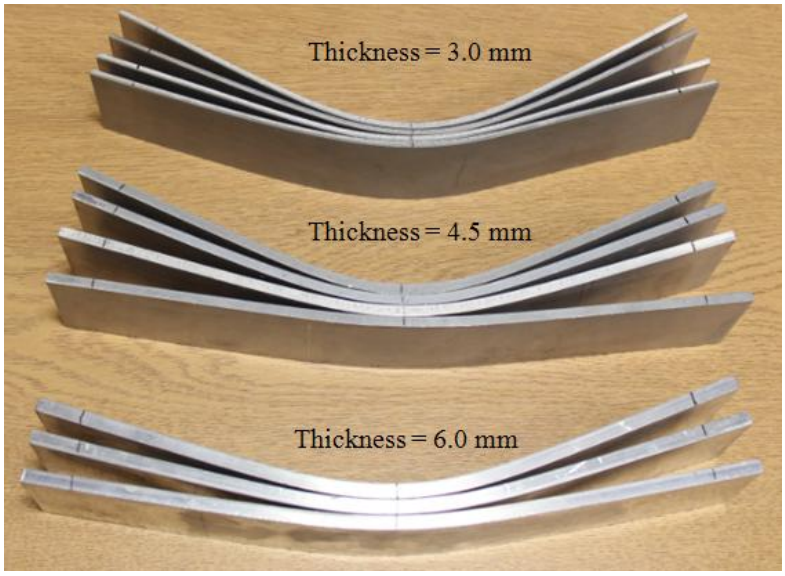


Figure 5.8: Deformed workpieces after creep age forming applied by different initial deflections.

For comparison with the experimental results, the springback indices obtained from experiment are plotted with symbols in Figure 5.9. Similar trends are observed from both experimental and simulated springback index curves. First, as the target depth/displacement of cross head increases, the springback index decreases. Second, as the thickness ($t$) of the workpiece increases, the springback index decreases. For the same target strokes, as the thicknesses of the sheet increase, more strain is accumulated in the outer layer of the sheet, which introduced more stresses and more inelastic deformation in the sheet, which lead to the decrease in springback. The simulated results have over-predicted the springback values with errors less than 12.6%, which is located at $t$ = 4.5 mm at the deflection of 30 mm. The reasons that may contribute to the errors are suggested as follows:

The simulation work does not take the inclusion of thermal stress into consideration during the temperature increase from 20 ℃ to 175 °C. Inclusion of the thermal stress can result in the increase of effective stress level, which subsequently increases the initial creep rate and hence increase the inelastic deformation.

The friction between the workpiece and rigid body was defined as 0.1 and 0.3 to simulate the contact conditions. In the figure, the solid line is the situation that the friction was 0.1, while the dotted line means that the friction was 0.3. The increase of the friction coefficient leads to the decrease of the springback index from the simulation results. However, the practical frictions coefficients were not identified. The real contact conditions at the contact area may result in the difference between the practical and theoretical results.

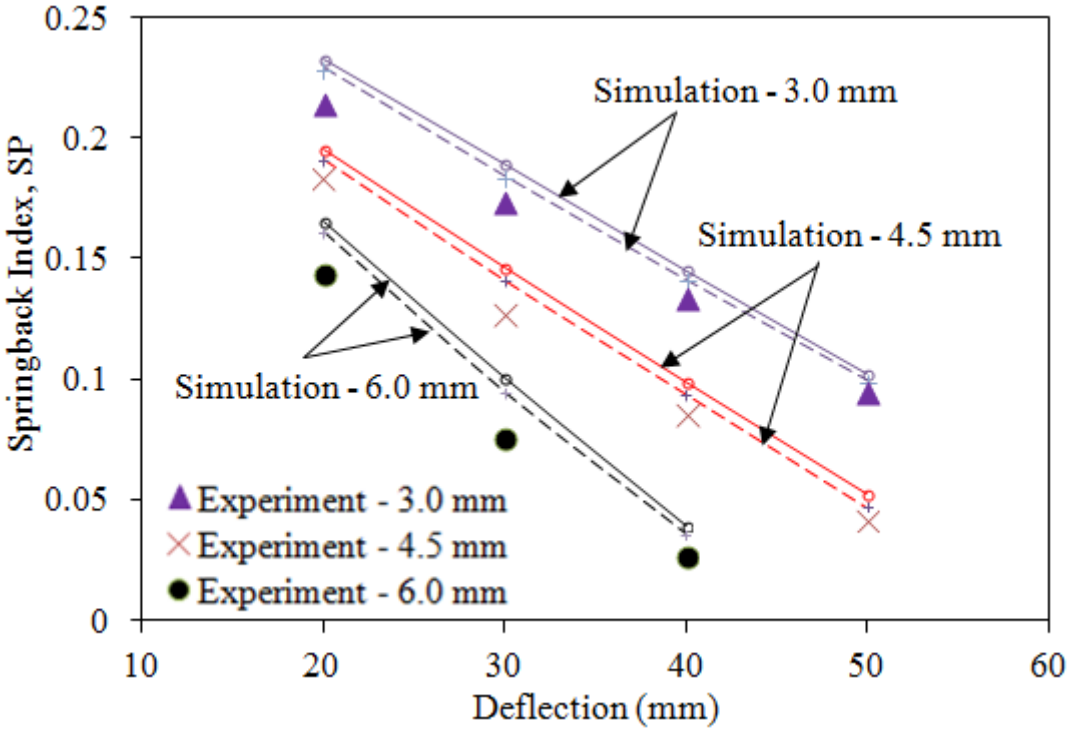


Figure 5.9: Comparison of experimental (symbols) and numerical (solid lines and dotted line) springback index for different panel thicknesses.

## 5.7 Summary

A four point bend rig was designed and assembled. Four point bending tests were carried out to investigate springback in CAF to examine the relationship between the initial deflection and the amount of springback after ageing and more importantly to validate the predicted springback results from the numerical simulation. From the comparison between experimental and numerical results, the simulated FE simulations have slightly over predicted the springback value. However, the maximum errors are no more than 15%, which is due to some simplifications of the numerical model and parameter settings. Generally, both springback indices curves have a similar trend. The comparison has suggested that the proposed FE procedures would be useful to provide as a guideline to predict springback in CAF.

# CHAPTER 6

# Prediction and Assessment of Springback in Typical Creep-age Forming Tools

## 6.1 Introduction

In industrial implementation, creep age forming is often carried out under vacuum or autoclave loading conditions, where a sufficiently high, uniform pressure is required to force the workpiece to contact closely with the tool surface. However, in the labotary, many CAF tests to evaluate springback are performed by clamping the workpiece to both ends of a cylindrical tool and forcing it to the tool surface, which is different from reality. In this chapter, unified creep ageing constitutive equations have been integrated into the commercial finite element code ABAQUS, to analyse a common CAF tester which employs a cylindrical tool shape. Two loading conditions are investigated: (i) end clamp and (ii) uniform pressure. The amount of springback has been predicted, compared and analysed for both loading cases. As discussed in Chapter 5, springback will be more sensitive in small deflection case. Especially if the maximum induced stress of the material is below yield stress (pure elastic deformation). The material modelled in this chapter is AA7055. Its yield strength is 2.5 times than that of AA2219 and all the simulations work of deforming the AA2219 sheet are carried out in the elastic region. The creep-ageing behaviour of AA7055 has been already characterised by Zhan et al. [53].

## 6.2 Numerical Procedures for CAF

### 6.2.1 Unified creep ageing constitutive equations

A unified physically based creep ageing-constitutive model for AA7055, formulated by Zhan et al., [53] has been employed in this work to describe the influence of ageing on the mechanical property evolution and creep deformation behaviour of the Al-alloy 7055 at 120 ℃ under CAF conditions. The model, which has the same manner as AA2219 creep-ageing constitutive equations, is described below:

$$\dot{p} = A_1 \sinh\left\{B_1\left[|\sigma_e|(1-\bar{\rho})\right]-k_0\sigma_y\right\} \tag{6.1}$$

$$\sigma_Y = \sigma_{SS} + \sqrt{\sigma_A{}^2 + \sigma_{dis}{}^2} \tag{6.2}$$

$$\dot{\sigma}_A = C_A \dot{\bar{r}}^{m_1}(1-\bar{r}) \tag{6.3}$$

$$\dot{\sigma}_{SS} = C_{SS}\dot{\bar{r}}^{m_2}(\bar{r}-1) \tag{6.4}$$

$$\dot{\sigma}_{dis} = A_2 n \bar{\rho}^{n-1}\dot{\bar{\rho}} \tag{6.5}$$

$$\dot{\bar{\rho}} = A_3(1-\bar{\rho})|\dot{p}| - C_p\bar{\rho}^{m_5} \tag{6.6}$$

$$\dot{\bar{r}} = C_r(Q-\bar{r})^{m_3}(1+\gamma_0\bar{\rho}^{m_4}) \tag{6.7}$$

$$D_{ij}^P = \left(\frac{3S_{ij}}{2\sigma_e}\right)\dot{p} \tag{6.8}$$

In Eqns (6.1)-(6.8) $A_1$, $B_1$, $k_0$, $C_A$, $m_1$, $C_{ss}$, $m_2$, $A_2$, $n$, $C_r$, $Q$, $m_3$, $m_4$, $A_3$, $\gamma_0$, $C_p$, $m_5$ are material constants. The creep strain rate evolution during ageing is described by Eq. (6.1). Creep strain rate is not only a function of equivalent stress, $\sigma_e$, and dislocation density, $\bar{\rho}$, but

also the yield stress, $\sigma_Y$ , which is a combined function of ageing hardening, $\sigma_A$ , solute hardening, $\sigma_{ss}$ , and dislocation hardening, $\sigma_{dis}$ , as summarized in Eq. (6.2-6.4). These represent the evolution of age hardening and solute hardening, which are described in terms of normalised precipitate size, $\bar{r}$ and evolutional rate, $\dot{\bar{r}}$ , described in Eq. (6.7). Equation (6.5) represents the dislocation hardening rate, which is related to dynamic and static recovery and is a function of normalised dislocation density. As precipitates evolve or grow monotonically during isothermal ageing, the coarsening kinetics of the ageing mechanism is modelled using a normalised precipitate size growth Eq. (6.7), in which the nucleation and growth of precipitates are related to the dislocation density stated in Eq. (6.6). For Eq. (6.8), it represents the plastic deformation in a multi-axial manner.

The material constants in the constitutive equations were determined by Zhan et al. by fitting to experimental data using evolutionary algorithms (EA) based on optimisation methods. Their resultant values are given in Table 6.1.

Table 6.1: Constants in the CAF constitutive equations for AA7055 at 120 °C [53].

| $A_1$ ($h^{-1}$) | $B_1$ (MPa) | $k_0$ | $C_A$ (MPa) | $m_1$ | $C_{ss}$ (MPa) | $m_2$ | $n$ | $A_2$ |
|---|---|---|---|---|---|---|---|---|
| 5.0E-5 | 0.0279 | 0.2 | 94.3 | 0.44 | 20.0 | 0.4 | 0.8 | 291.5 |
| $C_r$ ($h^{-1}$) | $Q$ | $\gamma_0$ | $m_3$ | $m_4$ | $A_3$ | $C_p$ | $m_5$ | |
| 0.032 | 1.69 | 2.7 | 1.3 | 1.98 | 200.0 | 0.07 | 1.3 | |

### 6.2.2 FE model and numerical procedures

Two finite element models have been developed to represent the cylindrical die and work piece under both loading conditions, as schematically illustrated in Figure 6.1(a) for the end clamp condition and Figure 6.1(b) for the uniform pressure condition. Due to the symmetrical nature of the geometries, a half model was created employing appropriate symmetry boundary conditions. The CAF simulation consisted of holding a 12 mm thick, initially flat rectilinear workpiece of half dimensions 185 mm × 80 mm × 12 mm of an aluminium alloy AA7055 against the die's surface, and subsequent creep age-forming it at a constant temperature of 120 °C for 20 hrs. The die's surface had a radius of 1400 mm and was assumed rigid. Four node reduced integration shell elements were employed to model the workpiece. A friction coefficient of 0.1, which is related to the contact pair, was specified to simulate a non-lubricated condition. For the convenience of locating the workpiece on the tool surface and avoiding contact convergence in the implicit forming simulation, two ground springs of stiffness of $1\times10^{-6}$ N mm$^{-1}$, which can be compressed to zero volume, were used to support the weight of the workpiece at its corners, as shown for example in Figure 6.1(b).

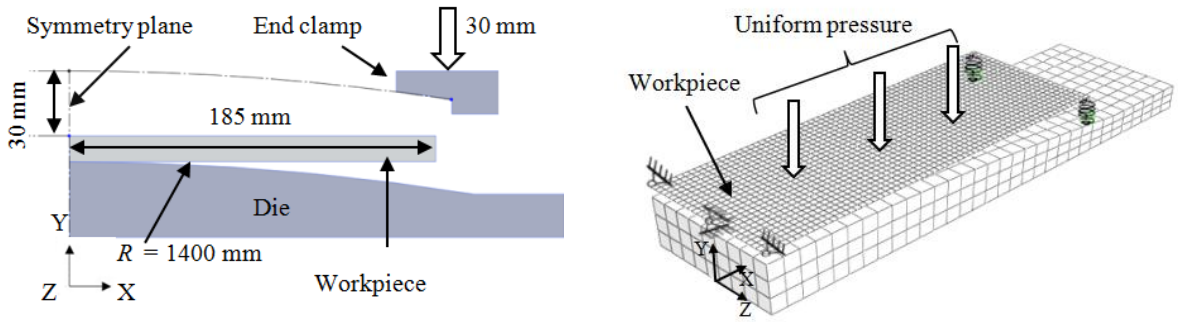


(a) End clamp loading (b) Uniform pressure loading

Figure 6.1: Numerical models with loading and boundary conditions.

To simulate the end clamp condition, initially a 30 mm displacement was applied in the downward (-*y*) direction to overcome the stiffness of the two ground springs and to ensure the corners of the workpiece were in direct contact with the tool surface. This end displacement was held for a time of 20 hrs, allowing ageing, creep and stress relaxation to take place. Finally, this end clamp displacement was removed incrementally, enabling the aluminium workpiece to springback.

For the uniform pressure condition a two-step analysis was also performed. Initially an 18 MPa load was applied incrementally in a static analysis, followed by a visco step where this load was held over a period of 20 hrs to the entire top surface of the workpiece, causing it to form the required shape. Similarly to the end clamp condition, this pressure was held for 20 hrs and then released, enabling the workpiece to spring back to its final deformed shape which was measured.

Mesh convergence studies have been performed in this chapter as well with different size of mesh e.g. 15 mm, 10 mm, 5 mm and 4 mm. Good agreements have been obtained by using the mesh size of 5 mm and 4 mm. In this simulation, a mesh size of 4 mm is applied. A detailed convergence study is shown in Appendix B to investigate the effect of implementation different size mesh.

## 6.3 Overall CAF process and springback assessment

### 6.3.1 Equivalent Stress Distribution

A contour plot of the equivalent (Mises) stress distribution, which controls the creep strain rate, over the workpiece's surface is shown in Figure 6.2 for the (a) end clamp and (b) uniform pressure condition (18 MPa) at three stages in time. Stage (i) $T = 0$ hr is the initial fully loaded condition where the ground springs were compressed to overcome their stiffness

by the end clamp's vertical displacement or by the applied pressure, and the whole workpiece deformed towards the die's surface. At this stage, for the end clamp condition, around half of the workpiece experiences high stress greater than 300 MPa, whereas for the uniform pressure condition the majority of the workpiece has a relatively uniform stress distribution between 280-300 MPa. The maximum stress attained was around 321 MPa and 306 MPa for end clamp and uniform pressure condition, respectively. In all cases the stresses were below the yield stress of the material which is around 361 MPa. The equivalent stresses at the corner is 14 MPa lower than that in the inner of the plate, this is due to the implementation of springs at the corner.

Significant stress relaxation due to creep took place, generally reducing the equivalent stress by approximately 50% to a maximum of 145 MPa and 151 MPa for the end clamped and uniform pressure condition, respectively, at the end of ageing period (Figure 6.2 (ii)). Though higher stresses were initially attained on loading for the end clamped condition compared to the uniform pressure condition, stress redistribution effects have lead to marginally higher stresses in the uniformly pressurised workpiece post-aging.

On removal of the applied loads, springback occurred and a residual stress remained in the workpieces. As shown in Figure 6.2 (iii), similar stress levels reside in the workpieces for both loading conditions. For the end clamp condition, the majority of residual stress distribution was released to below 40 MPa, which is similar to, but marginally lower than the uniform pressure condition (Max. 44 MPa). In all cases, as expected, the stresses are symmetrical about the workpieces' longitudinal centreline.

$\sigma^e$ (MPa)

(i) $T = 0$ hr

(Fully loaded)

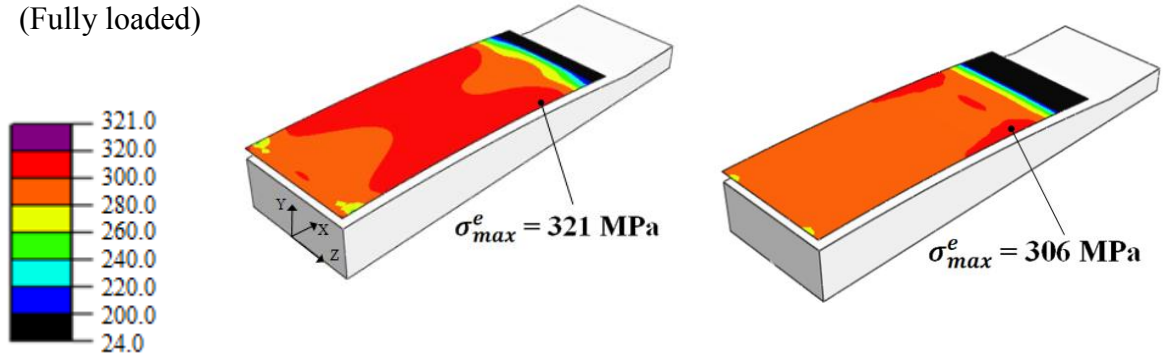


(ii) $T = 20$ hrs

(Fully aged)

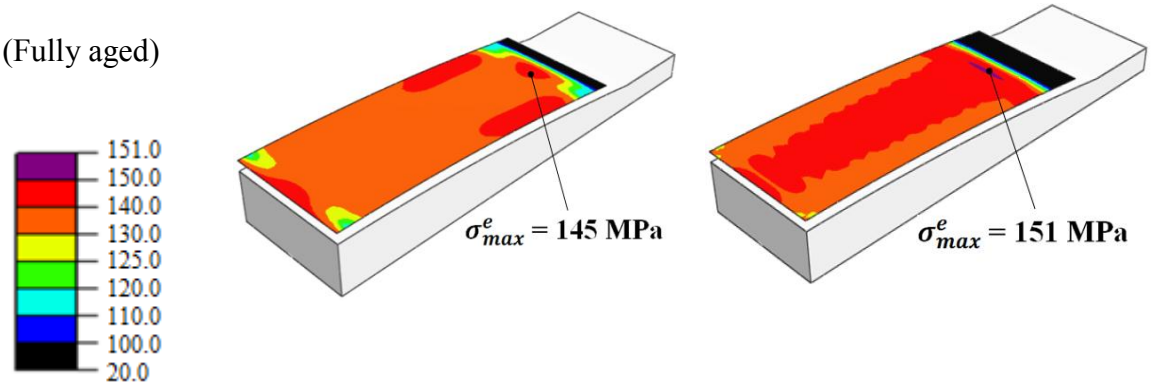


(iii) (After springback)

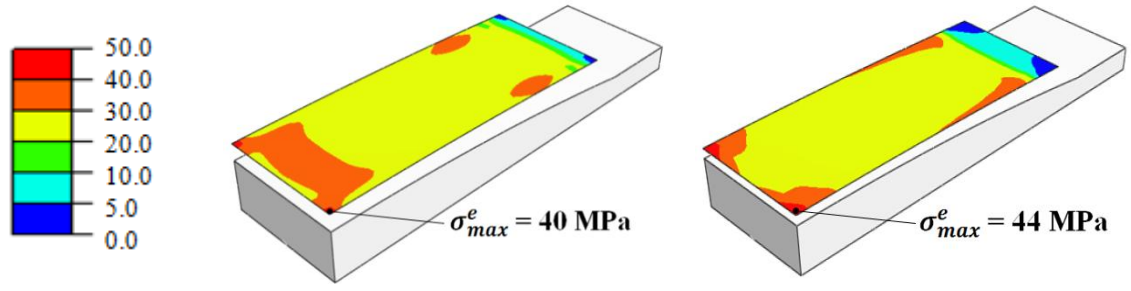


(a) End clamp (b) Uniform pressure

Figure 6.2: Comparison of top surface equivalent stress of the workpiece for (a) End clamp and (b) Uniform pressure loading conditions at (i) the initial, (ii) fully aged stages and (iii) after springback.

### 6.3.2 Contact stress distribution

In addition to the bending stresses in the workpiece, stresses are also generated due to the reaction force between the workpiece and die. Good contact between the die and workpiece promotes the workpiece to conform to the die's profile. Therefore, contact pressure may be used as a measure of the contact between the workpiece and die. Figure 6.3 shows the contact pressure distribution upon the upper surface of the die at (i) the initial and (ii) fully aged stages for both the (a) end clamped and (b) uniform pressure condition. As seen in Figure 6.3(a), the contact pressure is small except in the vicinity of the clamps where a maximum pressure of 100 MPa is observed on initial loading, which reduces by approx 20% after 20 hrs of ageing. Contact is achieved over the majority of the surface for the applied pressure loading condition (Figure 6.3(b)). The contact pressure is around 20-58 MPa except close to the workpiece edges where no contact is achieved. After ageing a similar pressure distribution was observed with a peak value reduction of around 22%.

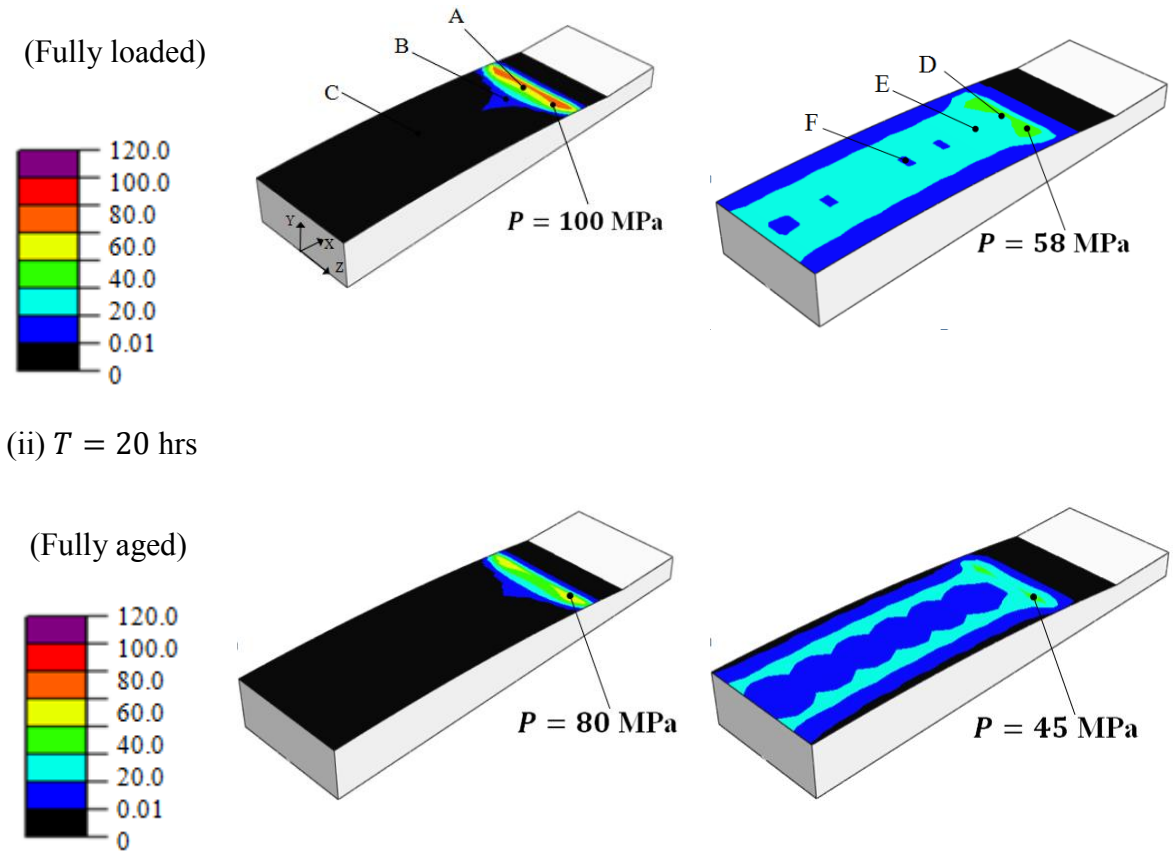


Figure 6.3**:** Comparisons of contact pressure on the die for (a) end clamp and (b) uniform pressure loading.

To examine the influence stress relaxation during CAF on the contact pressure in detail, three feature points have been identified on each workpiece, as shown in Figure 6.3 (i). Feature points A, B, and C on the end clamp die are located at *x* co-ordinate distances of 182 mm, 170 mm and 100 mm, respectively. Similarly points D, E, F on the uniformly pressurised die are located at *x* co-ordinate distances of 155 mm, 140 mm, and 100 mm respectively. The variations in contact pressure during CAF at these points are compared in

Figure 6.4. Since there is no contact pressure at Node C and it is excluded from Figure 6.4. Note that in this and subsequent figure, solid lines are used to signify initial loading conditions ($T$ = 0 hr) and dashed lines for data at 20 hrs of CAF.

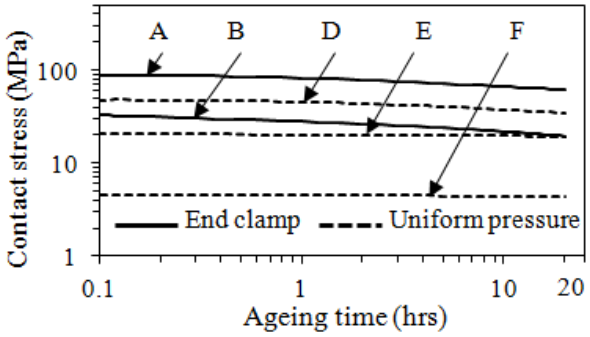


Figure 6.4: Variation of contact pressure during CAF for node A, B (Solid line) and node D, E, F (dotted lines) on die Shown in Figure 6.3.

Each curve exhibits the stress relaxation and it can be seen that the stresses release by 26.46 MPa (Node A), 13.39 MPa (Node B), 13.28 (Node D), 1.23 (Node E), 0.22 MPa (Node F) after 20 hours ageing. In comparison, uniform pressure presents a more stable stress relaxation rate than that of the end clamp condition. For each condition the stress relaxation rate increased with an increase in the initial stress.

The stresses in the end clamp loading case, which resembles a three point bending configuration, are dominated by bending stresses and little contact is made between the workpiece and die. Therefore, the shape of the deformed workpiece is mainly related to the bending stress distribution and not to the shape of the die's surface. For the uniform pressure loading case, 18 MPa has been found insufficient to achieve full contact between the workpiece and die's surface, and a noticeable gap existed between the workpiece and die at its ends.

The variation in the gap between the workpiece and die, from the point of initial loading to the end of 20 hrs aging, along the workpiece for both loading conditions is shown in Figure 6.5. For the uniform pressure condition, there is no contact for 10.3% of the workpiece's area on initial loading ($T = 0$ hr) which decreases marginally to 9.4% after 20 hrs aging. Whilst for the end clamp condition, the workpiece and die are only in contact under the clamps themselves and at mid-length of the workpiece (i.e. the plane symmetry line on the workpiece surface). Figure 6.5 shows the vertical distance (gap) between the tool and workpiece as a function of distance from the mid-length of the workpiece ($x = 0$). A parabolic profile is seen in Figure 6.5 between the clamped area and mid length of the workpiece. As explained in the ABAQUS manual contact pressure can only be generated between two deformable surfaces and cannot be generated for line-surface contact [122]. Hence, no contact pressure can be simulated at the mid-length of the plate and a small gap of $1\times10^{-3}$ mm exists at the mid-length. The gap increases to a peak value of 0.072 mm at 85 mm from the workpiece's mid-length on initial loading. After 20 hrs, a similar trend in the gap's profile can be seen, but the peak value has almost doubled to 0.147 mm.

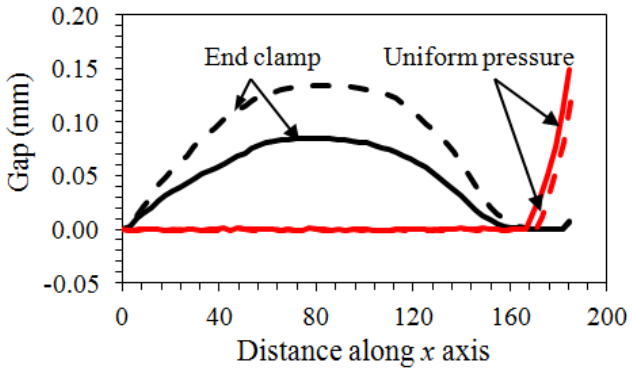


Figure 6.5: Variations of gap between workpiece and die for end clamping and air pressure conditions at ageing time) $T = 0$ hr (solid lines) and $T = 20$ hrs (dotted lines).

### 6.3.3 Overall springback assessment

Significant work has been performed to assess springback of the overall structure by several researchers [123-125]. The typical engineering approach to quantify springback is to evaluate the springback factor, *S*, which is given by

$$S = \left(1 - \frac{\delta_f}{\delta_0}\right) \tag{6.9}$$

where $\delta_0$ is the maximum vertical distance on the workpiece when fully loaded, while $\delta_f$ is the final maximum vertical distance on the workpiece after springback, as illustrated in Figure 6.6. If $S = 1$, the workpiece springs back to its initial shape and if $S = 0$, there is no springback at all.

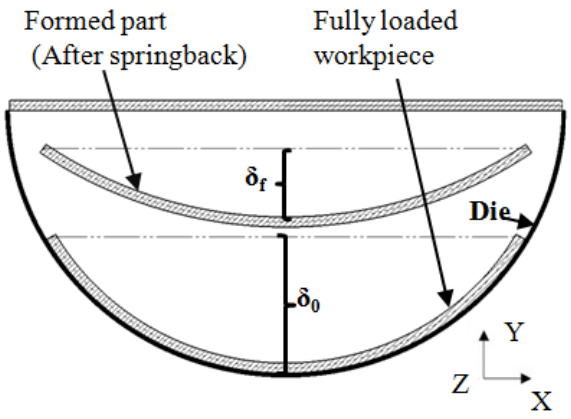


Figure 6.6: Overall springback is defined by a factor $S = (1 - \delta_f / \delta_0)$, where $S = 0$ represents no springback, $S = 1$ represents fully springback.

The maximum vertical distance relative to the workpiece edge (see Figure 6.7) was taken at two instances: (i) fully loaded and (ii) after springback. These measurements were used to evaluate springback. The overall springback factor for end clamp condition is 0.568,

which is smaller than that of the uniform pressure condition which has a factor of 0.575. The overall magnitudes of springback are similar.

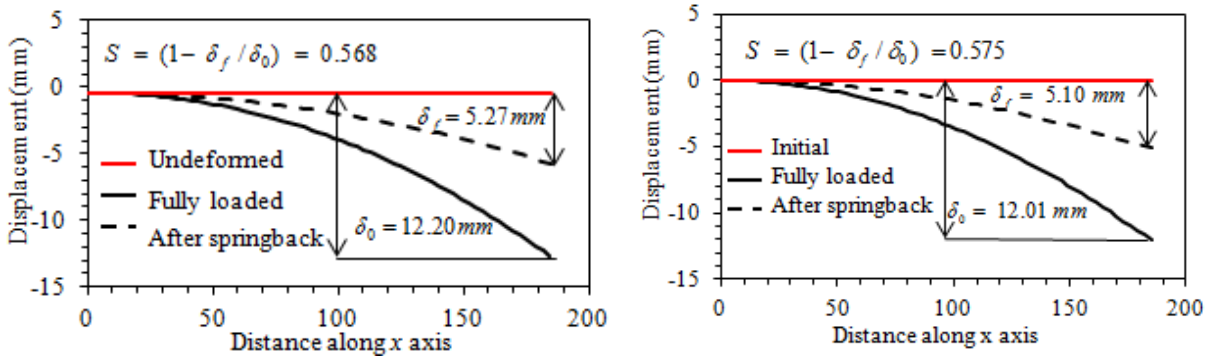


(a) End clamp loading (b) Uniform pressure loading

Figure 6.7: Overall springback predicted using the two loading cases of (a) end clamp and (b) uniform pressure.

## 6.4 Localized springback assessment

### 6.4.1 Definition of springback based on local curvatures

A detailed analysis of the deformed shape of the workpiece after springback can be obtained by local curvature measurements around the circumference of the workpiece. A schematic illustration is shown in Figure 6.8 to demonstrate the local curvature determination method. Along the workpiece transverse direction, several localised curvatures can be identified and these localised features enable the 'quality' of the workpiece's shape to be assessed at fully loaded and post springback conditions. To achieve a high resolution and stable curvature distribution, co-ordinates of three nodes located at the mid-thickness and width of the workpiece with an increment of 10 nodes between them (corresponding to an initial undeformed separation of 30 mm), were selected. The local radius of curvature $R_i$ of a

workpiece was determined using the co-ordinate measurements of these three nodes using Eqns (6.10) and (6.11) below

$$R_i = \sqrt{(X_i - O_{IX})^2 + (Y_i - O_{IY})^2} \tag{6.10}$$

$$(O_{iX}, O_{iY}) = F\{(X_{i-10}, Y_{i-10}), (X_i, Y_i), (X_{i+10}, Y_{i+10})\} \tag{6.11}$$

where $(X_{i-10}, Y_{i-10})$, $(X_i, Y_i)$, $(X_{i+10}, Y_{i+10})$ are the coordinates of the three selected nodes and $(O_{ix}, O_{iy})$ are the coordinates for the centre of curvature, where $i$ is the node number. Note that each localised curvature set of three nodes selected are identified by the mid node number in the set. Further details for determining the local radius of curvature can be found in [126]. In the FE model there are 63 nodes along the length of the half workpiece, from the mid symmetry plane to the right end.

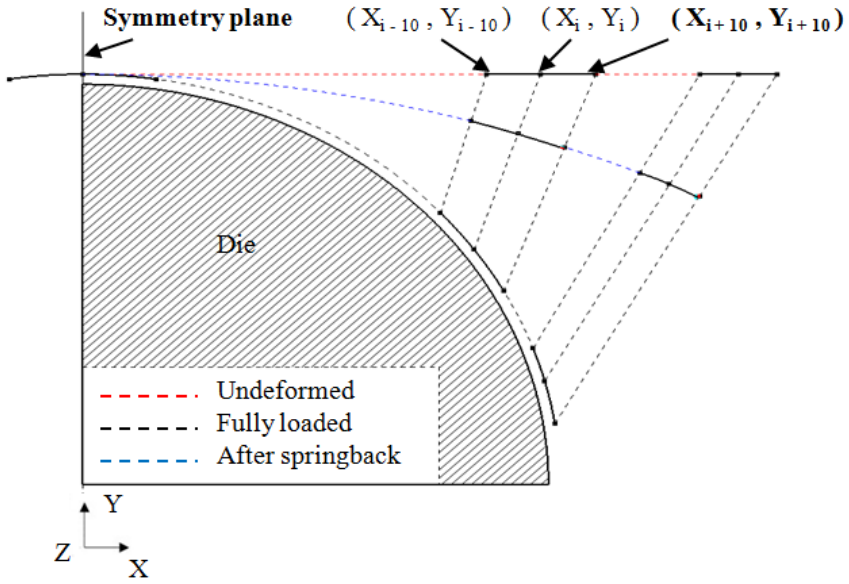


Figure 6.8: Schematic illustration for local curvature determination method.

Using these localised curvature measurements, a curvature index, *CI*, has been defined to quantify the deviation in the workpiece's geometry from that of the tool at any instant during the CAF procedure. The curvature index is defined through Eqns (6.12-6.13)

$$CI = \left(1 - \frac{R_e}{R_i}\right) \tag{6.12}$$

$$R_e = R_{tool} + \frac{t}{2} \tag{6.13}$$

where $R_i$ is the instantaneous local radius of curvature (see Eqns 6.10-6.11), $R_{tool}$ is the die's radius, and *t* is the thickness of the workpiece.

A $CI$ of unity indicates that the workpiece has no curvature and maintains its initial, undeformed shape. A $CI$ equal to zero means that the workpiece has the exact same shape as the die. This $CI$ factor enables the workpiece's shape to be evaluated at full load and after springback.

Similarly, a springback index, $SI$, is defined in Eqn (6.14) to compare the workpiece's geometry before the load is removed at the end of the CAF process and after springback occurs. The springback index is mathematically defined as

$$SI = \left(1 - \frac{R_i}{R_i'}\right) \tag{6.14}$$

where $R_i$ and $R_i'$ are the localised curvature at fully loaded and post springback conditions, respectively. A $SI = 0$ indicates the two curvatures at, pre and post load removal, are identical whereas $SI = 1$ means that the workpiece springs back to initial undeformed condition.

### 6.4.2 Local springback assessment

The variation of the curvature index $CI$ along the length of the workpiece at the initial fully loaded condition ($T$ = 0 hr) are compared in Figure 6.9 for the end clamp and uniform pressure loading conditions. The distance along the workpiece is identified by the undeformed $x$ co-ordinates of the mid nodes (0 mm-156 mm) in the set used for the curvature measurement.

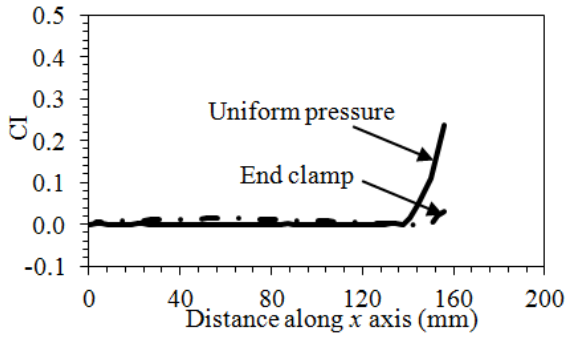


Figure 6.9: Comparison of curvature index variation along the workpiece for the end clamp and uniform pressure conditions at time $T = 0$ hr (Fully loaded).

Along the circumference of the workpiece, from its midpoint to end, the local curvature index, for the case of uniform pressure, starts to increase from 0 at 126 mm from the workpiece's midlength, which indicates that there is a small gap between the end area of workpiece and the die and that the majority of the workpiece is pressed tightly against the die's surface. For the end clamp condition, the localised curvature has a parabolic profile between the workpiece's midlength and the clamp's point of contact (149 mm from the workpiece's mid length) with a peak value of 0.014 at 66 mm from the workpiece's midlength. At the end area of the workpiece the curvature index increase again to 0.019 due to the line contact between the clamp and workpiece at 173 mm from the workpiece's

midlength (Note that there is no contact between the clamp and workpiece for a distance of 12 mm from the end of the workpiece. In general however, the localised *CI* for the clamped workpiece is just above 0, indicating a small gap between the workpiece and die. These results are consistent with those observed in Figure 6.5 and demonstrate that there are some significant differences in the CAF process for both loading conditions.

The effect of springback on the local curvature of the workpiece for both loading conditions has also been evaluated, as shown in Fig 6.10. The trend clearly indicates that the springback results depend on the loading conditions.

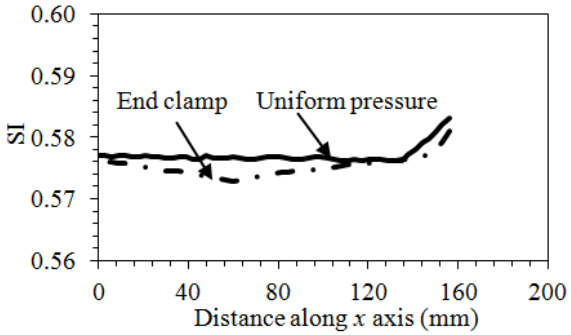


Figure 6.10: Comparison of curvature index variation along the workpiece for the end clamp and uniform pressure conditions after springback.

The localised springback index for uniform pressure conditions increases significantly at the end of the workpiece, but is relatively uniform at other regions. Similar trends are seen for the end clamp condition. However there are greater fluctuations in the SI values observed. The average SI value for end clamp condition is 0.575 with a standard deviation of 0.11%, and 0.578 for the uniform pressure case, with a standard deviation of 0.03%.

The SI value for the end clamped condition is less than that of the uniform pressure loading condition, on average by 0.56%. This corresponds to that found in the overall

springback assessment, where the overall springback factor for the end clamped condition was 1.2% less than that for the uniform pressure condition. However, the lower standard deviation in the *SI* for the uniform pressure case indicates that springback is relatively consistent over the workpiece. Therefore a uniform springback factor over the workpiece can be achieved, which enables tools to be designed to compensate for springback more easily.

### 6.4.3 Sensitivity of springback to vacuum loading pressure

A sensitivity study has been performed to determine the influence of the pressure magnitude on the *CI*. Three values of pressure have been considered in total *i.e.* 10 MPa, 18 MPa and 30 MPa. For each load the local *CI* has been evaluated on initial loading ($T$ = 0 hr) and after springback, as shown in Figure 6.11 (a) and (b), respectively.

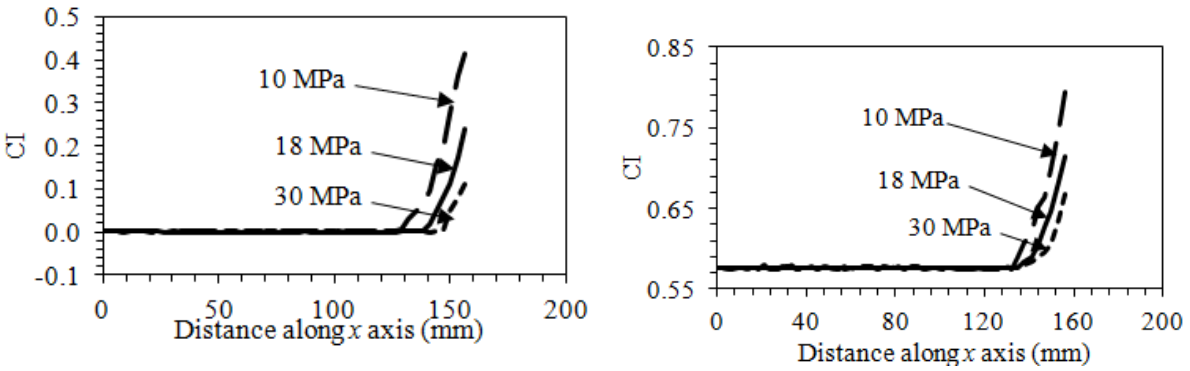


(a) Fully loaded (b) After springback

Figure 6.11: The effect of uniform pressure magnitude on the curvature index variation along the length of the workpiece from its centre point (a) under full load and (b) after springback.

Under full load, the *CI* at the end of the workpiece with a pressure of 30 MPa is four times less than that at 10 MPa. An increase in pressure enables the *CI* to reduce to a stable value of 0 over shorter distances from the workpiece edge. Similar overall trends are seen in Figure 6.11 (b) after springback. The *CI* at the end of the workpiece at 10 MPa pressure reaches 0.82, while for 18 MPa and 30 MPa, this reduces to 0.721 and 0.673, respectively. The *CI* for all three cases stabilises at value of around 0.575, with a standard deviation of 0.03%. These results indicate that, with a sufficiently high pressure, a workpiece with a stable *CI* distribution can be achieved.

## 6.5 Summary

Numerical models have been established to analyse the difference in springback predictions between the two loading cases: end clamp and uniform pressure. The former is often used in small scale laboratory testing and the latter in real industrial forming processes.

Good contact between the tool and workpiece's surfaces were achieved for the uniform pressure condition, providing sufficient pressure was applied, except close to the plate edge where no contact was observed. In contrast, contact was only achieved at the mid length of the end clamped workpiece and that contact was in the vicinity of the clamps themselves. A parabolic profile was found to exist between the middle of the specimen and the end clamp position. For the uniform pressure condition, the size of the gap decreases with pressure magnitude and ageing time. A method has been established to assess the local curvature and local springback values for the formed parts. For the uniform pressure loading, the springback is relatively uniform apart from at the ends. However, for the end loading case, the amount of springback varies noticeably along the length of the workpiece. These

differences observed between the two loading conditions will increase with component size and hence will cause significant variation in the curvature of the formed parts. Thus for a large scale component the springback evaluated from end clamping could not be used for assessing the springback from uniform pressure loading. It is recommended that laboratory scale end clamping tests should not be used to model springback features for the real vacuum forming processes as the local springback distributions are significantly different, even if the overall magnitudes are similar.

# CHAPTER 7

# Integrated Design for Creep Age Forming Isogrid Structures

## 7.1 Introduction

Shaping the specified structures using CAF is based on the stress relaxation behaviour due to creep, which occurs during the artificial ageing process. However, due to the time and temperature restrictions in CAF being specified to achieve a particular requirement of mechanical properties, the residual stress could not be fully released during CAF, and thus springback takes place.

Springback is one of the main drawbacks of CAF, which may lead to the formed structure being out of tolerance, introducing problems during assembly or installation. The common methodology to compensate springback by industry relies on trial and error, recursively modifying the tool shape until the formed structure springbacks to the required shape. Practically, the methodology above is costly, laborious and time consuming. It is therefore significant to develop an integrated system to predict the springback behaviour of the formed structures via numerical simulation, and subsequently modify the tool shape to compensate springback [127-132]. To creep-age form the isogrid panel, two types of loading methods can be employed, as shown in Figure 7.1. For autoclave forming condition, only a bottom die is required for manufacturing ultra large components. However, a pressurized autoclave, though adds significant cost. While for mechanical forming condition, this is similar to the traditional sheet metal forming process, e.g. stamping. The furnace used for

ageing would not lead to significant extra cost, as an ageing furnace would be required to increase alloy mechanical properties in any type of processing route. However, an upper die would be heavy, difficult to handle and requires extra cost for tool machining. In addition, high temperature resist material should be used to fill into the isogrid structures to stabilize the isogrid rib stiffeners, in order to distribute the forming/bending force through the compression/bending process [133, 134].

Stage 1: Isogrid panel prior to CAF

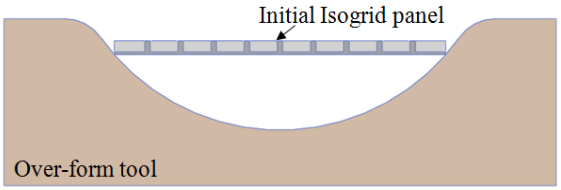


Stage 2: Isogrid panel reconfigured to the tool shape by either autoclave method or mechanical method

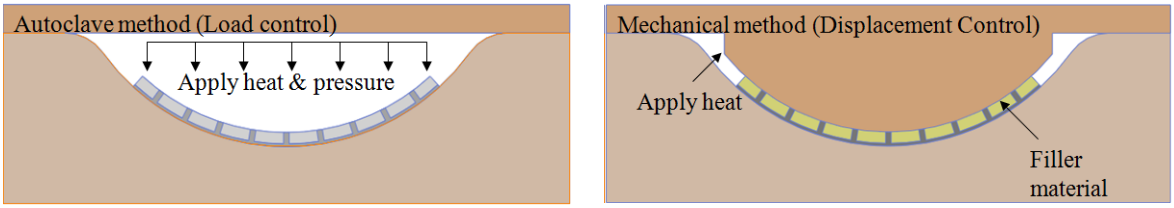


Stage 3: Final creep age-formed isogrid panel after springback

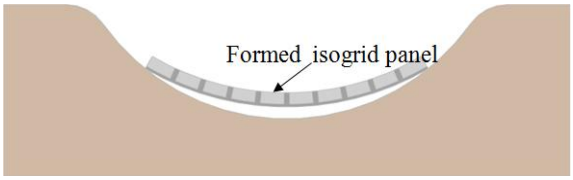


Figure 7.1: Illustrations of the three stages in the CAF process for forming isogrid panel.

This chapter contains an integrated creep age forming proposal for forming a 1/3 cylindrical isogrid structures by considering the autoclave creep age forming condition.

Based on the proposal, a description of integrated numerical procedures was given, in accordance with an offsetting tool shape methodology to compensate springback in CAF. Thereafter, the prediction of residual stress, springback and shape information was carried out using ABAQUS. Based upon the FE simulation results, a new tool surface has been finalized by using the tool offsetting algorithm. Finally, a proposed CAF process for forming 1/3 pieces isogrid cylindrical assembly by autoclave forming has been developed.

## 7.2 Integrated numerical procedures

The framework of integrate systems for springback behaviour investigation and tool shape determination is shown in Figure 7.2. The integrated system is divided into three stages over a loop: tool surface definition, FE simulation using FE solver and application of tool offsetting algorithm. These procedures are iterative processes with the aim of acquiring the final tool shape. This chapter mainly focuses on the establishment of FE simulation procedures by applying the creep-ageing model into the simulation of creep age forming of the AA2219 isogrid structures. Referring to Figure 7.2, the geometric data points for both AA2219 isogrid panel and tool surfaces were formulated in Solidworks in SAT format and then imported into ABAQUS. For the first iteration, the outside radius of desired isogrid panel was considered as the initial tool definition. The determined AA2219 creep-ageing constitutive equations were implemented into ABAQUS through the user-defined subroutine CREEP. The springback information was provided at the end of a complete multi-step FE simulation and was then input into the tool offsetting algorithm. The algorithm was designed to evaluate the effective radius ratio, between springback and target isogrid panel. If the error satisfies the specified tolerance, the current tool shape would be used as the final tool surface.

Otherwise, the next tool surface would be reconstructed by decreasing the effective radius of the current tool radius in accordance to the effective radius ratio of springback and current isogrid panel. The geometric information of the new tool surface were redefined in Solidworks and passed back for the next iteration of FE simulation. The integrated numerical procedures were repeated until the specified tolerance was achieved and finally the final surface definition was determined. The detailed explanation of the effective radius of isogrid panel and implementation tool construction algorithm is discussed in a following section. The tool surface definition and tool offset algorithm are carried out manually over each loop.

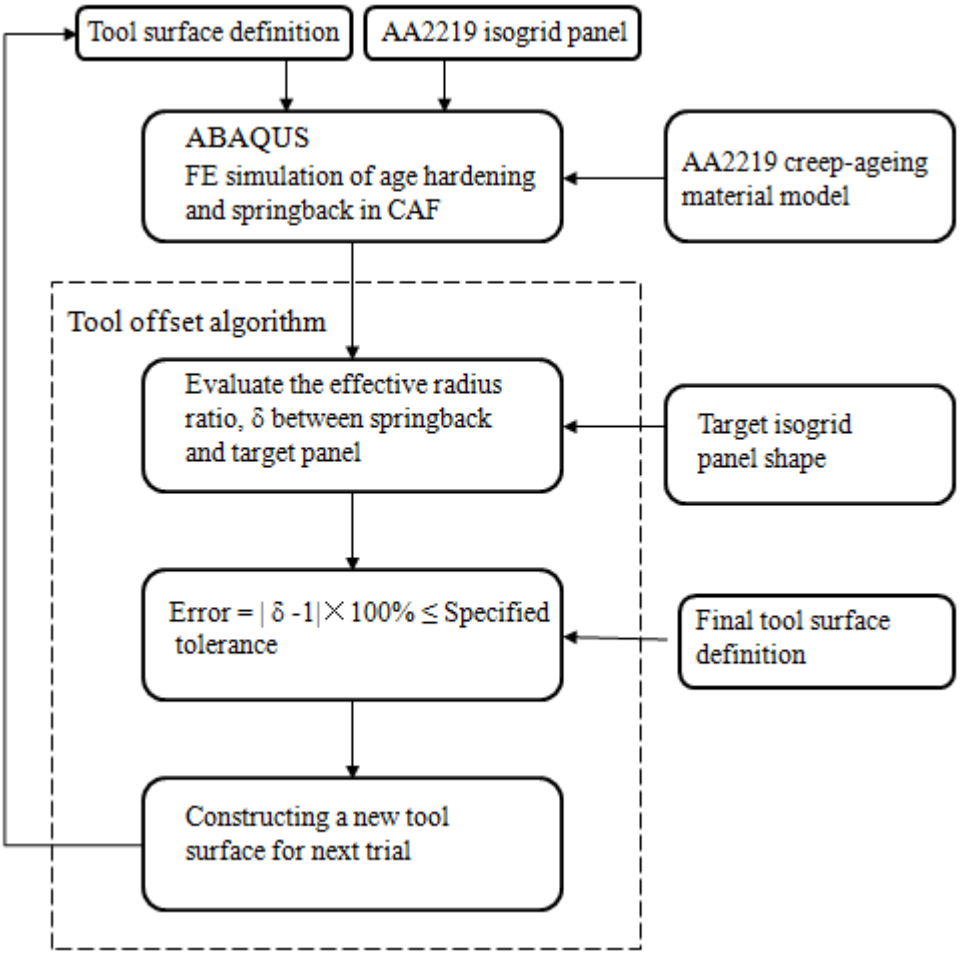


Figure 7.2: Integrated systems to compensate for springback.

## 7.3 Numerical procedures for creep age forming isogrid structures

FE simulations of creep age forming an AA2219 isogrid panel have been carried out using on a series of single-curved die with different effective radius determined by the tool offsetting algorithm. The dimension of the AA2219 panel is shown in Figure 7.3. The total dimension of isogrid panel is 580 mm × 200 mm. The panel thickness at the edge area is 3 mm while the thickness at the isogrid area is 2 mm. The width and the height of the ribs are 4 mm.

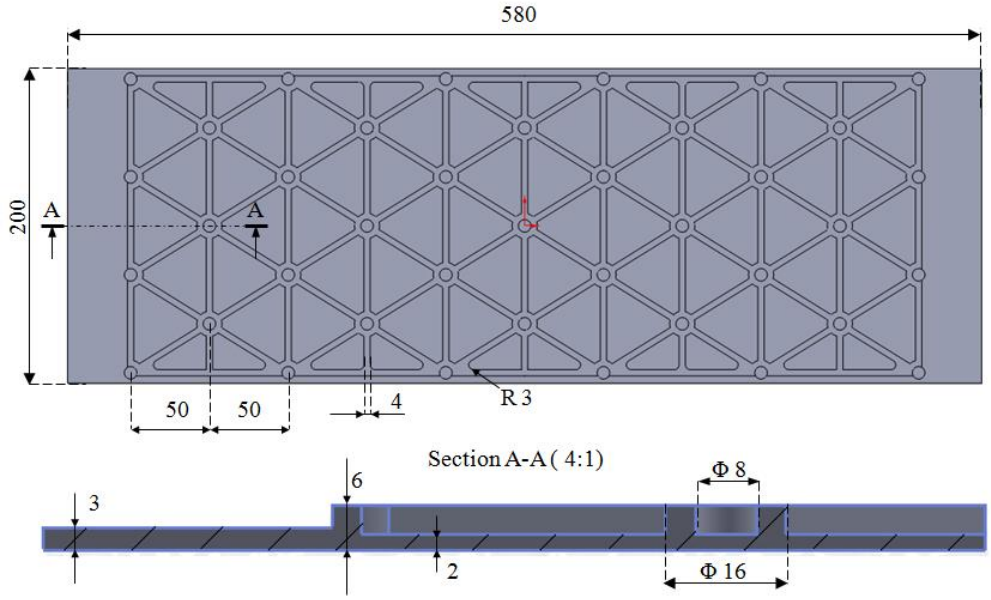


Figure 7.3: AA2219 isogrid workpiece geometry. (all dimensions in mm)

The flat isogrid panel is expected to form a 1/3 circle with a radius of 250 mm. The original isogrid panel is produced by CNC machining in T4 condition and creep age-formed at a constant temperature of 175 ℃ . The CAF simulation consists of locating a quarter isogrid panel against the tool, the surface of which forms the cavity in the shape required. For the convenience of locating the isogrid panel on the tool surface in the forming simulations,

four soft springs, which can be compressed to zero volume, are used to support the weight of the quarter workpiece. Figure 7.4 shows the geometry of the tool and the FE model of the isogrid panel, which would get the required isogrid shape after springback. Both tool surface and isogrid panel were initially constructed in Solidworks. The reduced integration used in this study improves the accuracy of the simulation results, but this has to be weighed up against the cost of computation time [135, 136] .

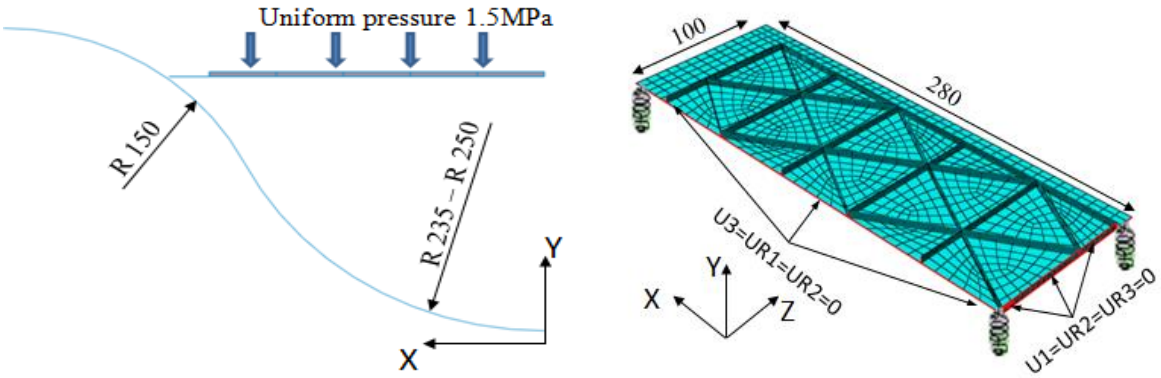


Figure 7.4: Numerical models with loading and boundary conditions on a quarter isogrid structures.

### 7.3.1 Creep-ageing constitutive equations

The creep-induced springback behaviour of AA2219 isogrid structures in a CAF simulation is governed by the physically-based, unified creep-ageing constitutive equations, namely, the AA2219 creep-ageing model. It was implemented into ABAQUS solver via the user-subroutine CREEP. The multi-axial form of the creep constitutive equations for the material model used in CREEP subroutine have been discussed in Chapter 5.

### 7.3.2 Multi-step FE simulation for predicting springback

The FE model, shown in Figure 7.4, consists of a square structure and a rigid spherical tool surface connected by springs. This quarter model has a dimension of 260 mm ×100 mm in length and width. The four-node, quadrilateral, stress/displacement shell elements with reduced integration and a large-strain formulation element S4R, was used for analysis. This rigid tool surface has a radius of 235 mm with a fillet of 150 mm.

Multi-step numerical procedures have been developed to simulate the CAF process and to evaluate the final shape using ABAQUS. The procedures are described below:

STEP 1: Apply a small but sufficient uniform pressure on the top of the isogrid aluminium panel to overcome the stiffness of the springs and guarantee the corner of the panel getting full contact with the tool surface.

STEP 2: Continue to apply uniform pressure to deform the isogrid panel until 95% of the panel completely contact with the tool surface.

STEP 3: Maintain the constant pressure and hold the isogrid panel on the tool surface for a certain period of 18 hours, which allows aging, stress relaxation to take place simultaneously.

STEP 4: Remove the constant pressure incrementally and allow the isogrid to springback. The outside points of the isogrid panel were collected.

### 7.3.3 Definition of effective radius

In Chapter 6, a sensitivity study has been carried out to determine the influence of pressure magnitude on the final shape of the workpiece, it has been found that the localized curvature index along the workpiece are distributed uniformly apart from the edge. Hence, the effective radius area is defined where the workpiece are fully contact with the tool surface during CAF, the outer radius of target workpiece or formed workpiece is termed as an effective radius (Figure 7.5). It is also suggested that the edges of the workpiece should be trimmed off after creep age forming.

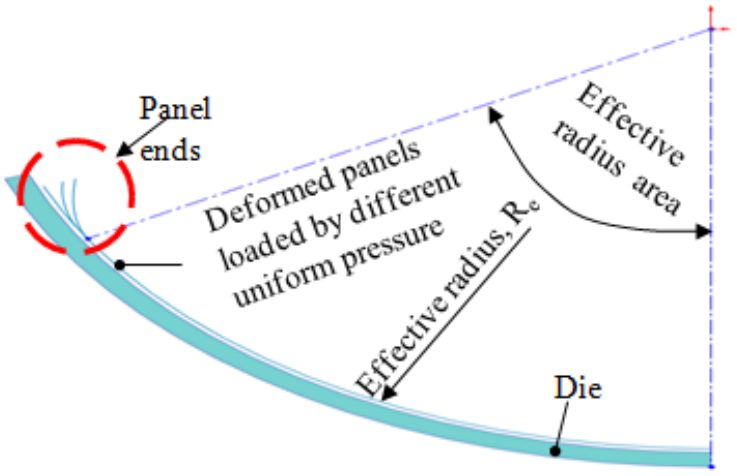


Figure 7.5: Definition of an effective radius.

### 7.3.4 Tool offsetting algorithm

The tool offsetting algorithm includes two steps. This first step is to evaluate the ratio of effective radius between the springback and target isogrid panel. If the calculated error is not within the tolerance, then the second step is applied to modify the radius of the current tool according to the tool offsetting algorithm. Figure 7.6 shows the illustration of offsetting the current tool surface.

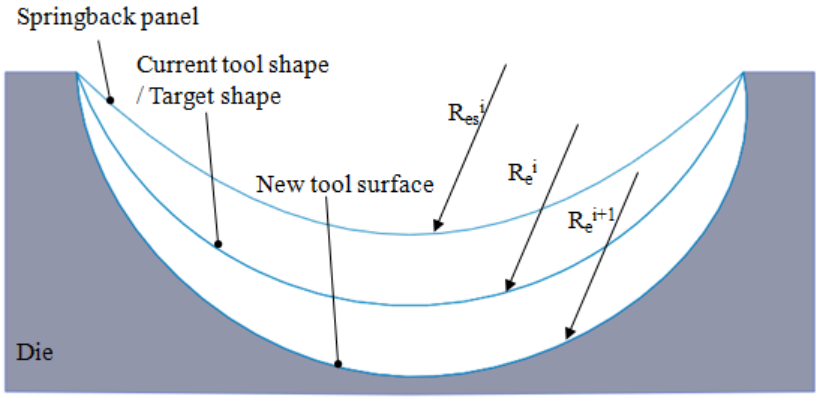


Figure 7.6: Illustration of offsetting a tool surface for springback compensation.

In the first step of the algorithm, the radius of current tool surface, $R_T^i$, the effective radius of target isogrid panel, $R_e^i$, and effective radius of springback isogrid panel, $R_{es}^i$, are provided. $i$ is the number of iteration. For the first iteration, it is assumed that $R_T^1 = R_e^1$. At the end of the FE simulation, the effective radius of the springback panel, $R_{es}^i$, is calculated according to geometric information gained from ABAQUS, and it was then passed into the tool offsetting algorithm. The ratio of effective radius between the springback and target isogrid panel are evaluated by

$$\delta = R_{es}^i / R^i \tag{7.1}$$

If the error, $|\delta - 1|$, is beyond the specified tolerance, the new radius of the tool are formulated in the second step of the algorithm by

$$R_e^{i+1} = R_e^i / \delta \tag{7.2}$$

The re-constructed tool surface are then passed into ABAQUS for next iteration of FE simulation until the error is less than the specified tolerance, and that particular tool surface

will be chosen for the design of the final tool. The tool offsetting algorithm was carried out in Excel-2007 manually to determine the tool surface of next iteration of FE simulation.

## 7.4 Computational results

### 7.4.1 Tool offsetting results

Redesigning of the tool effective radius using the tool offsetting method described above was carried out at the end of each FE numerical simulation. The effective radius of springback was calculated and passed into the algorithm for evaluating the ratio of effective radius between the springback and target isogrid panel. This error deduced from the ratio was then compared to the specified tolerance. The error in the present work was specified as 0.3%. If the error was less than the tolerance, then the current tool radius would be used for designing the final tool. Otherwise, the tool offsetting process would be continued. Figure 7.7 is the result of the error against the iteration. It can be seen that the error decreased significantly during the first three iterations and after that the error started to converge. After total five iterations, the error is 0.21%, which is below the specified tolerance 0.3%. Thus the effective radius (234.7 mm) at iteration 5 will be taken as the final radius for tool design. The final effective radius we applied for final design work is 235 mm for the convenience of the design work.

### 7.4.2 Modelling of stress relaxation and springback

Figure 7.8 shows the simulation results of the creep age forming of an isogrid panel at the $5^{th}$ iteration. This rigid tool surface has a radius of 235 mm with a fillet of 150 mm. The total forming time is 18 hours. Figure 7.8(a) shows the initial loading, where the corner of the isogrid panel has contacted with the tool filter area, at this time, it has already induced plastic deformation at the edge area of the panel. The stress level was lower at the inner of the

isogrid panel. But in terms of the isogrid ribs, the stress level was around 120.73 MPa. Further pressure was applied to deform the whole isogrid panel into the tool shape, shown in Figure 7.8(b). At this stage, the maximum stress level was about 259.1 MPa. However, the stress level is lower in the inner part of isogrid panel. With the isogrid panel held to the tool shape for a further 18 hours, creep took place, which relaxed the stress. The maximum stress at the edge is reduced from 259.1 MPa to approximately 123.3 MPa. While the maximum stress on the illustrated rib decreased from 160.43 MPa to 117.31 MPa. The normal stress level on the outer layer of the isogrid panel is around 120 MPa, as shown in Figure 7.8(c). Springback occurred upon release of the forming pressure since the stresses were not fully released by creep. Figure 7.8(d) shows the residual stress distribution after springback. The majority of the residual stress was less than 102.21 MPa. Due to the requirement on the mechanical property of the isogrid panel after ageing, it is not possible to extend the ageing time, thus the stress could not be relaxed further in the forming process. From the simulation, we can see that the stresses on the isogrid panel nearly reduced to the same stress level after creep ageing forming, which improves the shape stability after unloading.

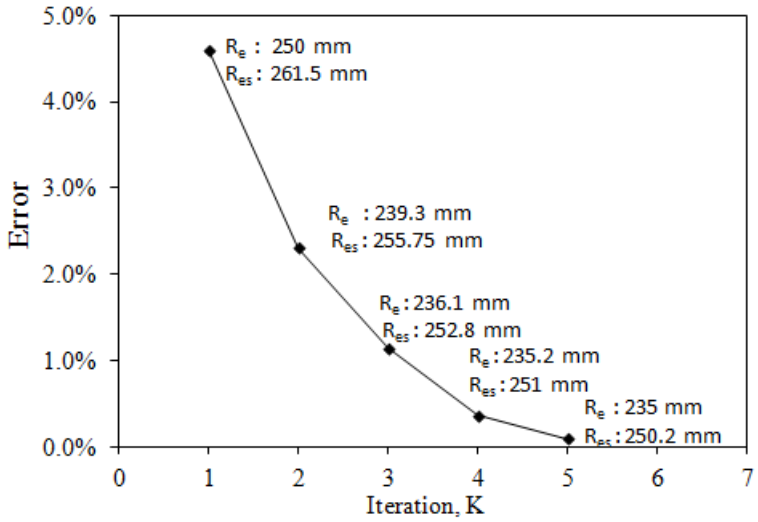


Figure 7.7: Error (difference) in the effective radius between target and springback isogrid panel.

(a) Initial loading

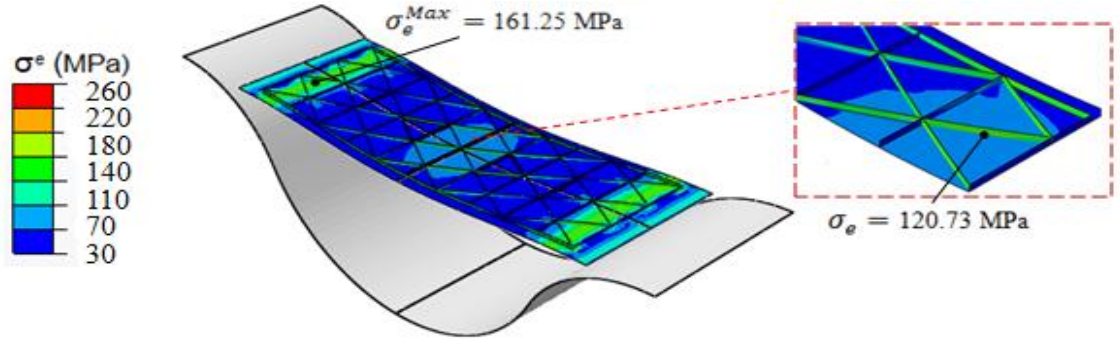


(b) Fully loaded

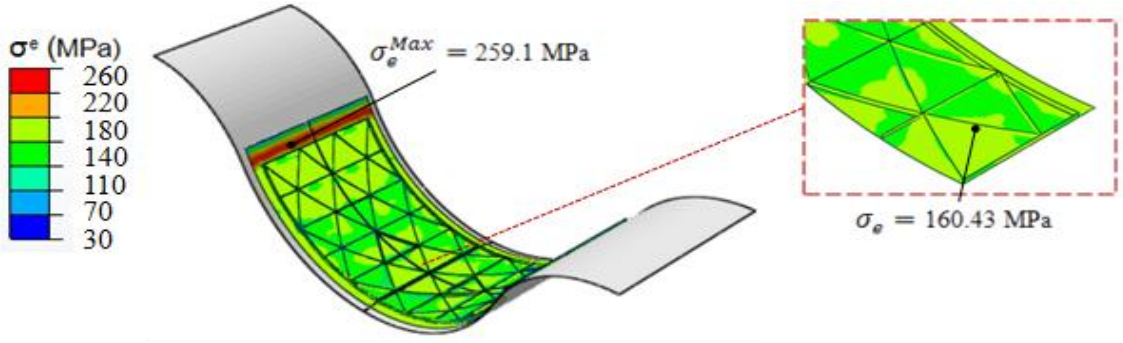


(c) Holding for 18 hours

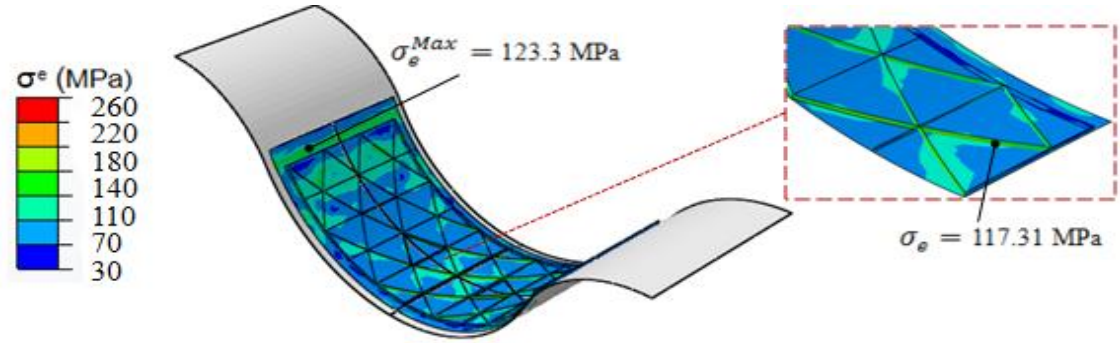


(d) After springback

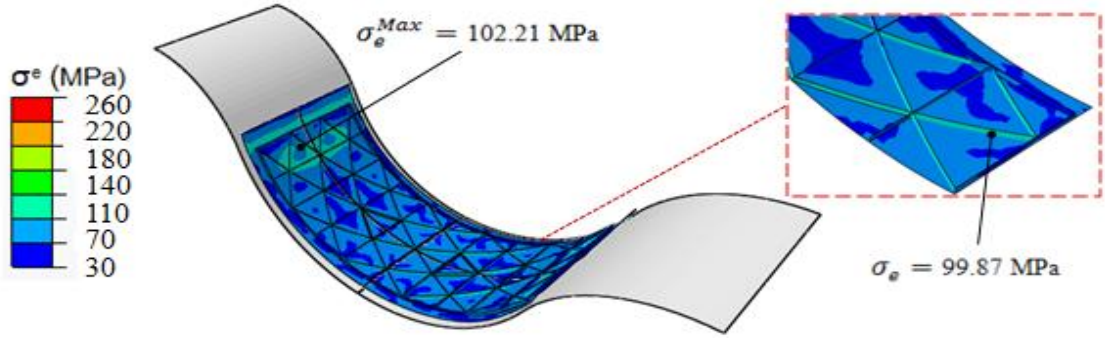


Figure 7.8: Evolution of effective stresses during CAF: (a) at initial loading, (b) fully loaded, (c) hold for 18 hours (d) after springback.

### 7.4.3 Isogrid rib deflection analysis

During the CAF process, one of the major concerns is whether the ribs are stiff enough to resist against buckling induced by vertical deflection in the bending process before artificial ageing. Numerical analysis has also been carried out to investigate the profile of ribs after fully loading. The numerical data was obtained from the top node sets on the ribs at the fully loading stage (Figure 7.9). To comprehensively present the isogrid rib deflection analysis, only a quarter models is illustrated in the numerical analysis. Figure 7.9(a) shows the undeformed isogrid structure while Figure 7.9(b) shows the comparison of computed profile (symbols) and ideal profile (solid lines) of isogrid structure after fully loading. From the simulation result, the maximum deflection is 0.9 mm in vertical direction against the longitudinal direction of ribs. This value is acceptable in isogrid structure design to resist buckling according to the Handbook of Isogrid Design [137]. It is also noted that the autoclave condition enables uniform pressure to be evenly distributed on the top surface of the panel and two sides of the isogrid ribs, thus the vertical deflection of the isogrid ribs is mainly due to the isogrid structure constraints at the intersection.

(a)

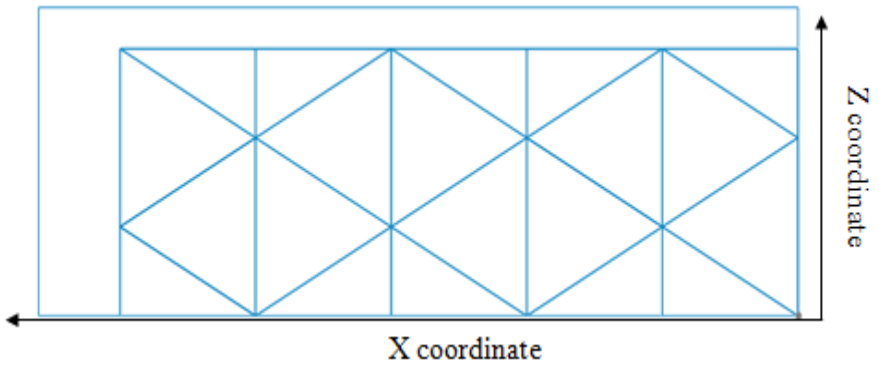


(b)

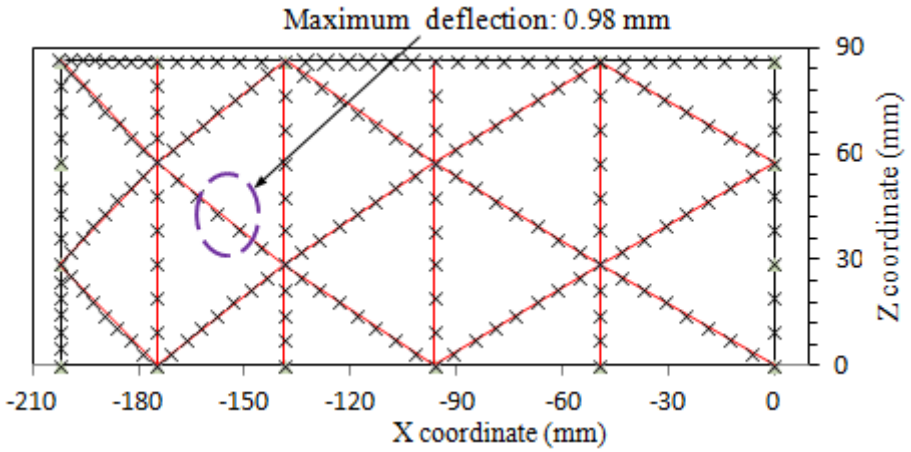


Figure 7.9: (a) Top view of the undeformed isogrid structure (b) Comparison of computed profile (symbols) and ideal profile (solid lines) of isogrid structure at full load.

## 7.5 Autoclave creep age forming of isogrid panels

Autoclave forming of isogrid panels has been basically divided into six stages. In Figure 7.10, a schematic diagram presents the forming stages of CAF for cylindrical isogrid panels. First, the isogrid structures are machined by numerically controlled CNC machining operation on AA2219-T4 flat panels (Figure 7.10(a)). Next, a high temperature vacuum bag is fitted to seal the component against the continuous surface of the forming tool, the air is removed from under the air bag to create an atmospheric pressure differential, forcing the

isogrid panel towards the die surface (Figure 7.10(b)). In the next stages, the pressurised component and tool are loaded into an autoclave while the panel undergoes heat treatment at a temperature of 175 ℃ (Figure 7.10(c)). At the end of the heat treatment cycle (18 hours), the isogrid panel is removed from the autoclave and unwrapped. The edges at the isogrid panel are trimmed thereafter (Figure 7.10(d)). In the last two stages, a cylindrical isogrid panel can be obtained by assembling three pieces of single formed isogrid panels via friction stir welding (Figure 7.10(e)). Excess materials at the lateral edges are machined off (Figure 7.10(f)).

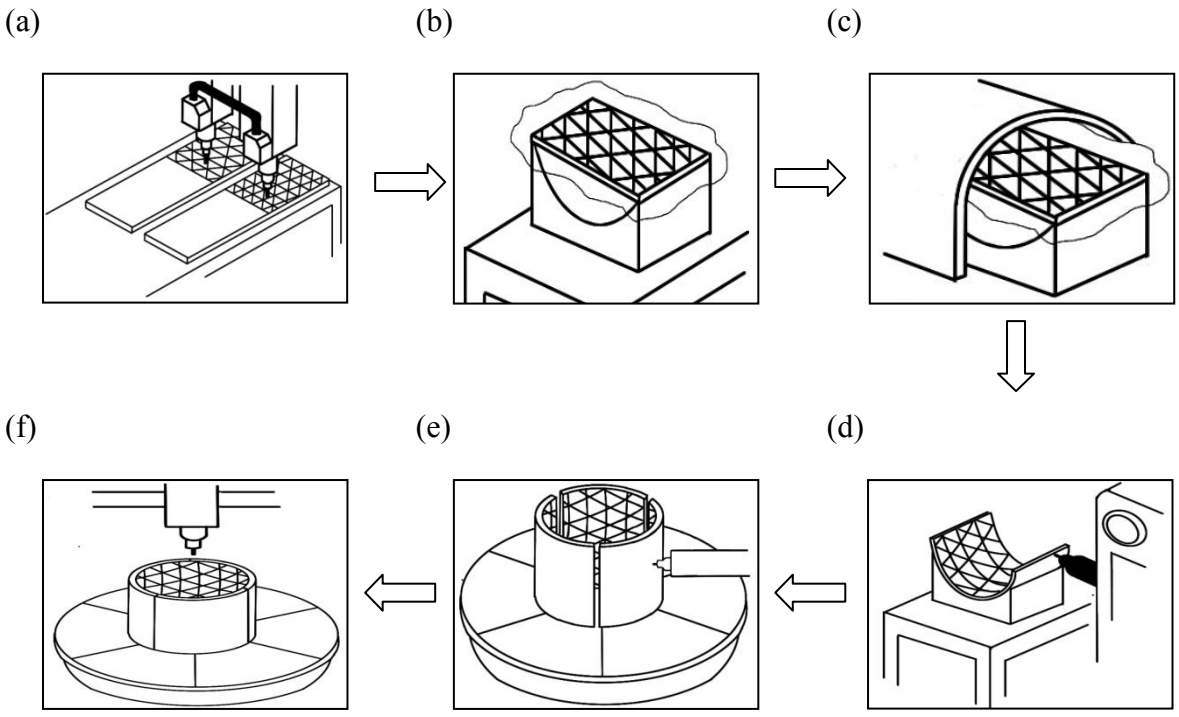


Figure 7.10: A schematic illustration of the CAF process for forming 1/3 pieces isogrid cylindrical assembly by autoclave forming.

## 7.6 Summary

Integrated numerical procedures for predicting stress relaxation and springback and tool shape determination for autoclave creep age forming isogrid panel have been developed. The main interest of this chapter was to establish the FE procedures to simulate the autoclave creep age forming process of forming isogrid panels and predict its consequent springback. The creep ageing behaviour of the material was modelled by implementing the AA2219 creep–ageing constitutive equation into the ABAQUS though CREEP subroutine for the CAF simulations. The integrated numerical procedures with the tool offsetting algorithm were carried out repeatedly until the specified tolerance was achieved and finally the final surface definition was determined. The convergence of tool offsetting results demonstrates that the iterative integrated procedures can be used to determine the final tool shape based on FE simulation results. Also, the numerical results show that the established FE procedures enables the stress relaxation, springback behaviour and the deflection of isogrid ribs to be predicted in CAF. Finally, a proposed CAF process for forming 1/3 pieces isogrid cylindrical assembly by autoclave forming has been given for the guidance of industrial usage.

# CHAPTER 8

# Experimental Investigation on Forming AA2219 Stiffened Structures

## 8.1 Introduction

As discussed in Chapter 7, besides autoclave creep age forming, upper-lower die set (mechanical forming) can also be employed for creep age forming large panel structures. In this chapter, an end clamp device was designed and used to creep age form a stiffened panel structure. The experiment consisted of three stages: in the first stage, an end clamp device, capable of generating a constant radius profile, was employed to deflect the specimen into the expected shape. In this stage, PTFE filler material was used to fill the machined-out pockets in the panel to avoid the contact force being compressed directly on the ribs. In the second stage, the compressed specimen, together with the end clamp device, was put into a closed furnace at 175 ℃ for duration of up to 18 hours. In the last stage, after the end clamp device was cooled down to the room temperature, the upper die device was removed and the specimen sprung back. The main objective of the experiment was to investigate the feasibility of creep age forming stiffened structures by a mechanical method (i.e. using an upper-lower die set).

## 8.2 Experimental Characterization

### 8.2.1 End clamp device design

Figure 8.1 shows the schematic configuration of the end clamp device. The test device was designed by the author and manufactured by three DMT students in the Mechanical Engineering Department at Imperial College London. The end clamp device consisted of a cylindrical die (top part) and two clamps at the bottom (bottom part). The detailed dimensions of the device are shown in the figure below.

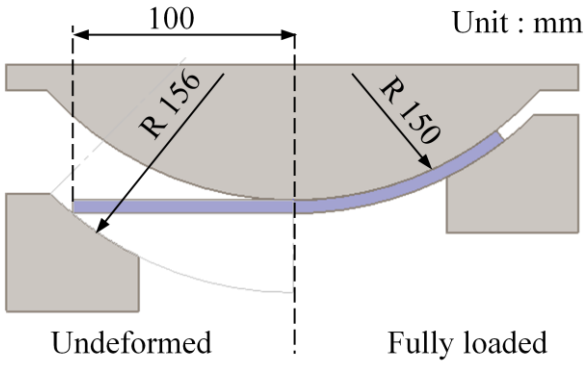


Figure 8.1: Schematic illustration of the end clamp experiment. (all dimensions in mm)

### 8.2.2 Test specimen preparation

The specimens were machined into three types of stiffened structures from 6 mm base 2219-T87 base plates: one stiffened panel, a rectangular stiffened panel and an isogrid stiffened panel. A flat 4.5 mm thick panel was also employed in the experiment. All the specimens were solution heat-treated and water quenched prior to the test. The dimensions of the four types of workpiece are shown in Figure 8.2.

(a) Flat panel

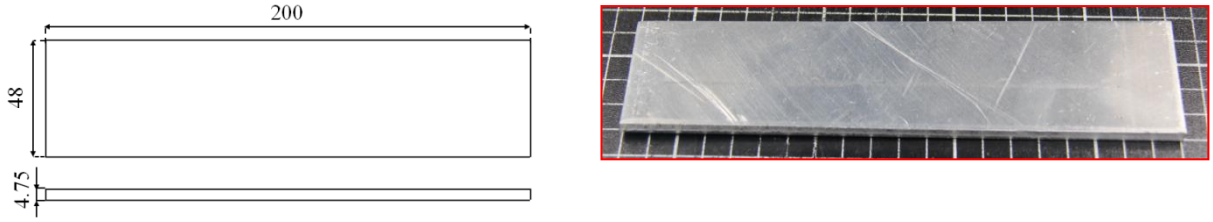


(b) One stiffened panel

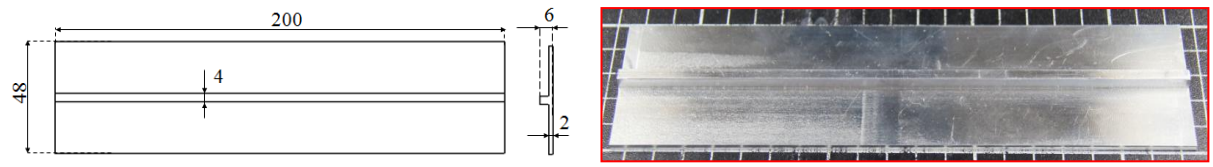


(c) Rectangular stiffened panel

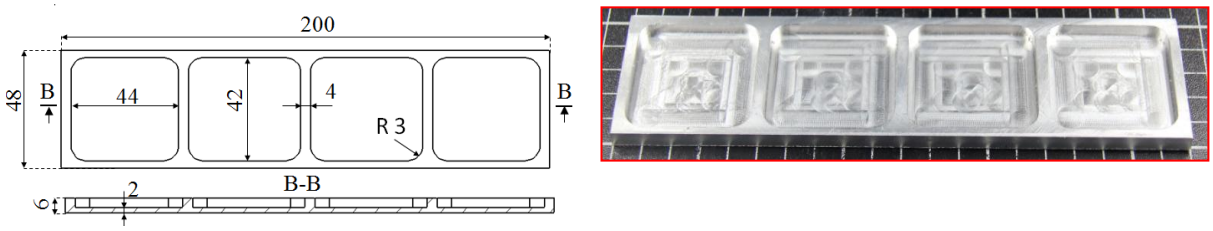


(d) Isogrid stiffened panel

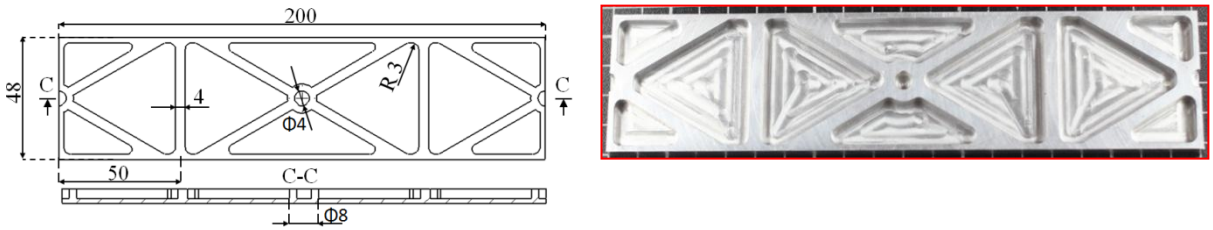


Figure 8.2: Illustration of the stiffened panels. (all dimensions in mm)

### 8.2.3 Experimental procedures

The experiments were performed by the author and three DMT students together. The experimental procedures are listed below:

- The initial workpiece was placed, centred, and properly aligned on the two clamps. Some markings were used to assist the alignment. 6 mm thick trimmed PTFE filler material ( $E: 750$ MPa, $\sigma_{0.2}: 12$ MPa [138]) was used to fill the machined-out pockets of the

stiffened panels. Another 6 mm thick plane PTFE material was placed on the top surface of the trimmed PTFE filler material to transfer the compression force. (Figure 8.3 (a))

- The cylindrical die was installed on the Lloyd 5588 material testing machine (as discussed in Chapter 5, Section 5.2.2); the displacement control model was used. Both the cross head speed and displacement were pre-set.
- The cylindrical die was lowered using a sensitive control until the 6 mm thick plane PTFE started to transfer the compression force onto the tested workpiece; an obvious positive loading change was the indicator used to confirm that the compression force was beginning to be transferred. (Figure 8.3 (b))
- The displacement and load indicator was then zeroed. The cross head was allowed to travel down at a constant speed so as to press down the cylindrical die and consequently compress the workpiece to the target displacement, i.e. by 38 mm in all the stiffened panels. (Figure 8.3 (c))
- Once the target distance was achieved, the cross head was stopped. Four locking bolts were applied to tighten the end clamp device in order to hold the workpiece in place. A value of around zero displayed on the indicator was taken to mean that the end clamp device was fully tightened. (Figure 8.3 (d))
- The end clamp device was then removed from the Lloyds 5588 material testing machine and the entire end clamp device associated with the compressed workpiece was put into a closed fan furnace. (Figure 8.3 (e))
- The temperature of the furnace was kept constant at 175 ℃ for 18 hours to allow age hardening and stress relaxation to take place.
- After 18 hours, the furnace was opened. The entire rig together with the held, deformed, workpiece was removed from the furnace.

- After cooling to room temperature (up to 3 hours), the locking bolts were removed from the end clamp device. The workpiece was then allowed to springback. (Figure 8.3 (f))

As well as forming these CAF workpieces, parallel experiments were also carried out to form CWBSFA workpieces, in a similar experiment to that conducted in Chapter 5.

(a) (b)

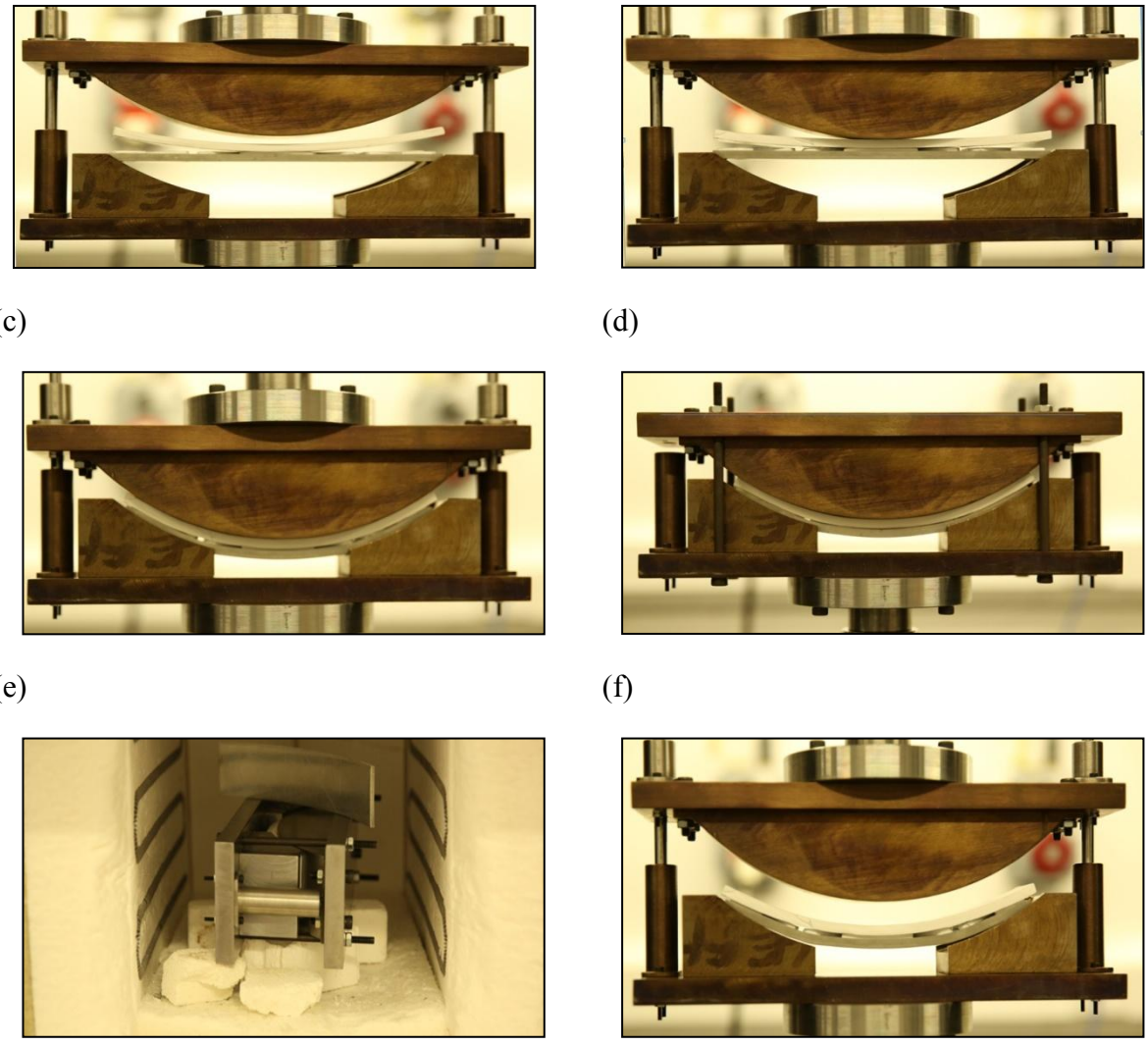

(c) (d)

(e) (f)

Figure 8.3: Pictorial illustrations of the experimental procedures.

## 8.3 Experimental Results

Several CAF tests were carried out using the procedures discussed in Section 8.2. Figure 8.4 shows the deformed workpieces together with the filler materials that were removed from

the machined-out pockets. The average thickness of the PTFE filler material was found to have decreased from 6.00 mm to 5.21 mm. These PTFE filler materials were used several times to form the same structure stiffened panel. After a total of four uses of the PTFE filler, the final average thickness of these materials was around 4.93 mm.

(a) Flat panel

(b) One stiffened panel

(c) Rectangular stiffened panel

(d) Isogrid stiffened panel

Figure 8.4: Deformed stiffened panels with filler materials after creep age forming.

- Figure 8.5 shows a visual profile and a plotted comparison of the CAF and CWBSFA workpieces. The outer profile of the half-deformed workpiece was plotted on coordinate paper. In Figure 8.5, REF, which equals 156 mm, refers to the outer profile of the deformed workpiece without springback.

(i) (ii)

(a) Flat Panel

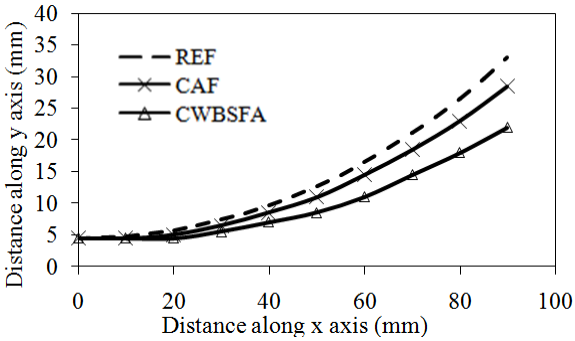


(b) One stiffened panel

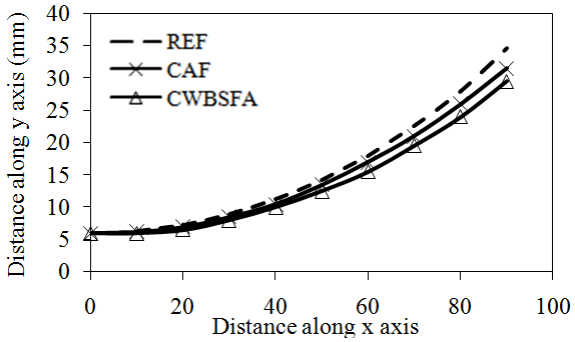


(c) Rectangular stiffened panel

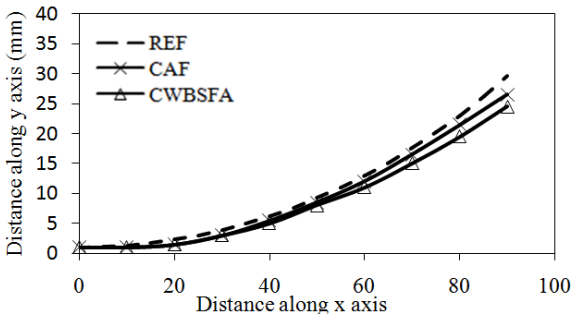


(d) Isogrid stiffened panel

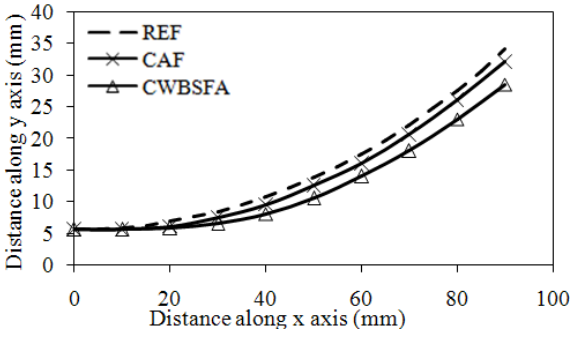


Figure 8.5: Illustration of (i) the visual profile and (ii) comparison of the profile between CAF and CWBSFA workpieces.

From Figure 8.5, stiffened workpiece with curvilinear profiles could be obtained. Due to the experiments are carried out by an end clamp device, it would not be cylindrical profiles. But it still proves that a stiffened workpiece with a curvilinear profile could be obtained using a mechanical creep age forming method with the application of PTFE material filling in the machined-out pockets. Also, from the observations, there are no obvious irregular skins and failure ribs due to buckling. The PTFE material will be therefore suggested to be applied in the future mechanical CAF work. Also, by performing the same compression procedures, the springback experienced by the CAF workpieces was less than that for the CWBSFA workpieces as expected.

## 8.4 Mechanical creep age forming of isogrid panels

Figure 8.6 represents the mechanical-based CAF manufacturing sequences involved in producing cylindrical isogrid structures.

Firstly, the CNC machining operation is conducted on an AA2219-T4 isogrid panel (Figure 8.6(a)). When the section being machined has been completed, it is filled with PTFE material, which is able to deform with the isogrid panel up to a temperature of 260 °C (Figure 8.6(b)). Next, the isogrid panel filled with PTFE material is compressed to the desired curvature using a compression die tool. Once the panel is in full contact with the lower die, the upper die is stopped and locked into position using bolts (Figure 8.6(c)). Thereafter, the entire system is put into a closed fan furnace at a temperature of 175 ℃ . After 18 hours, the entire system is removed from the furnace and cooling takes place. After the system has cooled down to room temperature, the upper die is removed and a curved isogrid panel is obtained (Figure 8.6(d)). The filler material can then be removed from the isogrid panel and

the leading and trailing edges of the panel are trimmed (Figure 8.6(e)). Finally, a cylindrical structure can be obtained by assembling three pieces of single formed isogrid panels via friction stir welding (Figure 8.6(f)). Excess materials at the lateral edges are machined off (Figure 8.6(g))

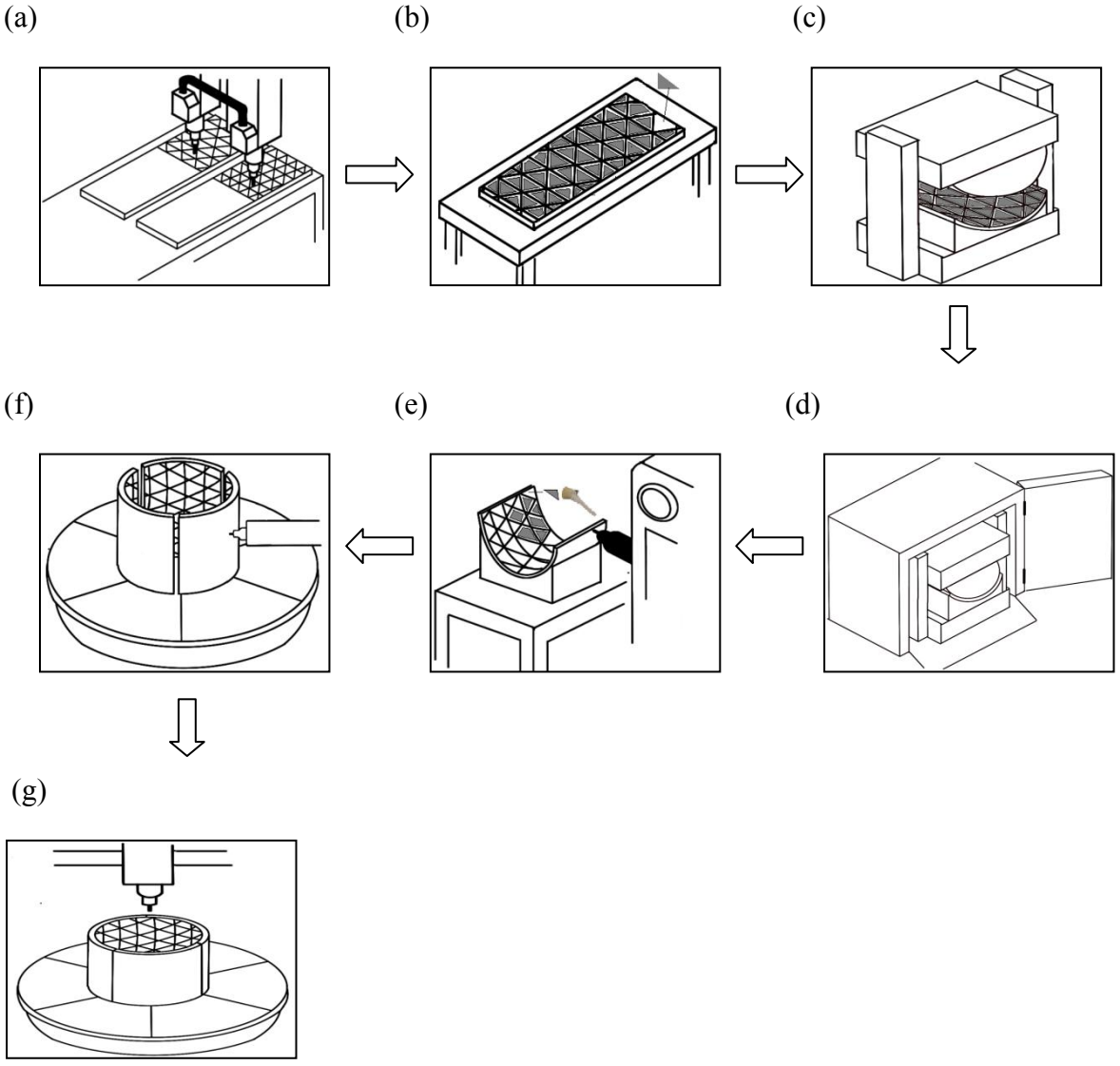


Figure 8.6: A schematic illustration of the CAF process for forming 1/3 pieces for isogrid cylindrical assembly by bending and forming.

## 8.5 Summary

In the experiment described in this chapter, an end clamp device was employed to investigate creep age forming of stiffened structures using a mechanical forming method. Generally, the experimental results show that mechanical creep age forming of stiffened structures with PTFE filler material enables the formation of curvilinear stiffened structures. In addition, comparison between stiffened panels formed using CAF and CWBSFA showed that the creep age forming technique resulted in less springback than in the CWBSFA panels, thereby providing improved formability. Finally, as a guide for usage of this process in an industrial context, the chapter outlines a proposed CAF process for forming 1/3 pieces for an isogrid cylindrical assembly using mechanical forming with PTFE filler material.

# CHAPTER 9

# Conclusions and Suggestions for Future Research

## 9.1 Conclusions

The study of creep age forming (CAF) of aluminium alloy 2219 and application of modelling techniques for predicting age-hardening, stress relaxation and springback in CAF have been presented in this thesis. The key conclusions of this research have been drawn into the following aspects:

- Due to limitations of the industrial artificial ageing temperature and the forming time dictated by microstructure requirements, it is not possible to fully relax the stresses in the AA2219 aluminium structure. Therefore, springback is unavoidable in CAF. When the stress level drops due to creep, the creep rate reduces sharply according to sinh-law relation. The creep deformation is subsequently in the stage of steady state and so as the stress relaxation. These stresses are expected to relax to a similar level at a critical load at the end of artificial ageing.
- Constitutive modelling methods have been applied and adopted to model both physical and mechanical properties of the AA2219 in CAF at 175 ℃ . FE numerical simulation procedures for CAF AA2219 sheet structure have been established using commercial FE solver ABAQUS via user-defined subroutine, CREEP. The FE simulation results demonstrated that, apart from modelling the creep deformation, stress relaxation behaviour of the material and its consequent springback, the microstructure evolution of normalized mean ratio of disc-shape precipitates and yield strength of the material during CAF can also be predicated.

- Four point bend experiments were designed and carried out to characterize the springback behaviour and validate the springback prediction of the AA2219 sheet components. The experimental result and simulation are in good agreement with errors less 15%. The simulated results might be improved if the thermal stress effect during the heating process is considered in the simulation.
- Numerical models have been established to analyse the difference in springback predictions between the two loading cases: end clamp and autoclave. The former is often used in small scale laboratory testing and the latter in real industrial forming processes. It is recommended that for a large scale component the springback evaluated from end clamping could not be used for assessing the springback from autoclave condition. It is recommended that laboratory scale end clamping tests should not be used to model springback features for the real vacuum forming processes as the local springback distributions are significantly different, even if the overall magnitudes are similar.
- Integrated numerical procedures for predicting stress relaxation and springback and tool shape determination for autoclave creep age forming isogrid panel have been developed. A tool offsetting algorithm is established based on the CAF simulation results of 1/3 pieces isogrid cylindrical structures. By employing the algorithm, the desired tool shape with good accuracy can be found in 5 integrations.
- Experimental work has been carried out to investigate mechanical-based creep age forming stiffened structure. The investigation indicates mechanical-based CAF of stiffened structures with PTFE filler material enables to form curvilinear stiffened structures without passing the compression force directly onto the stiffened ribs.

## 9.2 Suggested Future Work

The present research is the preliminary work to model the CAF features of aluminium alloy 2219 and investigation of the related forming work for CAF AA2219 isogrid structures. There are some areas required further investigation and following are suggestions:

- Microstructure examination on the evolution of ageing precipitates is expected to be performed to improve the understanding of the material during CAF.
- A detailed research of thermal stress analysis needs to be carried out to understand and investigate the thermal stress effect on the loading stage of CAF.
- A CAF equipment should be designed for forming 1/3 pieces isogrid cylindrical structure to further validate the FE simulation and seek the novel CAF process for forming isogrid structure in the industrial application.
- Exploration of new forming process for forming isogrid fuel tank will be carried out based on the well understanding of CAF process. One piece cylindrical isogrid structures are expected to be fabricated in the future by CAF to reduce piece-part count. A preliminary idea of creep age forming one-piece cylindrical isogrid structure is shown in Figure 9.1.

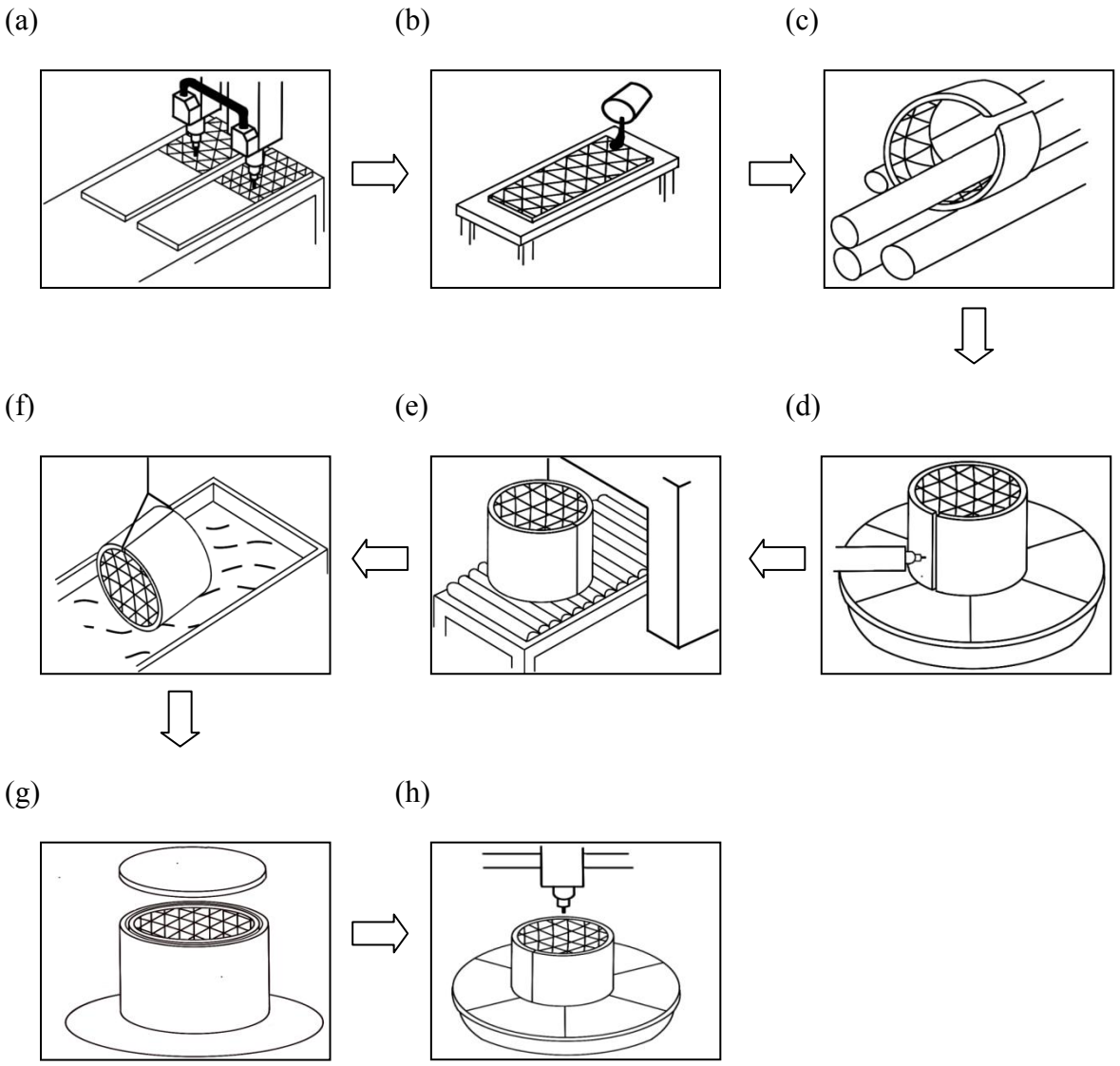


Figure 9.1: A schematic illustration of the CAF process for forming one piece isogrid cylindrical assembly by hydro forming.

During this novel process, the isogrid structures are expected to be machined on AA2219-T4 flat panels (Figure 9.1(a)). Next, the machined isogrid panel is rolled as a whole cylindrical body after the machined-out pockets filled with a low melting wax (Figure 9.1 (b) and (c)). After the rolling process, two ends of the rolling part are expected to be welded together via friction stir weldment (Figure 9.1(d)). Next, the wax is melted out at 60 ℃ and the isogrid panel is cleaned in the water tank (Figure 9.1 (e) and (f)). Then the

whole cylindrical isogrid body are sent into a hydro tank to allow hydro expanding and artificial ageing taken place synchronously in the forming process (Figure 9.1 (g)). Finally, excess materials at the lateral edges are machined off (Figure 9.1 (h)).

# Reference


1. Braun, R.D., A.A. Moore, and I.M. Kroo, *Collaborative approach to launch vehicle design.* Journal of Spacecraft and Rockets, 1997. **34**(4): p. 478-486.
2. Chan, A.L., et al., *Payload housing and assembly joint for a launch vehicle*, 1998, Google Patents.
3. Thomas, G.R., C.M. Fadick, and B.J. Fram. *Launch vehicle payload adapter design with vibration isolation features*. in *Smart Structures and Materials*. 2005. International Society for Optics and Photonics.
4. Wertz, J.R. *Economic model of reusable vs. expendable launch vehicles*. in *IAF, International Astronautical Congress, 51 st, Rio de Janeiro, Brazil*. 2000.
5. Hanson, J. *Advanced guidance and control project for reusable launch vehicles*. in *AIAA Guidance, Navigation, and Control Conference and Exhibit*. 2000.
6. Hanson, J.M., *A plan for advanced guidance and control technology for 2nd generation reusable launch vehicles.* AIAA paper, 2002. **4557**.
7. Wertz, J.R., R. Conger, and J. Kulpa. *Responsive Launch With the Scorpius Family of Low-Cost Expendable Launch Vehicles*. in *AIAA 1st Responsive Space Conference*. 2003.
8. Behrens, C.E., *Space Launch Vehicles: Government Activities, Commercial Competition, and Satellite Exports.* Space Policy and Exploration, 2008: p. 39.
9. Isakowitz, S.J., J.P. Hopkins, and J.B. Hopkins, *International reference guide to space launch systems*. 1999: American Institute of Aeronautics and Astronautics.
10. Oh, D., et al., *Deep Space Mission applications for NEXT: NASA's evolutionary xenon thruster*. 2004: Pasadena, CA: Jet Propulsion Laboratory, National Aeronautics and Space Administration.
11. Jia, Y., *A Series of Chang-Zheng Rockets' Space Launch Number of Times Amount to 100 by the Thirteenth of September 2006 [J]*. Spacecraft Recovery & Remote Sensing, 2006. **4**: p. 000.
12. Smith, M.S. *China's Space Program: An Overview*. 2005. DTIC Document.
13. EUROPEAN-SPACE-AGENCY, *Available from: http://www.esa.int/ESA*. 2006.
14. He, S., *China's moon project change: Stratagem and prospects.* Advances in Space Research, 2003. **31**(11): p. 2353-2358.
15. Xuhui, Z., *Telemetry Simulation System of LM-2F Launch Vehicle [J]*. Missiles and Space Vehicles, 2004. **1**: p. 005.
16. China-Aerospace-Corporation, *Available from: http://www.cgwic.com/LaunchServices/LaunchVehicle/LM2F.html* 2005.
17. Olds, L., *Integration of cost modeling and business simulation into conceptual launch vehicle design.* Paper No. AIAA, 1997: p. 97-3911.
18. Larson, W.J. and L.K. Pranke, *Human spaceflight: mission analysis and design*. 2000: McGraw-Hill Companies.
19. Huybrechts, S. and T.E. Meink. *Advanced grid stiffened structures for the next generation of launch vehicles*. in *Aerospace Conference, 1997. Proceedings., IEEE*. 1997. IEEE.
20. Díaz, V., E. del Olmo, and M. Frövel. *Design & development of advanced composite isogrid structural solutions for primary structures of future reusable launch vehicle*.

in *proceedings ECSSMMT, 11th European Conference on Spacecraft Structures, Materials and Mechanical Testing, Toulouse, France*. 2009.
21. Glass, D.E. and H. Belvin. *Airframe technology development for next generation launch vehicles*. in *Prepared for the 55thInternationalAstronautical Congress, Vancouver, Canada*. 2004.
22. Hilburger, M.W., et al., *Design and Analysis of Subscale and Full-Scale Buckling-Critical Cylinders for Launch Vehicle Technology Development.* 2012.
23. Masubuchi, K., *Integration of NASA-sponsored studies on aluminum welding.* 1972.
24. Narayana, G.V., et al., *Fracture behaviour of aluminium alloy 2219–T87 welded plates.* Science and Technology of Welding & Joining, 2004. **9**(2): p. 121-130.
25. Polmear, I., *Recent developments in light alloys.* JIM, Materials Transactions, 1996. **37**(1): p. 12-31.
26. Vasiliev, V., V. Barynin, and A. Rasin, *Anisogrid lattice structures–survey of development and application.* Composite structures, 2001. **54**(2): p. 361-370.
27. Meyer, R., O. Harwood, and J. Orlando, *Isogrid design handbook.* 1973.
28. Heinz, A., et al., *Recent development in aluminium alloys for aerospace applications.* Materials Science and Engineering: A, 2000. **280**(1): p. 102-107.
29. Munroe, J., K. Wilkins, and M. Gruber, *Integral Airframe Structures (IAS)---Validated Feasibility Study of Integrally Stiffened Metallic Fuselage Panels for Reducing Manufacturing Costs.* 2000.
30. Pettit, R., J. Wang, and C. Toh, *Validated feasibility study of integrally stiffened metallic fuselage panels for reducing manufacturing costs*. 2000: National Aeronautics and Space Administration, Langley Research Center.
31. Elangovan, K. and V. Balasubramanian, *Influences of pin profile and rotational speed of the tool on the formation of friction stir processing zone in AA2219 aluminium alloy.* Materials Science and Engineering: A, 2007. **459**(1): p. 7-18.
32. Elangovan, K. and V. Balasubramanian, *Influences of tool pin profile and welding speed on the formation of friction stir processing zone in AA2219 aluminium alloy.* Journal of materials processing technology, 2008. **200**(1): p. 163-175.
33. Surekha, K., B. Murty, and K. Prasad Rao, *Effect of processing parameters on the corrosion behaviour of friction stir processed AA 2219 aluminum alloy.* Solid state sciences, 2009. **11**(4): p. 907-917.
34. Kleiner, M., S. Chatti, and A. Klaus, *Metal forming techniques for lightweight construction.* Journal of materials processing technology, 2006. **177**(1): p. 2-7.
35. Jeswiet, J., et al., *Metal forming progress since 2000.* CIRP Journal of manufacturing Science and technology, 2008. **1**(1): p. 2-17.
36. Marré, M., et al., *Manufacturing of lightweight frame structures by innovative joining by forming processes.* International Journal of Material Forming, 2009. **2**(1): p. 307-310.
37. Holman, M.C., *Autoclave age forming large aluminum aircraft panels.* Journal of Mechanical Working Technology, 1989. **20**: p. 477-488.
38. Schmoeckel, D. and M. Beth, *Springback reduction in draw-bending process of sheet metals.* CIRP Annals-Manufacturing Technology, 1993. **42**(1): p. 339-342.
39. Mitra, R., *Process for stretch forming age-hardened aluminum alloy sheets*, 2000, Google Patents.
40. Yuansong, Z. and H. Xia, *Forming technologies of large integral panel [J]*. Acta Aeronautica Et Astronautica Sinica, 2008. **3**: p. 037.

41. Miao, H., et al., *Experimental study of shot peening and stress peen forming.* Journal of Materials Processing Technology, 2010. **210**(15): p. 2089-2102.
42. Yu, W.-W. and R.A. LaBoube, *Cold-formed steel design*. 2010: Wiley.
43. Zhan, L., J. Lin, and T. Dean, *A review of the development of creep age forming: Experimentation, modelling and applications.* International Journal of Machine Tools and Manufacture, 2011. **51**(1): p. 1-17.
44. Bakavos, D., P. Prangnell, and R. Dif. *A Comparison of the Effects of Age forming on the Precipitation Behavior in 2 xxx, 6 xxx and 7 xxx Aerospace Alloys*. in *Materials Forum*. 2004.
45. Robey, R., P. Prangnell, and R. Dif. *A Comparison of the Stress Relaxation Behavior of Three Aluminium Aerospace Alloys for use in Age-Forming Applications*. in *Materials Forum*. 2004.
46. Peery, D.J., *Aircraft structures*. 2011: Courier Dover Publications.
47. Watcham, K., *Airbus A380 takes creep age-forming to new heights.* Materials World, 2004. **12**(2): p. 10-11.
48. Eberl, F., et al., *Ageformable panels for commercial aircraft.* Proceedings of the Institution of Mechanical Engineers, Part G: Journal of Aerospace Engineering, 2008. **222**(6): p. 873-886.
49. Xue, P., T. Yu, and E. Chu, *An energy approach for predicting springback of metal sheets after double-curvature forming, Part I: axisymmetric stamping.* International journal of mechanical sciences, 2001. **43**(8): p. 1893-1914.
50. Mavromihales, M., J. Mason, and W. Weston, *A case of reverse engineering for the manufacture of wide chord fan blades (WCFB) used in Rolls Royce aero engines.* Journal of materials processing technology, 2003. **134**(3): p. 279-286.
51. GNK-AEROSPACE, *Available from http://www.gkn.com/aerospace/products-and-capabilities/capabilities/metallics/advance-creep-forming/Pages/default.aspx 2009.*
52. Ribeiro, F., et al., *Creep age forming: a short review of fundaments and applications.* Journal Achievements in Mechanics, Manufacturing and Materials Science, 2010. **43**: p. 353-361.
53. Zhan, L., J. Lin, and M. Huang. *Constitutive Modelling and Springback Prediction in Creep Age Forming of AA7055 Doubly Curved Panels*. in *AIP Conference Proceedings*. 2011.
54. Ho, K., J. Lin, and T. Dean, *Constitutive modelling of primary creep for age forming an aluminium alloy.* Journal of Materials Processing Technology, 2004. **153**: p. 122-127.
55. Ho, K., J. Lin, and T. Dean, *Modelling of springback in creep forming thick aluminum sheets.* International Journal of Plasticity, 2004. **20**(4): p. 733-751.
56. Jeunechamps, P.-P., et al., *A closed form technique to predict springback in creep age-forming.* International Journal of Mechanical Sciences, 2006. **48**(6): p. 621-629.
57. Lin, J., K. Ho, and T. Dean, *An integrated process for modelling of precipitation hardening and springback in creep age-forming.* International Journal of Machine Tools and Manufacture, 2006. **46**(11): p. 1266-1270.
58. LI, J., et al., *Age Forming of Al Alloys and Ageformable Al Alloys.* Materials Review, 2006. **5**: p. 029.
59. Pitcher, P. and C. Styles. *Creep age forming of 2024A, 8090 and 7449 alloys*. in *Materials science forum*. 2000. Trans Tech Publ.
60. GAN, Z., et al., *Mold design for age forming of integral skin-panel.* Ordnance Material Science and Engineering, 2011. **4**: p. 026.

61. Gan, Z., J.Z. Zhu, and L. Zhang, *Research on Springback Compensation in Age Forming Technology of Integral Panel.* Advanced Materials Research, 2011. **304**: p. 90-95.
62. Zhan, L., et al., *Experimental studies and constitutive modelling of the hardening of aluminium alloy 7055 under creep age forming conditions.* International Journal of Mechanical Sciences, 2011. **53**(8): p. 595-605.
63. Gan, Z., et al., *Structure of Mold Surface for Stress Relaxation Forming of Integral Panel of 2124 Aluminum Alloy.* Applied Mechanics and Materials, 2012. **152**: p. 140-144.
64. Gangloff, R.P., et al., *Fatigue crack propagation in aerospace aluminum alloys.* Journal of aircraft, 1994. **31**(3): p. 720-729.
65. Jambu, S., et al., *Creep forming of AlMgSc alloys for aeronautic and space applications.* ICAS 2002, 2002.
66. JAMBU, S., K. JUHL, and B. LENCZOWSKI, *METHOD FOR SHAPING STRUCTURES COMPRISED OF ALUMINUM ALLOYS*, 2002, WO Patent 2,002,026,414.
67. Starke, E. and J. Staley, *Application of modern aluminum alloys to aircraft.* Progress in Aerospace Sciences, 1996. **32**(2): p. 131-172.
68. Zhu, A. and E. Starke Jr, *Materials aspects of age-forming of Al–< i> x</i> Cu alloys.* Journal of materials processing technology, 2001. **117**(3): p. 354-358.
69. Starink, M.J., et al. *Development of new damage tolerant alloys for age-forming*. in *Materials Science Forum*. 2002. Trans Tech Publ.
70. Arabi Jeshvaghani, R., et al., *Effects of time and temperature on the creep forming of 7075 aluminum alloy: Springback and mechanical properties.* Materials Science and Engineering: A, 2011. **528**(29): p. 8795-8799.
71. Arabi Jeshvaghani, R., et al., *Influence of multi-step heat treatments in creep age forming of 7075 aluminum alloy: Optimization for springback, strength and exfoliation corrosion.* Materials Characterization, 2012.
72. Lin, Y., et al., *Precipitation hardening of 2024-T3 aluminum alloy during creep aging.* Materials Science and Engineering: A, 2012.
73. Lin, Y., et al., *Constitutive descriptions for hot compressed 2124-T851 aluminum alloy over a wide range of temperature and strain rate.* Computational Materials Science, 2010. **50**(1): p. 227-233.
74. J. Peddieson, G.R.B., *Mathematical modelling of an age-forming process.* Mathematical and Computer Modelling 1990. **14**: p. 1057–1060.
75. Sallah, M., J. Peddieson, and S. Foroudastan, *A mathematical model of autoclave age forming.* Journal of materials processing technology, 1991. **28**(1): p. 211-219.
76. Jackson, M., J. Peddieson, and S. Foroudastan, *Age-forming of beam structures' analysis of springback using a unified viscoplastic model.* Proceedings of the Institution of Mechanical Engineers, Part L: Journal of Materials Design and Applications, 2005. **219**(1): p. 17-24.
77. Narimetla, S., et al., *A simulation procedure for panel age forming.* Journal of engineering materials and technology, 1998. **120**(2): p. 183-190.
78. Narimetla, S., et al., *A simple unified age forming model.* Mechanics Research Communications, 2000. **27**(6): p. 631-636.
79. Guines, D., A. Gavrus, and E. Ragneau, *Numerical modeling of integrally stiffened structures forming from creep age forming technique.* International Journal of Material Forming, 2008. **1**(1): p. 1071-1074.

80. Kowalewski, Z., D. Hayhurst, and B. Dyson, *Mechanisms-based creep constitutive equations for an aluminium alloy.* The Journal of Strain Analysis for Engineering Design, 1994. **29**(4): p. 309-316.
81. Shercliff, H. and M. Ashby, *A process model for age hardening of aluminium alloys—I. The model.* Acta Metallurgica et Materialia, 1990. **38**(10): p. 1789-1802.
82. Poole, W., et al., *A model for predicting the effect of deformation after solution treatment on the subsequent artificial aging behavior of AA7030 and AA7108 alloys.* Metallurgical and Materials Transactions A, 2000. **31**(9): p. 2327-2338.
83. Kashyap, K., et al., *A model for two-step ageing.* Bulletin of Materials Science, 2000. **23**(5): p. 405-411.
84. Grèze, R., et al., *Influence of the temperature on residual stresses and springback effect in an aluminium alloy.* International Journal of Mechanical Sciences, 2010. **52**(9): p. 1094-1100.
85. Zhan, L., J. Lin, and M. Huang, *Study on Springback Behavior in Creep Age Forming of Aluminium Sheets.* Advanced Science Letters, 2013. **19**(1): p. 75-79.
86. LEVERS, A., *AIRCRAFT COMPONENT MANUFACTURING TOOL AND METHOD*, 2004, WO Patent 2,004,054,735.
87. Huang, S., et al., *Aluminum Alloy Creep Test and Its Constitutive Modeling.* Journal of Aeronautical Materials, 2008. **28**(1): p. 93.
88. Miller, J., S. Kyriakides, and E. Corona, *On bend-stretch forming of aluminum extruded tubes—II: analysis.* International Journal of Mechanical Sciences, 2001. **43**(5): p. 1319-1338.
89. Miller, J. and S. Kyriakides, *Three-dimensional effects of the bend–stretch forming of aluminum tubes.* International journal of mechanical sciences, 2003. **45**(1): p. 115-140.
90. ZHANG, Z.-g., et al., *Age forming of aluminum alloy.* Age Forming of Aluminum Alloy, 2008. **2**: p. 57-59.
91. Starink, M., et al., *Relations between microstructure, precipitation, age-formability and damage tolerance of Al–Cu–Mg–Li (Mn, Zr, Sc) alloys for age forming.* Materials Science and Engineering: A, 2006. **418**(1): p. 241-249.
92. May, A., et al., *Influence of heat treatment on the fatigue behaviour of two aluminium alloys 2024 and 2024 plated.* Procedia Engineering, 2010. **2**(1): p. 1795-1804.
93. Marlaud, T., et al., *Electrochemical aspects of exfoliation corrosion of aluminium alloys: The effects of heat treatment.* Corrosion Science, 2011. **53**(4): p. 1394-1400.
94. Reis, D.A., et al. *Effect of Artificial Aging on the Mechanical Properties of an Aerospace Aluminum Alloy 2024*. in *Defect and Diffusion Forum*. 2012. Trans Tech Publ.
95. Rioja, R.J., et al., *METHODS OF AGING ALUMINUM ALLOYS TO ACHIEVE IMPROVED BALLISTICS PERFORMANCE*, 2010, Google Patents.
96. Chakrabarti, D.J., et al., *ALUMINUM ALLOY PRODUCTS AND ARTIFICIAL AGING METHOD*, 2012, EP Patent 1,346,073.
97. Alexis, J., et al., *Study of the Influence of the Artificial Ageing Temperature on the AA2024 Alloy Microstructure.* Key Engineering Materials, 2013. **550**: p. 115-125.
98. ASM-Handbook, *Heat Treating: Heat Treating of Aluminum Alloys, Precipitation from Solid Solution.* 2002. **Volume 4**.
99. Sieniawski, J. and G. MrÄłwka-Nowotnik, *Analysis of Intermetallic Phases in 2024 Aluminium Alloy.* Solid State Phenomena, 2013. **197**: p. 238-243.
100. D.A. Porter and K.E. Easterling, *Phase Transformations in Metals and Alloys.* 1996(2nd ed., CHapman and Hall): p. 514.

101. Liu, G., et al., *Modeling the strengthening response to aging process of heat-treatable aluminum alloys containing plate/disc-or rod/needle-shaped precipitates.* Materials Science and Engineering: A, 2003. **344**(1): p. 113-124.
102. Cassell, A., et al., *Microstructure and corrosion behaviour of low copper 7xxx aluminium alloy.* Surface and Interface Analysis, 2013.
103. Liu, H. and X. Feng, *Effect of post-processing heat treatment on microstructure and microhardness of water-submerged friction stir processed 2219-T6 aluminum alloy.* Materials & Design, 2012.
104. Yuan, S., et al., *Effects of precipitate morphology on the notch sensitivity of ductile fracture in heat-treatable aluminum alloys.* Materials Science and Engineering: A, 2010. **527**(27): p. 7369-7381.
105. Liu, G., et al., *Experiment and multiscale modeling of the coupled influence of constituents and precipitates on the ductile fracture of heat-treatable aluminum alloys.* Acta materialia, 2005. **53**(12): p. 3459-3468.
106. Yan, J., *Strength Modelling of Al-Cu-Mg Type Alloys*, 2006, University of Southamtpon.
107. Liu, G., et al., *Heat treatment-modulated coupling effect of multi-scale second-phase particles on the ductile fracture of aged aluminum alloys.* Acta materialia, 2007. **55**(1): p. 273-284.
108. Song, M., *Modeling the hardness and yield strength evolutions of aluminum alloy with rod/needle-shaped precipitates.* Materials Science and Engineering: A, 2007. **443**(1): p. 172-177.
109. Banerjee, S., P. Robi, and A. Srinivasan, *Prediction of hot deformation behavior of Al–5.9% Cu–0.5% Mg alloys with trace additions of Sn.* Journal of Materials Science, 2012. **47**(2): p. 929-948.
110. Zhang, J., Y. Deng, and X. Zhang, *Constitutive modeling for creep age forming of heat-treatable strengthening aluminum alloys containing plate or rod shaped precipitates.* Materials Science and Engineering: A, 2012.
111. Kalikmanov, V., *Classical Nucleation Theory*, in *Nucleation Theory*. 2013, Springer. p. 17-41.
112. Hou, Y.-H., et al., *Modeling of whole process of ageing precipitation and strengthening in Al-Cu-Mg-Ag alloys with high Cu-to-Mg mass ratio.* Transactions of Nonferrous Metals Society of China, 2010. **20**(5): p. 863-869.
113. ASM-Handbook, *Heat Treating: Heat Treating of Aluminum Alloys, Strengthening by Heat Treatment.* 2002. **Volume 4**.
114. ASM-Handbook, *Heat Treating: Heat Treating of Aluminum Alloys, Fabrication and Finishing of Aluminum Alloys, Heat Treating.* 2002. **Volume 4**.
115. Lin*, J., et al., *Development of dislocation-based unified material model for simulating microstructure evolution in multipass hot rolling.* Philosophical magazine, 2005. **85**(18): p. 1967-1987.
116. Lin, J., J. Cao, and D. Balint, *Development and determination of unified viscoplastic constitutive equations for predicting microstructure evolution in hot forming processes.* International Journal of Mechatronics and Manufacturing Systems, 2011. **4**(5): p. 387-401.
117. Cao, J., J. Lin, and T. Dean, *An implicit unitless error and step‐size control method in integrating unified viscoplastic/creep ODE‐type constitutive equations.* International journal for numerical methods in engineering, 2008. **73**(8): p. 1094-1112.

118. De Jong, K.A., *Evolutionary computation: a unified approach*. Vol. 262041944. 2006: MIT press Cambridge.
119. Li, B., J. Lin, and X. Yao, *A novel evolutionary algorithm for determining unified creep damage constitutive equations.* International Journal of Mechanical Sciences, 2002. **44**(5): p. 987-1002.
120. Lin J, H.D., Dyson BF, *A new design of uniaxial testpiece with slit extensometer ridges for improved accuracy of strain measurement.* International Journal of Mechanical Sciences, 1993. **35**(1): p. 63-78.
121. Liu, D.Z., et al., *The review of computational FE software for creep damage mechanics.* Advanced Materials Research, 2012. **510**: p. 495-499.
122. D.Simulia, *Abaqus analysis user's manual, contact pressure-overclosure relationships.* Abaqus 6.11 Documentation, 2011. **33**(1.2).
123. Bahloul, R., S. Ben-Elechi, and A. Potiron, *Optimisation of springback predicted by experimental and numerical approach by using response surface methodology.* Journal of materials processing technology, 2006. **173**(1): p. 101-110.
124. Papadia, G., A. Del Prete, and A. Anglani, *Experimental springback evaluation in hydromechanical deep drawing (HDD) of large products.* Production Engineering, 2012. **6**(2): p. 117-127.
125. Parsa, M., H. Pishbin, and M. Kazemi, *Investigating spring back phenomena in double curved sheet metals forming.* Materials & Design, 2012.
126. Hopp, T.H., *The sensitivity of three-point circle fitting.* NIST report NISTIR, 1994. **5501**.
127. Meinders, T., et al., *Numerical product design: springback prediction, compensation and optimization.* International Journal of Machine Tools and Manufacture, 2008. **48**(5): p. 499-514.
128. Li, L., et al., *Numerical simulations on reducing the unloading springback with multi-step multi-point forming technology.* The International Journal of Advanced Manufacturing Technology, 2010. **48**(1-4): p. 45-61.
129. Liao, J., et al., *A new springback compensation method for sheet metal bending based on curvature correction.* Advanced Materials Research, 2010. **97**: p. 130-134.
130. Cafuta, G., N. Mole, and B. Štok, *An enhanced displacement adjustment method: Springback and thinning compensation.* Materials & Design, 2012.
131. Chung, K., et al., *The 8th international conference and workshop on numerical simulation of 3d sheet metal forming processes (numisheet 2011).* 2012.
132. Gan, Z., H.B. Tan, and J.Z. Zhu, *Simulation and Springback Prediction of Integral Panel with High Ribs in Age Forming.* Applied Mechanics and Materials, 2012. **152**: p. 135-139.
133. Abdelal, G.F., N. Abuelfoutouh, and A.H. Gad, *Finite Element Analysis for Satellite Structures: Applications to Their Design, Manufacture and Testing*. 2013: Springer.
134. Mu, L., et al., *Comparative study of tribological properties of different fibers reinforced PTFE/PEEK composites at elevated temperatures.* Tribology Transactions, 2010. **53**(2): p. 189-194.
135. Zienkiewicz, O., R. Taylor, and J. Too, *Reduced integration technique in general analysis of plates and shells.* International Journal for Numerical Methods in Engineering, 1971. **3**(2): p. 275-290.
136. Schwarze, M. and S. Reese, *A reduced integration solid‐shell finite element based on the EAS and the ANS concept—Large deformation problems.* International journal for numerical methods in engineering, 2011. **85**(3): p. 289-329.

137. Mc-Donnel-Douglas-Astronautics-Company, *ISOGRID DESIGN HANDBOOK*. 1973.
138. Wang, X., *Overview on Biocompatibilities of Implantable Biomaterials*. 2013.

# Appendix A

Detailed drawings of the four point bending rig are shown here:

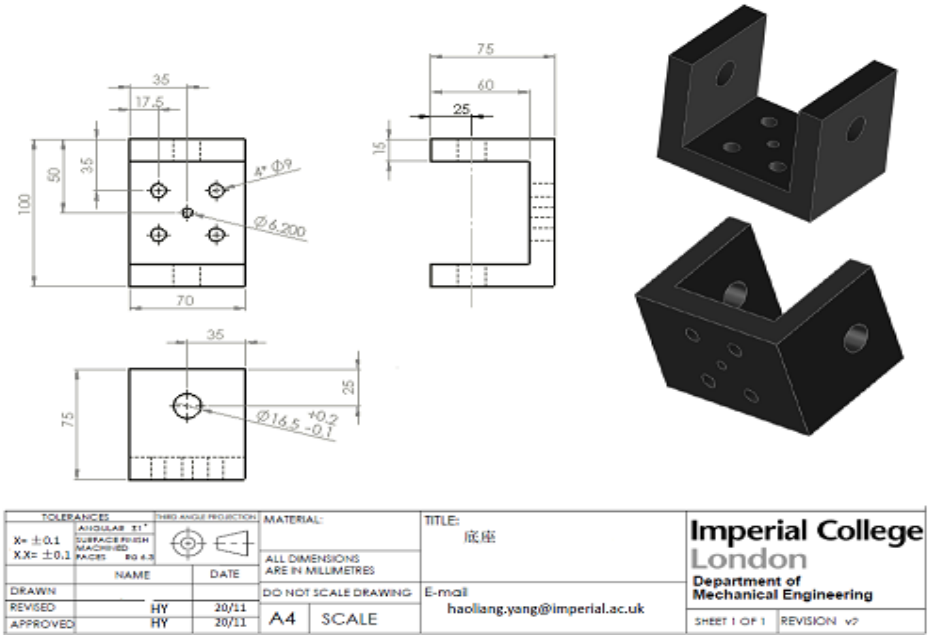


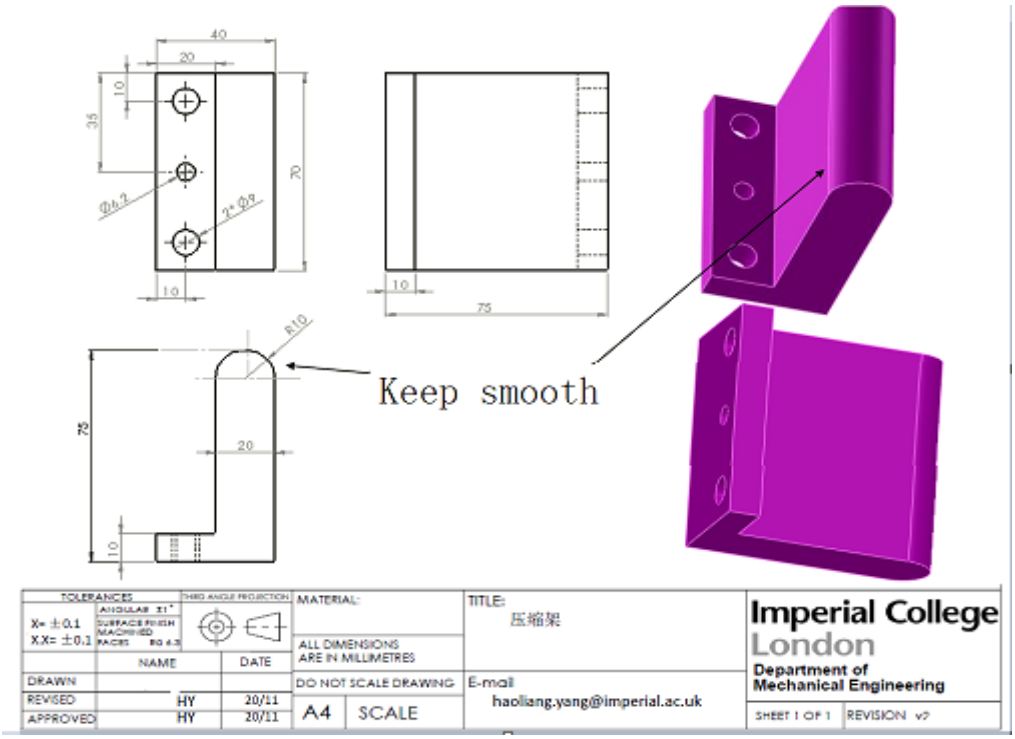

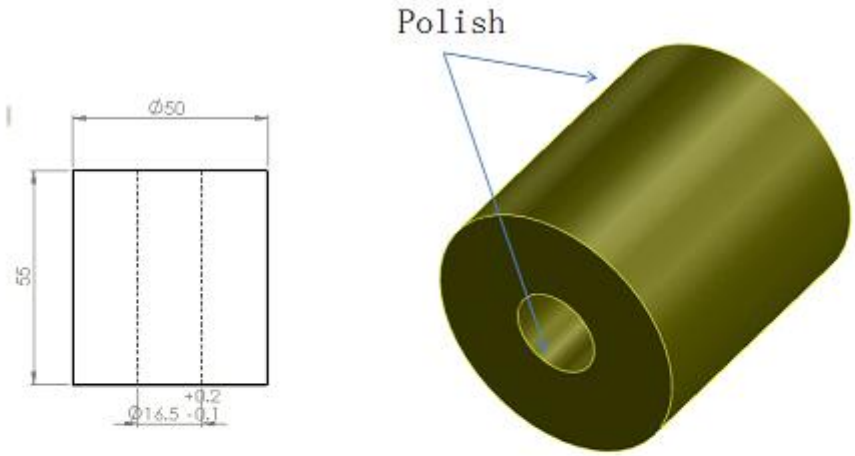


| TOLERANCES | | THIRD ANGLE PROJECTION | MATERIAL: | TITLE: 滚轮 | Imperial College London<br>Department of Mechanical Engineering |
|---|---|---|---|---|---|
| X= ±0.1<br>X.X= ±0.1 | ANGULAR ±1°<br>SURFACE FINISH MACHINED FACES Ra 6.3 | | ALL DIMENSIONS ARE IN MILLIMETRES | | |
| | NAME | DATE | DO NOT SCALE DRAWING | E-mail haoliang.yang@imperial.ac.uk | |
| DRAWN | | | A4 SCALE | | SHEET 1 OF 1 REVISION v2 |
| REVISED | HY | 20/11 | | | |
| APPROVED | HY | 20/11 | | | |

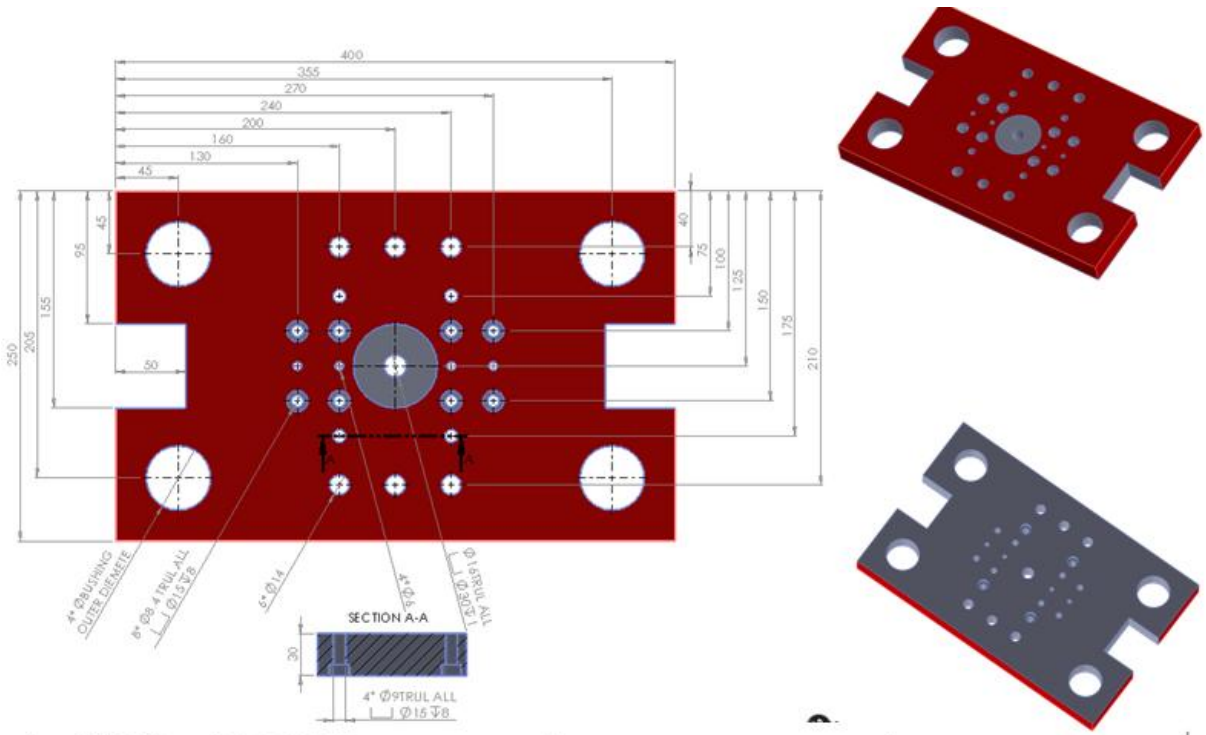


| TOLERANCES | | THIRD ANGLE PROJECTION | MATERIAL: Mild steel | TITLE: TOP Plate<br>Amount : 1 | Imperial College London<br>Department of Mechanical Engineering |
|---|---|---|---|---|---|
| X= ±0.1<br>X.X= ±0.1 | ANGULAR ±1°<br>SURFACE FINISH MACHINED FACES Ra 6.3 | | ALL DIMENSIONS ARE IN MILLIMETRES | | |
| | NAME | DATE | DO NOT SCALE DRAWING | E-mail haoliang.yang@imperial.ac.uk | |
| DRAWN | | | A4 SCALE | | SHEET 1 OF 1 REVISION v2 |
| REVISED | HY | 09/12 | | | |
| APPROVED | HY | 09/12 | | | |

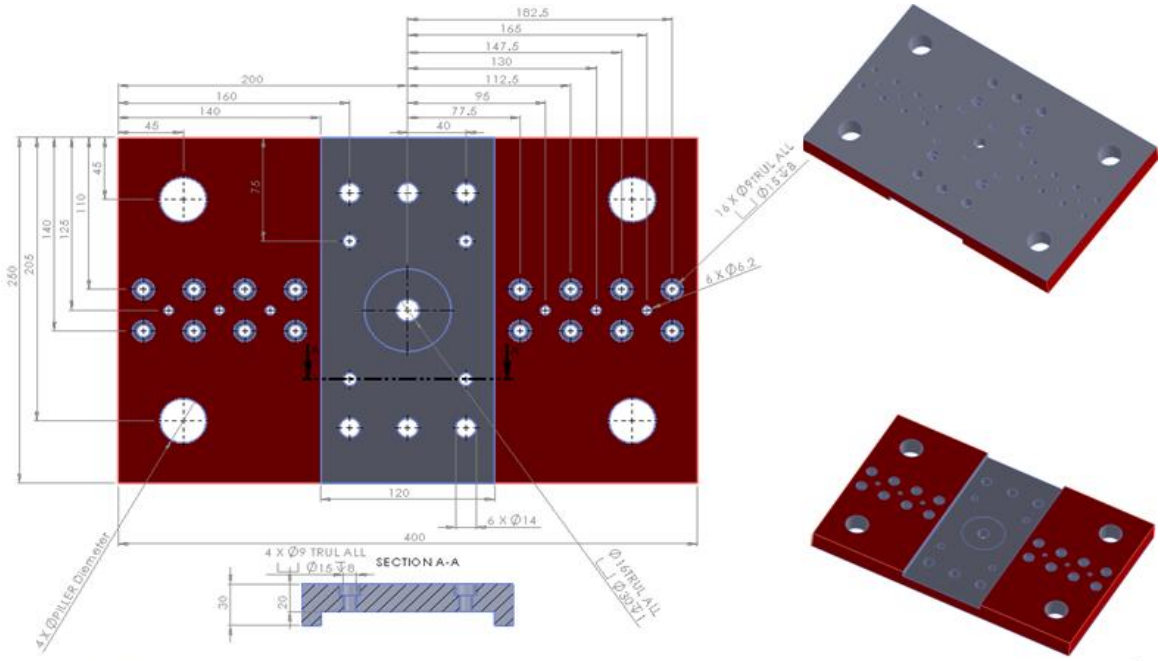


| TOLERANCES | | THIRD ANGLE PROJECTION | MATERIAL: | TITLE: | Imperial College London |
|---|---|---|---|---|---|
| X= ±0.1<br>X.X= ±0.1 | ANGULAR ±1°<br>SURFACE FINISH MACHINED FACES Ra 6.3 | | Mild steel<br>ALL DIMENSIONS ARE IN MILLIMETRES | Bottom plate ( page 1/2)<br>Amount : 1 | Department of Mechanical Engineering |
| | NAME | DATE | DO NOT SCALE DRAWING | E-mail haoliang.yang@imperial.ac.uk | |
| DRAWN | | | A4 SCALE | | SHEET 1 OF 1 REVISION v2 |
| REVISED | HY | 09/12 | | | |
| APPROVED | HY | 09/12 | | | |

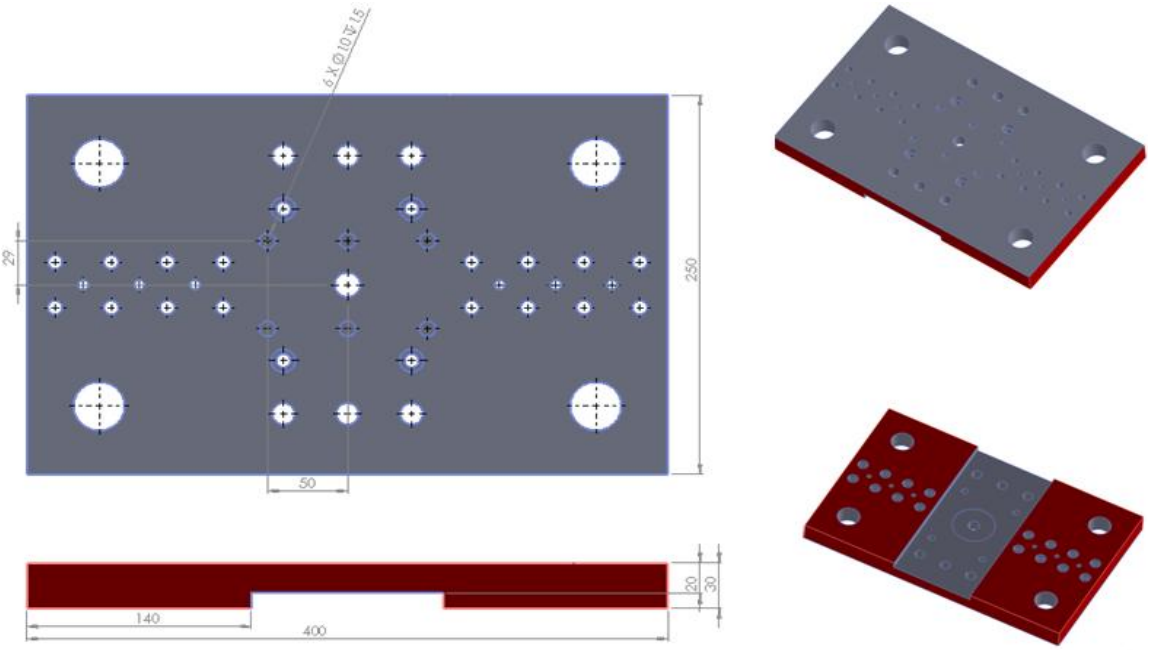


| TOLERANCES | | THIRD ANGLE PROJECTION | MATERIAL: | TITLE: | Imperial College London |
|---|---|---|---|---|---|
| X= ±0.1<br>X.X= ±0.1 | ANGULAR ±1°<br>SURFACE FINISH MACHINED FACES Ra 6.3 | | Mild steel<br>ALL DIMENSIONS ARE IN MILLIMETRES | Bottom plate ( page 2/2)<br>Amount : 1 | Department of Mechanical Engineering |
| | NAME | DATE | DO NOT SCALE DRAWING | E-mail haoliang.yang@imperial.ac.uk | |
| DRAWN | | | A4 SCALE | | SHEET 1 OF 1 REVISION v2 |
| REVISED | HY | 09/12 | | | |
| APPROVED | HY | 09/12 | | | |

# Appendix B

Mesh convergence studies have been performed for all the simulations in this thesis in order to guarantee that enough elements are used to get a convergent solution. Mesh convergence studies have been performed with different size of mesh e.g. 15 mm, 10 mm, 5 mm and 4 mm for the simulations in this thesis. Good agreements have been obtained by using the mesh size of 5 mm and 4 mm. A detailed convergence study is performed here to investigate the effect of implementation different size mesh. The mesh size induced equivalent stresses in the simulation will be more sensitive, if the maximum induced stress of the material is below yield stress in pure elastic region. The simulation results shown here are carried out based on the uniform pressure loading on CAF of an AA7055 sheet in Chapter 6. Figure B-1 shows the surface equivalent stress of the workpiece for uniform pressure loading conditions at the initial loading. The mesh sizes are 15 mm, 10 mm, 5 mm and 4 mm respectively.

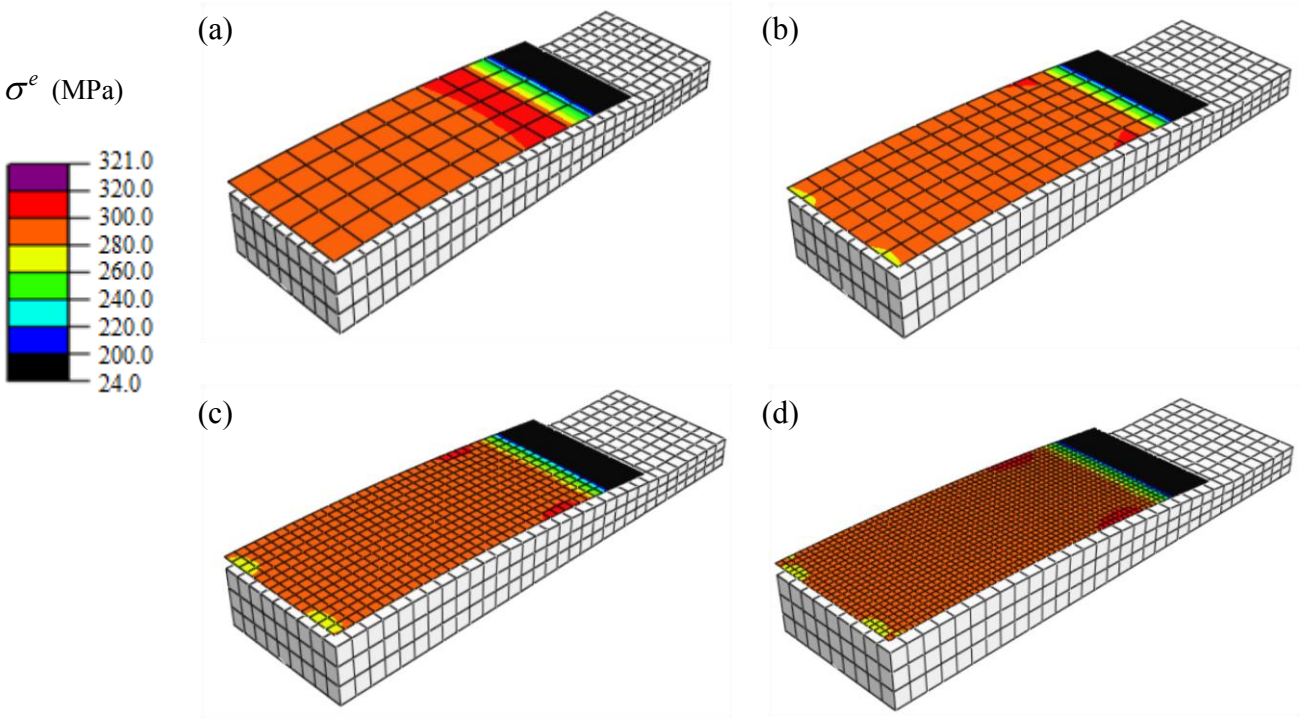


Figure B-1: The surface equivalent stress of the workpiece for uniform pressure loading conditions at the initial loading. The mesh sizes are (a) 15 mm, (b) 10 mm, (c) 5 mm and (d) 4 mm respectively.

From the simulation results, we can see that good agreements have been obtained by using the mesh size of 5 mm and 4 mm. The subsequent simulations on the fully age stages and after springback stages is related to the initial loading's stress distribution. Thus it is necessary to perform the mesh convergence studies in order to get the accurate solutions.